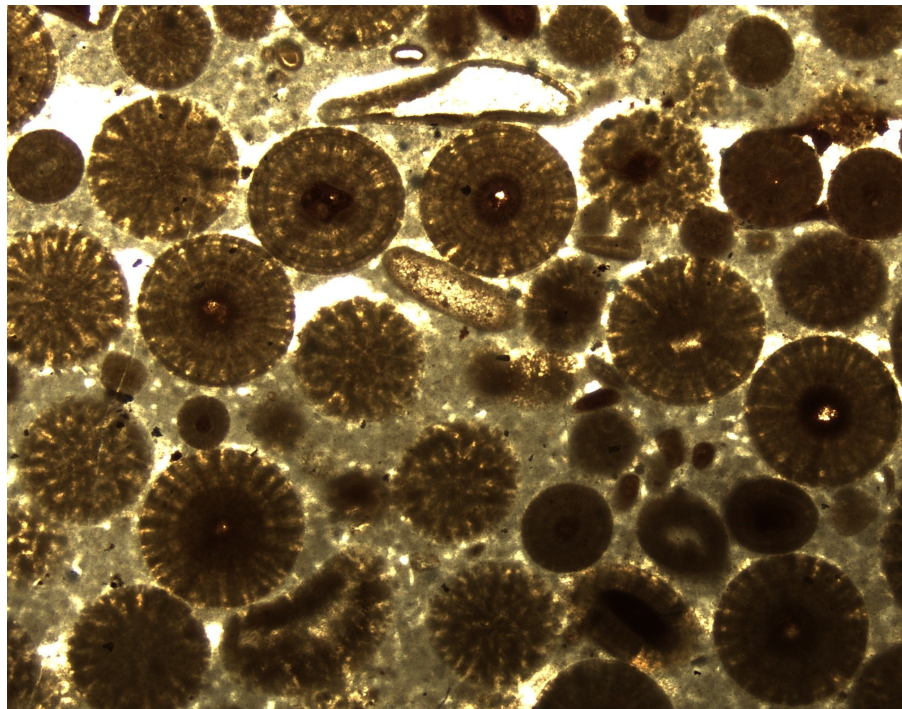


# Oolites from the Arabian platform: Archives for the aftermath of the end- Triassic mass extinction

***Johannes Greiff***

Dissertations in Geology at Lund University,  
Master's thesis, no 616  
(45 hp/ECTS credits)

---



Department of Geology  
Lund University  
2021



# **Oolites from the Arabian platform: Archives for the aftermath of the end- Triassic mass extinction**

Master's thesis  
Johannes Greiff

Department of Geology  
Lund University  
2021

# Contents

<b>1 Introduction .....</b>	<b>9</b>
<b>2 Background .....</b>	<b>9</b>
2.1 The end-Triassic mass extinction	9
2.1.1 The Triassic—Jurassic GSSP & Terrestrial effects of the ETME	9
2.1.2 Causes and environmental implications	10
2.1.3 Carbon cycle and ocean acidification	11
2.2 Ooids	11
2.3 Microbialites	13
2.4 Anachronistic facies	13
<b>3 Geological setting and stratigraphy .....</b>	<b>14</b>
3.1 The Ghalilah Formation	17
3.2 The Triassic—Jurassic boundary in the United Arab Emirates	17
<b>4 Methods .....</b>	<b>18</b>
4.1 Field work in the United Arab Emirates	18
4.2 Thin sections for optical microscope and LA-ICP-MS analyses	18
4.3 Optical petrographic microscope	18
4.4 Samples for SEM analyses	19
4.5 SEM (Scanning Electron Microscope)	19
4.6 LA-ICP-MS (Laser Ablation—Inductively Coupled Plasma—Mass Spectrometry)	19
4.7 Processing of LA-ICP-MS data	20
<b>5 Results .....</b>	<b>21</b>
5.1 Logs of the outcrop	21
5.1.1 Log of the uppermost Triassic Sumra Member (Rhaetian)	21
5.1.2 Log of the Jurassic Sakhra Member (Hettangian)	22
5.1.3 Legend for the logs	23
5.2 Petrographic descriptions and interpretations of the Wadi Ghalilah samples	24
5.3 Summary of thin section observations	26
5.4 Micritization intervals	26
5.5 Sequence stratigraphy	27
5.6 SEM	27
5.7 LA-ICP-MS	29
5.7.1 Average elemental concentrations	29
5.7.2 REE + Y concentrations	30
5.7.3 Ooid laminae major and minor elemental concentrations	31
5.8 Transects	37
5.9 Ce anomaly and redox conditions	40
<b>6 Discussion .....</b>	<b>40</b>
6.1 Petrographic analyses	40
6.2 SEM interpretations	40
6.3 Sequence stratigraphy	40
6.4 Milankovitch cyclicity	41
6.5 Previous analyses of the Ghalilah Formation	41
6.6 LA-ICP-MS interpretations	42
6.6.1 Average ooid elemental concentrations	42
6.6.2 Transects	42
6.7 Redox conditions	42
6.7.1 Ce ratios and calculations	42
6.7.2 Hypotheses of varying P concentrations in ooids	43

**Cover Picture:** Radial ooids from sample WG19 in this study, as seen in the optical microscope through plane polarized light. Photo: Johannes Greiff



## Contents, continued

6.7.3 Shift in Ce ratios and its implications	43
6.7.4 Th/U ratios as redox proxies	43
6.8 Ocean acidification	44
6.8.1 The "Unreefing" model and global perspectives	44
6.8.2 Ocean acidification in Wadi Ghalilah	45
6.9 Comparison to modern day events	45
<b>7 Conclusions</b> .....	<b>45</b>
<b>8 Acknowledgements</b> .....	<b>46</b>
<b>References</b> .....	<b>46</b>
<b>Appendix 1</b> .....	<b>51</b>
<b>Appendix 2</b> .....	<b>61</b>
<b>Appendix 3</b> .....	<b>67</b>

# Oolites from the Arabian platform: Archives for the aftermath of the end-Triassic mass extinction

JOHANNES GREIFF

Greiff, J., 2021: Oolites from the Arabian platform: Archives for the aftermath of the end-Triassic mass extinction. *Dissertations in Geology at Lund University*, No. 616, 72 pp. 45 hp (45 ECTS credits).

**Abstract:** The end-Triassic mass extinction (ETME) which occurred around 201 Ma is known as one of “the big five” mass extinction events of the Phanerozoic eon. Its effects were most severe on marine ecosystems, resulting in a global decline of invertebrate taxa and the complete extinction of the conodonts. The cause of the ETME can be attributed to the volcanic activity of the Central Atlantic magmatic province (CAMP), which resulted in drastic emissions of volcanogenic gasses such as CO<sub>2</sub> and SO<sub>2</sub>. These eruptions caused severe environmental changes such as global warming and ocean acidification, which made the ETME particularly selective for acid sensitive taxa. These conditions also resulted in an almost global depositional hiatus at the time of the Triassic – Jurassic boundary.

In this study, marine strata from the Triassic – Jurassic boundary interval at Wadi Ghalilah in the United Arab Emirates have been petrographically and geochemically analysed. The examined strata are part of the Ghalilah Formation, namely the uppermost Sumra (Rhaetian) and the Sakhra (Hettangian) Members. The study had the goal to describe the geological, geochemical, and environmental conditions present after the ETME. Results were also compared with other Triassic—Jurassic boundary sections in order to understand the effects of the ETME on global and regional scales.

Through the analyses conducted in this study, it seems evident that the ocean acidification caused by CAMP was indeed widespread enough to affect the southern latitudes of the UAE at the time. This can be seen in the form of a submarine dissolution surface and subsequent deposition of oolites and microbialites as anachronistic facies. The globally recognized Hettangian transgressions are also supported from Wadi Ghalilah, and was likely strongly influenced by the disappearance of carbonate producing organisms. Analyses of major, trace, and rare earth elements in ooids indicate a slight increase in anoxia after the onset of the Hettangian, as well as increased continental weathering which could be coupled with the start of increased biological productivity after the extinction.

**Keywords:** sedimentology, carbonates, geochemistry, oolites, ooids, thrombolites, microbialites, Triassic, Jurassic, Hettangian, extinction, United Arab Emirates, Wadi Ghalilah, Wadi Milaha.

**Supervisors:** Sylvain Richoz (LU), Ingrid Urban (LU)

**Subject:** Bedrock Geology

*Johannes Greiff, Department of Geology, Lund University, Sölvegatan 12, SE-223 62 Lund, Sweden. E-mail: greiff.johannes@gmail.com*

# Ooliter från Arabiska plattformen: Arkiv för efterföljerna av det sen-Triassiska massutdöendet

JOHANNES GREIFF

Greiff, J., 2021: Ooliter från Arabiska plattformen: Arkiv för följderna av det sen-Triassiska massutdöendet. *Examensarbeten i geologi vid Lunds universitet*, Nr. 616. 72 sid. 45hp.

**Sammanfattning:** Det sen-Triassiska massutdöendet (STM) som inträffade för omkring 201 miljoner år sedan är känt som ett av ”de fem stora” massutdöendena under Fanerozoisk tid. Massutdöendet påverkade främst marina ekosystem, vilket resulterade i en global minskning av ryggradslösa djur och utdöendet av konodonterna. Orsaken till STM kan anknytas till utbrotten av den Central-Atlantiska magmatiska provinsen (CAMP), vars utsläpp av vulkanogena gaser såsom koldioxid och svaveldioxid resulterade i drastiska miljöförändringar såsom global uppvärmning och försurning av haven. Detta medförde att organismer som var speciellt känsliga för låga pH-nivåer drabbades hårdast. Dessutom orsakade denna försurning avbrott i depositionen av karbonater under den Triassiska – Jurassiska övergången på ett flertal platser globalt.

I denna studie har marina avlagringar från slutet av trias och början av jura från Wadi Ghalilah i Förenade Arabemiraten petrografiskt och geokemiskt analyserats. Det undersökta intervallet ingår i Ghalilahformationen och består av översta delen av Sumraledet (rät) och Sakhraledet (hettang). Målet med undersökningarna har varit att beskriva de geologiska och geokemiska förhållandena som rådde efter STM. Resultaten har även jämförts med andra likåldriga avlagringar för att få en uppfattning om hur omfattande påverkningarna av STM har varit på global och regional skala.

Analyserna som utförts i denna studie tyder på att försurningen av havet måste varit omfattande nog för att också påverka de tropiska breddgraderna där Wadi Ghalilah en gång låg. Detta kan ses i form av marina upplösningsytor och efterföljande deposition av ooliter of mikrober i form av anakronistiska facies. De globalt igenkänningsbara transgressioner som förekom under hettang kan även observeras vid Wadi Ghalilah, och var sannolikt påverkade i hög grad av försvinnandet av karbonatproducerande organismer. Analyser av grund- och spårämnen samt sällsynta jordartsmetaller i ooider indikerar en lätt ökning av syrefattiga förhållanden efter början av hettang, samt ökad kontinental vittring vilket skulle kunna kopplas till början av en långsam ökning av biologisk produktivitet efter massutdöendet.

**Nyckelord:** sedimentologi, karbonatbergarter, geokemi, ooliter, ooider, thromboliter, mikrober, trias, jura, hettang, massutdöende, Förenade Arabemiraten, Wadi Ghalilah, Wadi Milaha.

**Handledare:** Sylvain Richoz (LU), Ingrid Urban (LU)

**Ämnesinriktning:** Berggrundsgeologi

*Johannes Greiff, Geologiska institutionen, Lunds universitet, Sölvegatan 12, SE-223 62 Lund, Sweden. E-mail: greiff.johannes@gmail.com*



# 1 Introduction

It should undoubtedly have escaped no one, that present day greenhouse gas emissions and associated global warming poses a significant threat to the continued survival of many species on Earth. The IPCC states that “Any increase in global warming is projected to affect human health, with primarily negative consequences” and that “The risk of irreversible loss of many marine and coastal ecosystems increases with global warming, especially at 2°C or more” (IPCC 2018). Although global warming in the Anthropocene is one of the largest crises humanity has faced thus far, it is far from the first time that earth has undergone drastic environmental changes. In the geologic record, the sudden demise of broad ranges of taxa can sometimes be linked with such perturbations, resulting in what are known as mass extinction events. After such events, both environment and fauna undergo dramatic changes.

My master’s thesis will focus on the aftermath of one of these events, the end-Triassic mass extinction (ETME). By petrographically and geochemically analyzing sediments from a marine carbonate succession of Rhaetian and Hettangian age in the United Arab Emirates (UAE), it will be possible to gain a unique insight into the direct consequences of the extinction. The formation which will be analyzed is named the Ghalilah Formation, and outcrops in Wadi Ghalilah, which is the main locality for this study. Within the Ghalilah Formation, it is particularly the Sakhra Member which will be in focus, as it contains marine sediments from the Triassic – Jurassic (T-J) boundary interval and the earliest Jurassic Hettangian stage.

At the time of the T-J transition, large parts of the Arabian shelf were covered by the Tethys Ocean. Productivity in the Tethys Ocean was high, which during the Permian and most of the Mesozoic promoted deposition of carbonates and organic rich shales, which in present day constitute much of the oil and natural gas used for our worldwide energy needs. By the transition into the Jurassic, there is a distinct observable change in the lithological and paleontological record. This change can be directly linked to the ETME and the events leading up to its occurrence.

The post extinction intervals displayed in the Ghalilah Formation at Wadi Ghalilah contain anachronistic facies such as microbialites and ooids, which are facies typical for pre-phanerozoic times (Sepkoski et al. 1991; Groves & Calner 2004; Baud et al. 2007). Interestingly, these types of facies can be found rather regularly in the direct aftermath of phanerozoic mass- and smaller scale extinction events such as the Permian mass extinction and the Silurian Lau event (Sepkoski et al. 1991; Groves & Calner 2004; Baud et al. 2007). Petrographic and sedimentological analysis on these deposits will allow for an improved understanding on how the sea level and the depositional environment varied through time, and how this can be correlated on regional and even global scales. Furthermore, applying LA-ICP-MS analysis on these sediments allows for an improved understanding of the environmental, chemical, biological, and geological settings of the area at the time of formation. This is achieved by directly measuring which types of major

and trace elements are present in the ooids, cement, and matrix, and to what extent. Individual ooids were studied in order to gain information about elemental changes on a yearly or decadal base, as well as to analyze larger scale changes and trends in carbonate deposition. Observations using Scanning Electron Microscope (SEM) were also conducted in order to analyze and characterize ooids in greater detail, and will complement the observations made from thin sections using optical microscopes.

Furthermore, results from the locality at Wadi Ghalilah are compared with a nearby locality named Wadi Milaha located 24 km SSE of the main locality where an outcrop of the Ghalilah Formation is also exposed. This will provide a basis for paleoenvironmental reconstruction on a regional scale. Moreover, it will simplify correlation between other globally recognized T-J boundary sections to those in the UAE, as both the placement of the T-J boundary and the effects of the ETME at these localities have long been debated. The results from Wadi Milaha have been obtained by supervisor Ingrid Urban as part of her PhD project dealing with geochemical characterization of ooids during the aftermath of mass extinctions.

## 2 Background

### 2.1 The end-Triassic mass extinction

#### 2.1.1 The Triassic—Jurassic GSSP & terrestrial effects of the ETME

The ETME which occurred around 201 Ma at the very end of the Triassic period is widely regarded as one of the “big five” mass extinction events of the Phanerozoic eon (Sepkoski, 1982). During this time-period marine biota in particular was severely affected. This led to the decline of several invertebrate taxa such as molluscs (Kiessling 2007), as well as cnidarians and other reef builders (Stanley 1988, 2003; Stanley & Beauvais 1994). In addition to causing major changes in plankton communities (Richoz et al. 2012), the most typical markers for the extinction event and the T-J boundary are the complete extinction of the conodonts and the first appearance of the Jurassic ammonite *Psiloceras spelae* in the Hettangian (Hillebrandt et al. 2007). A global stratotype section and point (GSSP) was not set for the base of the Jurassic until 2008, which has made correlation of early Jurassic strata notoriously difficult. The GSSP is presently placed in the Kuhjoch section of the Austrian Karwendel mountains (Hillebrandt et al. 2007, 2013). The section includes the first occurrence of *Psiloceras spelae* 6 m above the boundary between the Rhaetian Kössen Formation and the Kendelbach Formation, which represents the extinction level (Hillebrandt et al. 2007; Hautmann 2012, Hillebrandt et al. 2013). It should be noted that this GSSP has in recent years been debated, and arguments have been made regarding a change of

locality from the Kuhjoch section (Lucas et al. 2019).

In the terrestrial realm, there has been widespread debate over the last decade whether vegetation underwent a substantial decline during the T-J transition (Lucas & Tanner 2008; van de Schootbrugge et al. 2009; Hautmann 2012). While Lucas & Tanner (2008) argue that there is no evidence of a global mass extinction of terrestrial vegetation at the T-J boundary, van de Schootbrugge et al. (2009) suggest that sharp increases of atmospheric sulphate aerosols and other pollutants contributed to a severe and wide-ranging shift in terrestrial vegetation. This is in part based on the fact that gymnosperm forests were replaced by fern-like vegetation, which is a signature flora for disturbed ecosystems (van de Schootbrugge et al. 2009). In addition, more recent reviews by Lindström et al. (2016) concluded that ecosystems were indeed affected drastically enough on both hemispheres for significant decline in palynoflora to occur. Perhaps the most notable terrestrial implications for the ETME however, were the large niches left behind after the extinction of the Archosaurs and Raudisuchians, which led to the evolution of the dinosaurs in the late Jurassic (Serenio 1999).

### 2.1.2 Causes and environmental implications

Several potential causes for this mass extinction, both terrestrial and extra-terrestrial, have been suggested. Some of the more notable ones include the discovery of an iridium anomaly in the Newark Basin coincident with abundant fern spores, which Olsen et al. (2002) argued to mean that a bolide impact scenario was the primary cause for the ETME. In addition to this, several impact craters with apparent synchronous ages to the T-J boundary have also been discovered (van de Schootbrugge & Wignall 2016). The impact hypothesis has however since been disputed and deemed as improbable due to the non-contemporaneous occurrence of the potential impact sites, the sizes of the impact craters and further analysis of the iridium anomaly which argues for a volcanic origin of the anomaly (Tanner et al. 2016; Tegner et al. 2020). The most widely accepted model in present day and what I will use for this thesis states that episodes of Large Igneous Provinces (LIP) in the Central Atlantic Magmatic Province (CAMP) before the T-J transition resulted in severe climate change, which in turn led to the ETME (Schaltegger et al. 2008; Deenen et al. 2010; Davies et al. 2017). According to this model, extensive CAMP volcanism and flood basalt eruptions hundreds of thousands of years before the T-J boundary caused extreme influxes of sulphate aerosols and carbon dioxide into the ocean-atmosphere cycle (Schaltegger et al. 2008; Deenen et al. 2010; Davies et al. 2017; Percival et al. 2017; Tegner et al. 2020).

Through carbon isotope analyses of various T-J boundary sediments around the globe, the extinction can be correlated to a negative carbon isotope excursion (CIE) peak of roughly around -3 to -4‰ (Pálffy et al. 2021). Based on high-resolution U-Pb ages from CAMP mafic intrusions in various localities in Morocco and North America, the initial magmatic activity of CAMP can be correlated to just before the globally recognized negative CIE, indicating that the CAMP volcanism was indeed a driving mechanism for the ensuing climate changes and subsequent faunal decline (Davies et al. 2017; Percival et al. 2017; Heimdal et al. 2019, 2020). Moreover, it has been shown that clear increases in Hg and Hg/TOC (total organic carbon) ratios occur in T-J boundary sediments (Percival et al. 2017). This resulted in perturbations in the global Hg cycle at the time, which can be led back to the pulsatory volcanism of CAMP (Percival et al. 2017). These increased Hg concentrations would have strongly affected and delayed ecological recovery for many millions of years (Percival et al. 2017, Lindström et al. 2020).

It has been estimated that a volume of 3 million km<sup>3</sup> of magmas were released from CAMP, along with volcanogenic gases (Marzoli et al. 2018). These volumes make CAMP possibly the largest continental flood basalt to ever erupt (Wignall 2001; Nomade et al. 2007; Greene et al. 2012). In regards to this, it has recently been estimated that the total CO<sub>2</sub> emissions could have been as high as 24000 gigatons (Gt) over a time period of 800 thousand years (kyrs) of volcanic activity (Heimdal et al. 2020), suggesting that the amount of released magma is even larger than previously estimated by McHone (2003). This estimate has been achieved by analyzing proxies in the form of negative CIEs from terrestrial and marine sediments (Heimdal et al. 2020). The emissions caused during these 800 kyrs is interpreted to have taken place during five separate pulses and released carbon from three different sources; volcanic carbon, inorganic thermogenic carbon, and organic thermogenic carbon (Heimdal et al. 2020). The authors argue that the presence of thermogenic sources are highly plausible due to the vast amount of emissions predicted by the model (Heimdal et al. 2020). Indeed, these amounts are not enough to originate from volcanic carbon alone, as this is the highest estimate so far (McHone 2003, Heimdal et al. 2020).

Widespread black shales around the margins of the Tethys ocean were also being deposited in the early Jurassic, marking a distinct change in sedimentation style (Ricoz et al. 2012; van de Schootbrugge et al. 2013). Through uranium isotope analyses on shallow marine limestones deposited around the T-J boundary, research has suggested that a 40 - 100 times increase in the extent of anoxic deposition occurred worldwide (Jost et al. 2017). This is based on a negative excu-

sion of  $^{238}\text{U}$  of about 0.7 ‰, and it is suggested that this widespread anoxia likely delayed ecological recovery into the later stages of the Hettangian (Jost et al. 2017).

Previously one of the least studied and understood mass extinctions, research on the T-J mass extinction has had a major upswing in the last decade. The increasing interest is partly due to the progress in radiometric dating of the CAMP basalts (Hautmann et al. 2012). It must be noted, however, that there is some debate regarding the severity of the ETME. Some authors argue that the ETME is rather the result of minor events on a local scale (Lucas & Tanner 2018). For all intents and purposes, this thesis is written with the idea in mind that the end-Triassic mass extinction is in fact, a mass extinction event on a global scale.

### 2.1.3 Carbon cycle and ocean acidification

At other localities where marine T-J boundary strata have been studied, such as Europe, Asia and South America, the negative CIE from the initial stages of CAMP differs a few permille from the observed values at Wadi Ghalilah (Ruhl et al. 2020). Most global and Tethyan CIE from this interval are usually observed at around  $-4$  and  $-6.5$ ‰ (Ruhl et al. 2020), whereas in the Wadis of UAE it is around  $-1$  and  $-3$ ‰ (Ge et al 2018, Pálffy et al 2021).

Since the volcanic activity roughly tripled the amount of atmospheric ( $p$ )  $\text{CO}_2$  concentrations in the ocean-atmosphere cycle (McElwain et al., 1999; Schaller et al., 2011, 2012; Steinthorsdottir et al., 2011; Ruhl et al. 2020), climate, temperature and precipitation would have been severely affected (Ruhl et al 2020). This would have led to increased warming and humidity in both marine environments and continental settings (Korte et al., 2009; Bonis et al., 2009; Bonis et al., 2010; Ruhl et al., 2010; Bonis and Kürschner, 2012; Steinthorsdottir et al., 2012; Ruhl et al. 2020).

Various proxies of  $p\text{CO}_2$  also show a 1700-2500 ppm  $\text{CO}_2$  increase in the beginning of the Hettangian (Steinthorsdottir et al. 2011). More drastic increases have also been suggested, with numbers as high as 4400 to 5100 ppm increase directly following the CAMP eruptions (Schaller et al. 2011; Greene et al 2012).

With the drastic release of greenhouse gases, it is plausible that there would have been an initial climate cooling from the release of  $\text{SO}_2$  (Guex et al. 2016) and subsequent global warming and ocean acidification event where the excess  $p\text{CO}_2$  reacts with seawater to form carbonic acid (Greene et al. 2012). This subsequent warming around the T-J boundary has also been shown from palynological studies, indicating a 3-4 degree Celsius increase with climates transitioning

from arid to more humid at the start of the Jurassic (McElwain et al 1999; Greene et al 2012).

Considering the increase in atmospheric  $\text{CO}_2$  and other volcanogenic gases caused by CAMP volcanism, there have been several arguments made for and against the development of ocean acidification synchronous with the ETME. An ocean acidification event requires the influx of  $p\text{CO}_2$  to be greater than the influx (or buffering) of alkaline elements from weathering (Greene et al. 2012). This level of buffering of ancient oceans is simply not known for such deep time studies. Factors such as the dissolved inorganic carbon levels in the ocean also affected how sensitive the Tethys Ocean would have been to ocean acidification, and thus even an increase of 7000 ppm of  $p\text{CO}_2$  does not guarantee prolonged and significant lowering of seawater pH (Greene et al. 2012).

The ETME was however selective in nature, meaning that acid-sensitive and reef inhabiting taxa were especially affected by the oceanic perturbations at the time (KieSSLing 2007, 2011; Greene 2012). This, along with widely observed coincident carbonate depositional hiatus in the European Alps as well as North and South America (Hautmann et al. 2008; Greene et al. 2012), argues for the fact that CAMP was indeed significant enough in terms of  $\text{CO}_2$  output to have caused ocean acidification. As a result, numerous other T-J marine sections experienced a lack, or at least decrease, of carbonate deposition at this time (Greene et al. 2012).

## 2.2 Ooids

A major part of the herein described lithology at Wadi Ghalilah includes the occurrence of ooids. Ooids, and their lithified equivalents oolites, are millimeter-sized spherical grains which consist of a nucleus and an outer laminated layer called a cortex or laminae (Carozzi 1960). Due to hydrological conditions during their formation, ooids are usually not larger than 2 mm in diameter. Larger sizes would inhibit their growth rate significantly, however there is the exception of some giant ooids (i.e larger than 2 mm in diameter) (Li et al. 2013). The cortex can be made up out of a variety of minerals and elemental compositions including iron, silica, and phosphates. The most common types of ooids however, are carbonate ooids, which are also in the focus of this study. Moreover, ooids constitute as valuable proxies for paleoceanographical reconstruction where they can aid in the determination of seawater chemistry, depth, energy levels, and salinity (Sandberg 1983; Tucker 1990; Flügel 2010).

Ooids can be classified differently depending on the crystal structure of the cortex (Fig. 1), with the most common classification of ooids being concentric (Fig. 2), radial (Fig. 3) and micritic. Normally, radial

ooids tend to form in restricted low energy environments around platform interiors, whereas concentric ones form during higher energy conditions (Flügel 2010). Micritic ooids have a random or even absent laminae due to higher degrees of micritization (Flügel 2010). Additionally, in cases where the diameter of the nucleus is larger than the radial of the whole ooid, they are designated as superficial (Flügel 2010).

Although ooids occur in deposits as old as the Mesoarchean, formation remain debated. The formation of smaller sized ooids include formation in suspension in either high or low water energy conditions (Flügel 2010), as well as accretion in both marine and non-marine environments. The most leading model for many decades states that they tend to form along the margins of carbonate platforms when certain physico-chemical conditions are met (Duguid et al. 2010). These conditions are: 1. Presence of a nucleus. 2. Calcite or aragonite supersaturated water, and 3. An environment which allows for the degassing of CO<sub>2</sub> (Duguid et al. 2010). When the ooids are no longer accreting in suspension during higher-energy conditions, post-formation micritization can start (Diaz et al. 2017). The degree of micritization at this stage is then directly affecting the preservation potential of the crystallized laminae.

Anderson et al. (2020) recently proposed a model for larger ooids to form within sediment piles. This model uses modern day ooids as an example when stating that the threshold for ooids which grow in suspension is far smaller than more ancient ooids which have a larger diameter. Therefore, Anderson et al. (2020) makes the case that carbonate ooids with a larger diameter grow in dunes, where carbonate saturation state in the pore water is higher than the surround-

ing seawater.

In contrast to this, there have been a number of suggested models which argue that biological influence plays a key role in ooid formation. According to Dupraz et al. (2019), organisms which promote CaCO<sub>3</sub> precipitation can adjust pH conditions to more favorable ones for crystal nucleation. In Lake Geneva, modern fresh water ooids are formed due to the initial calcite precipitation by biofilms around a nucleus, making physico-chemical conditions almost irrelevant in this ooid formation process (Plee et al. 2008; Ariztegui et al. 2012). With lots of evidence pointing both for and against a biotic origin for ooids, it is safe to say that this is still a very much debated topic.

To better understand their formation, several studies have focused on the formation of ooids in present time. Modern day ooids are for example known from the Bahamas, the Great Salt Lake, and Baffin Bay, but can differ from ancient ooids in their size and mineralogy (Anderson et al. 2020). Modern day marine ooids are all aragonitic. This is due to modern day oceans being predominantly aragonitic, but the world's oceans have oscillated between being calcitic and aragonitic on scales of 100 -200 Myrs (Stanley & Hardie 1999). Ancient ooids vary between being dominantly calcitic and aragonitic, depending on the seawater chemistry at the time of formation. These differences between ancient and modern day ooids can result in difficulties when attempting to draw parallels between the two and compare how they are formed (Andersen et al 2020).

In addition to ooids, coated grains and cortoids have also been used as descriptive terms for rounded grains in the Wadi Ghalilah carbonate rocks. Coated grains refer to grains that do not display significant



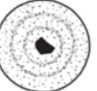
	Microfabric of the cortex	Mineralogy, modern examples	Environment
<b>Concentric (tangential) ooids</b> 	Concentric laminae consisting of tangentially arranged crystals whose long axes are aligned to the surface of the laminae. High microporosity	Aragonite: Bahamas, Yucatan, Abu Dhabi, Persian Gulf (Great Salt Lake/Utah)	Very shallow, warm low-latitude seas; <i>common in high-energy settings</i> Lacustrine-hypersaline
		Low-Mg calcite: Caliche ooids*	Terrestrial
<b>Radial (radial-fibrous) ooids</b> 	Laminae consisting of radially arranged crystals; long crystal axes perpendicular to the laminae surface	Aragonite: Persian Gulf, Great Barrier Reef, (Yucatan, Shark Bay, Mediterranean) Gulf of Aqaba Great Salt Lake/Utah	Shallow marine, <i>common in low-energy settings</i> Sea-marginal hypersaline pool Lacustrine-hypersaline
		Mg-calcite: (Baffin Bay/Texas)	Marine-hypersaline
		Calcite and Low-Mg calcite: e.g. Cave pearls*	Non-marine
<b>Micritic (random) ooids</b> 	Laminae composed of randomly arranged microcrystalline crystals or Laminae obliterated or absent, due to a pervasive micritization of the cortex	Aragonite: Bahamas	Shallow-marine

Figure 1. Flügel's description of the various types of ooids and their respective depositional environments (from Flügel 2010).



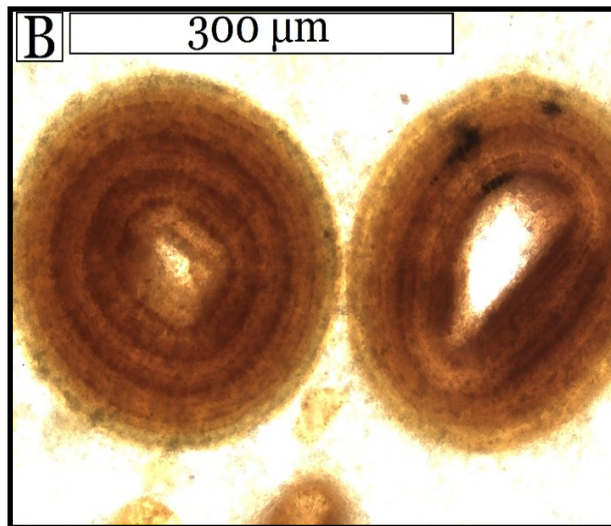


Figure 2. Concentric ooids from sample WG14 in this study.

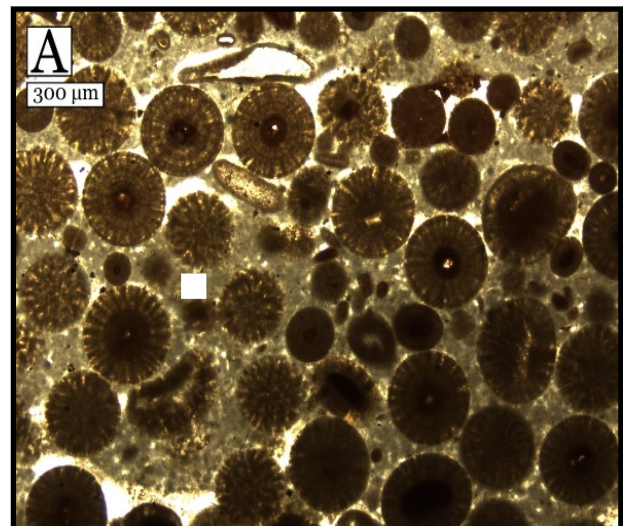


Figure 3. Radial ooids from sample WG19 in this study.

### 2.3 Microbialites

In two samples collected from Wadi Ghalilah, microbial buildups in the form of thrombolites can be observed. Thrombolites are stromatolite-related benthic microbes that range from freshwater to deep shelf settings (Flügel 2010) but differ from stromatolites in regards to their structure. Instead of exhibiting lamination like stromatolites, thrombolites have a macroclotted fabric, with clots referring to irregular carbonate outlines which often form long streaks and irregular patterns (Fig. 4).

Whereas different types of stromatolites have been observed in the sedimentological record since the Archean, thrombolites have only been observed since the Neoproterozoic (Riding 2011), but were important constituents to small-scale reef builders in the early Phanerozoic (Flügel 2010). After the Ordovician, thrombolites had a constant decline until the Permian and Mesozoic (Flügel 2010). Although increasingly rarer in the Phanerozoic, microbialite faunas are found dominating after certain extinction events (Calner 2005; Baud et al. 2007). This phenomenon is known as anachronistic carbonate facies.

### 2.4 Anachronistic facies

As previously stated, certain facies which were more frequently deposited during the Proterozoic and the early Paleozoic may become dominant for a time following Phanerozoic extinction events (Sepkoski et al. 1991). Examples of these kinds of facies are flat pebble conglomerates, large seafloor carbonate cements as well as microbial mats and ooids (Sepkoski 1991; Woods et al. 1999; Groves & Calner 2004). This has

for example been the case with the Silurian Lau event (Calner 2005) and the end-Permian mass extinction event (Baud et al. 2007), resulting in the deposition of anachronistic carbonate facies with microbial boundstones or widespread oolites. In the case of ooids, it has been speculated that the large stress a mass extinction event causes the marine environment results in alteration of carbonate precipitation (Groves & Calner 2004). The disappearance of many calcifying organisms thereby removes an important seawater carbonate sink, which allows for more inorganic ooid precipitation as well as widespread deposition of oolites in the aftermath of extinction events (Groves & Calner 2004).

Similar to post-extinction strata from other areas and times, the Sakhra Member includes thrombolites and oolites. It is not entirely known why this phenomenon occurs. Possibly, the abundance of metazoans during the Phanerozoic results in a decline of microbialites due to grazing and competitiveness. Under such circumstances a post extinction environment could be favorable for a sudden increase of microbialites, as this type of depositional environment resembles that of pre-Phanerozoic times when bioturbation was not as pronounced (Riding 2011). However, it is uncertain whether metazoans significantly affected the evolution of microbialites or not (Riding 2011).

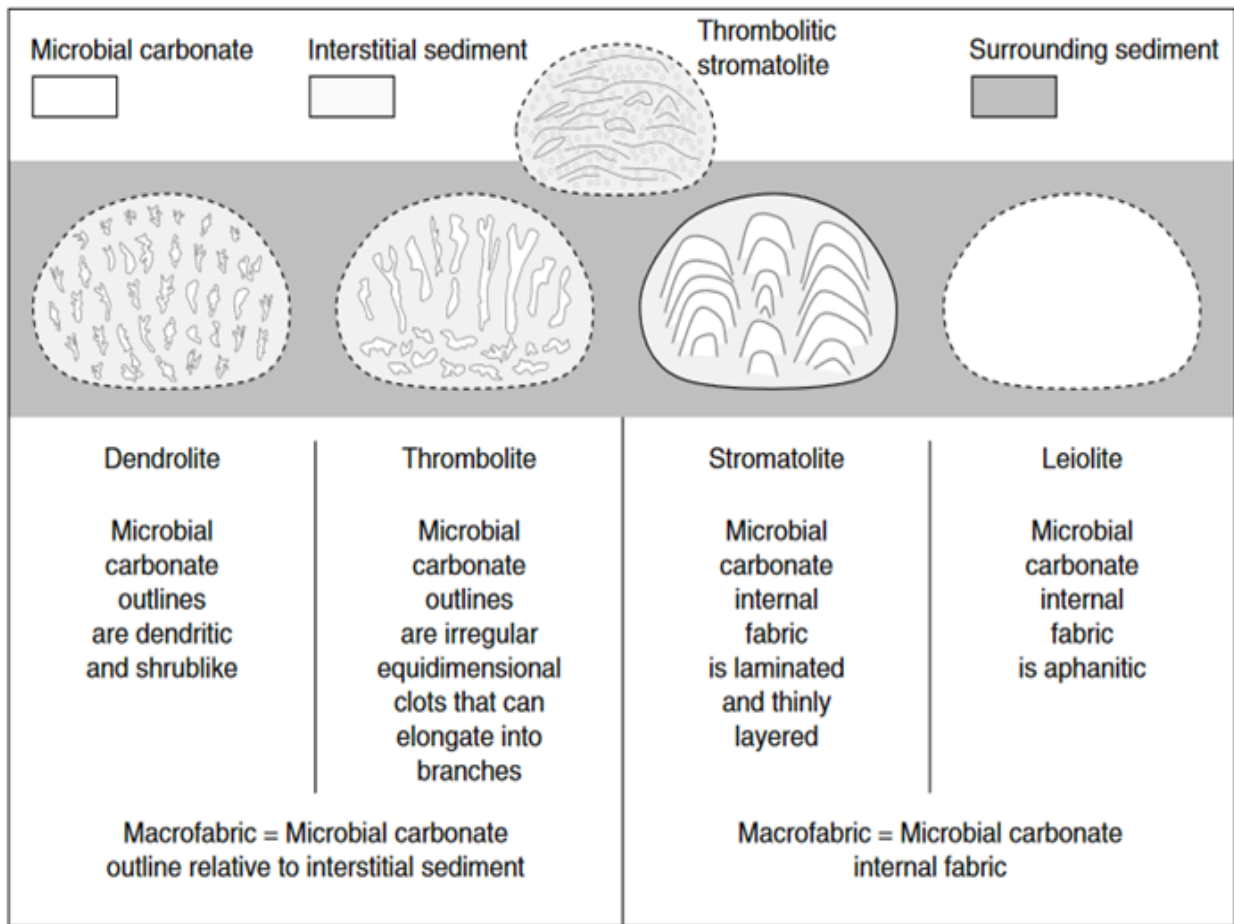


Figure 4. Different types of microbial buildups and their general distinctive appearances (Riding 2011).

### 3 Geological setting and stratigraphy

In the northeastern UAE, T-J boundary interval rocks outcrop in the Ras Al Khaimah and Musandam Mountains (Maurer et al. 2008), which separates the Gulf of Oman from the Arabian Gulf. During the Mesozoic, this modern-day mountain range was part of the tectonically stable southern margins of the Tethys Ocean, located around 20 degrees South of the Equator at this time, (Stämpfli & Borel 2002; Hönig 2017) where a tropical shallow marine carbonate platform subsequently developed (Maurer et al. 2008). This stable environment allowed for the deposition of over 3 km thick Permian and Mesozoic sediments (Maurer et al. 2008). Furthermore, paleogeographic reconstructions have shown that to the east an open marine carbonate shelf was present and to the west shallower settings occurred (Ziegler 2001; Al-Suwaidi et al. 2016; Ge et al. 2018, 2019). These shallow water carbonates are now exposed in west-verging thrust sheets, caused by the Cretaceous obduction of large slices of oceanic

lithosphere known as the Semail ophiolite (Roberts et al. 2016) (Maurer et al. 2008). Subsequent tectonic phases eventually resulted in the formation of the present day Musandam Mountains (Maurer 2008). In comparison to the nearby Oman and Zagros mountains, the Musandam Mountain range has undergone significantly less tectonic overprint (Maurer et al. 2008). It is here that the study area Wadi Ghalilah and the Ghalilah Formation is found (Fig. 5). Here, focus will be made on the post-extinction carbonate rocks of the uppermost Sumra and Sakhra Member at Wadi Ghalilah, with comparisons to results from the same Members at Wadi Milaha. A stratigraphic chart of the Ghalilah Formation at Wadi Ghalilah can be seen in Fig. 6, with photographs from the same locality in Figs. 7 & 8.

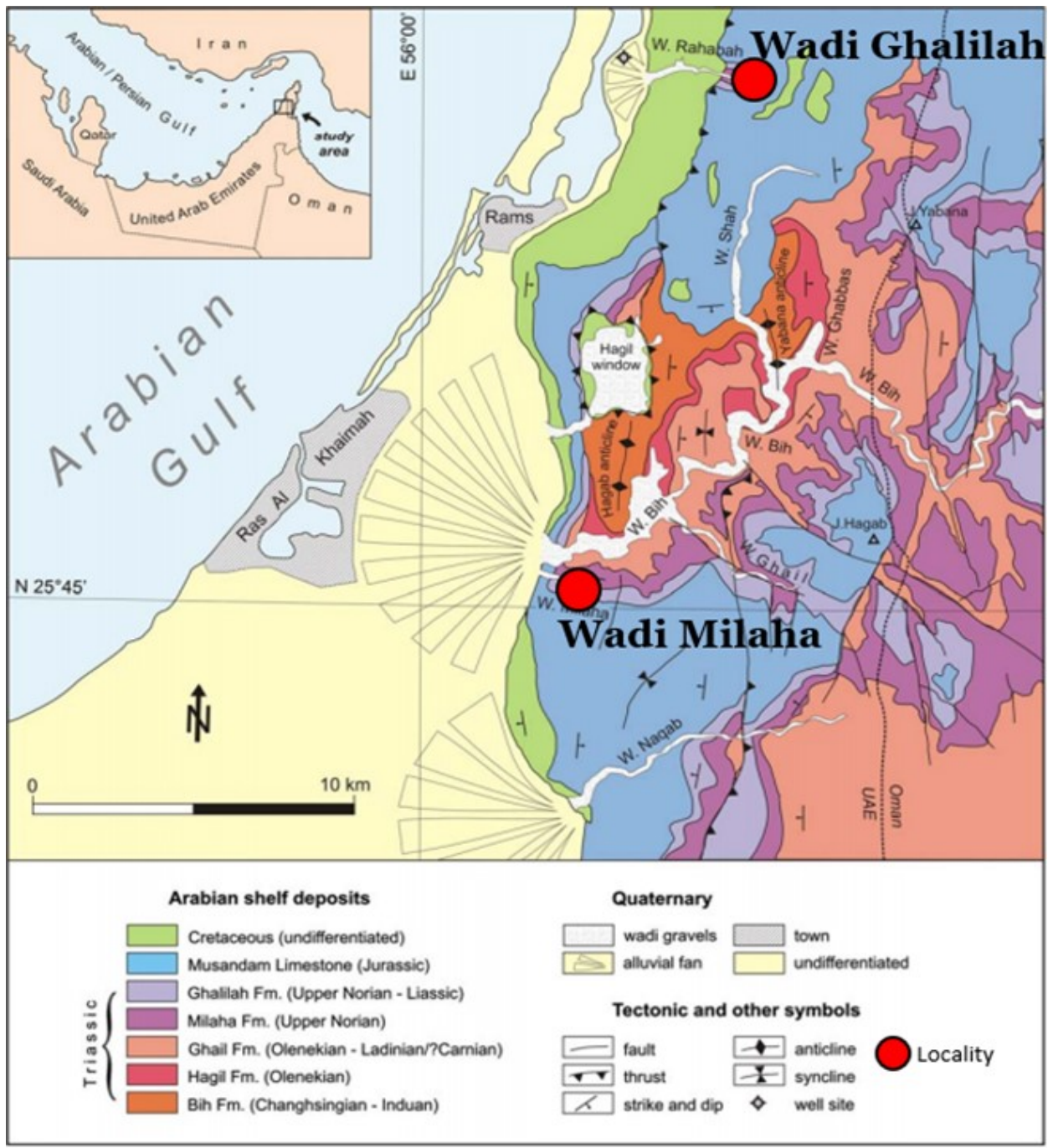


Figure 5. Overview of the Ras Al Khaimah area and the Musandam mountains in the UAE with Wadi Ghalilah and Wadi Milaha marked (Modified from Maurer et al. 2008)



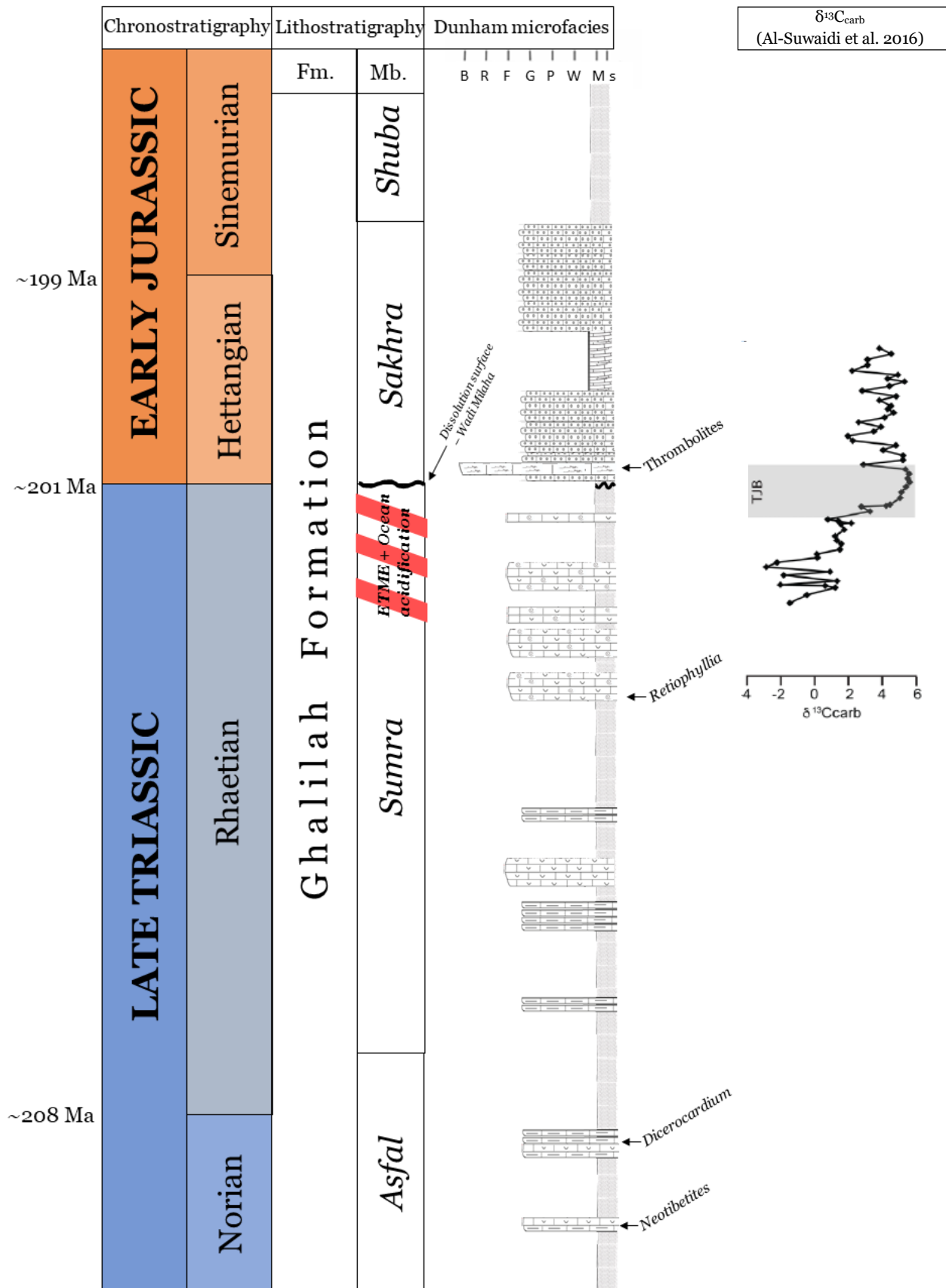


Figure 6. Stratigraphic chart of the Ghalilah Formation at Wadi Ghalilah, as interpreted in this study. The marked dissolution surface is however not observable at Wadi Ghalilah, but only at Wadi Milaha. Biostratigraphy is based on field observations and results from Maurer et al. (2008). The carbon isotope curve is from Al-Suwaidi et al. (2016) and may not correlate perfectly with this chart, but the negative CIE is still relatively coincident with the ETME. For a full reference on the CIE curve, see Al-Suwaidi et al. (2016).

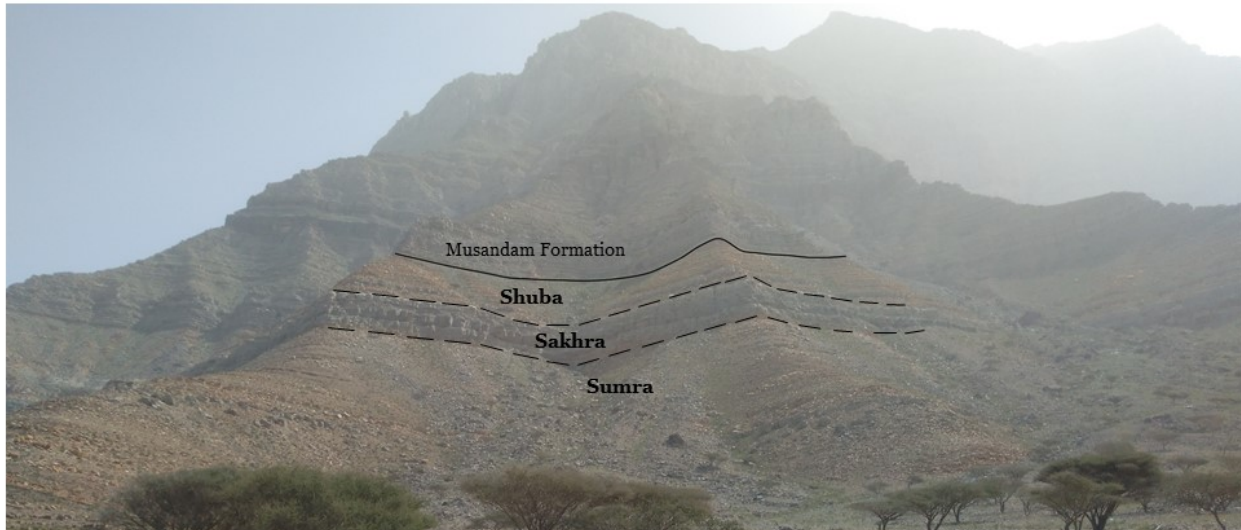


Figure 7. Overlook of the Sumra, Sakhra, and Shuba Members of the Ghalilah Formation and the overlying Musandam Formation, view towards the East.



Figure 8. Closer overlook of three of the stratigraphic members of the Ghalilah Formation: The Sumra, Sakhra, and Shuba Members. Overlying the Shuba Member is the Musandam Formation.

### 3.1 The Ghalilah Formation

The Ghalilah Formation is a mixed carbonate-clastic unit composed of four Members ranging from the late Norian to the Sinemurian; The Asfal, Sumra, Sakhra and Shuba Members. The Late Norian Asfal Member is

ca 120 m thick and constitutes brown and green marlstones along with quartz arenites with various carbonate intercalations. It is characterized by a typical Late Triassic fauna with gastropods, brachiopods, corals, bivalves as well as the ammonoid *Neotibetites* (Maurer et al. 2008). The overlying 60 m thick Sumra Member is lithologically similar to the Asfal, but lacks quartz arenites and is more fossiliferous with the top part consisting of floatstones with abundant coral and sponge debris (Maurer et al. 2018). In the overlying 25 m thick Sakhra Member there is a distinct change to less fossiliferous oolitic grainstones. The uppermost member of the Ghalilah Formation, the Shuba Member, is a 50 m thick unit composed of siltstones, dolomitic mudstones and marlstones, with a low macrofossil content (Maurer et al. 2008).

### 3.3 The Triassic—Jurassic boundary in the United Arab Emirates

Maurer et al. (2008) places the T-J boundary at the base of the Sakhra Member based on the disappearance of the Rhaetian coral-rich floatstone of the underlying Sumra Member and the transition into the poorly fossiliferous beds of the Sakhra and Shuba Members. This placement of the base of the Hettangian is also coincident with the results of Al-Suwaidi et al. (2016), where it is set after the negative CIE that defines the ETME. Hönig et al. (2017) on the other hand, place the T-J boundary in accordance with De Matos (1997) in the uppermost Shuba Member, close to the boundary of the overlying Musandam Formation. This placement was made after stratigraphic and biostratigraphic examinations led to the discovery of Liassic crinoids, as well as Triassic bivalves and shark teeth (De Matos 1997).

For this study, the same hypothesis as that of Maurer et al. (2008) and Al-Suwaidi (2016) will be followed, namely placing the T-J boundary at the base of the Sakhra Member following the negative CIE, as this is also the hypothesis used by my supervisors in their respective projects. The main arguments for this are that there is no sedimentological reason for the transition from the fossil rich Sumra Member into the fossil poor beds of the Sakhra Member, but must have rather been caused by the ETME. The lower parts of the Sakhra Member does not constitute a deep sea or hypersaline setting, which could have otherwise been reasons for the lack of fossils. Furthermore, the overall trend of a change from a regression in the Rhaetian to a transgression in the Hettangian is a globally recognized phenomenon (Pálffy et al. 2021) which can be seen in the lowermost Sakhra Member. Lastly, the fossils of the Sumra Member are already Rhaetian in age, and the transition into the Musandam Formation includes a pavement of typical Pliensbachian lithiotis bivalves. Therefore, placing the T-J boundary at the base of the Musandam Formation would mean that the Hettangian and Sinemurian is missing. Since this study aims to research post-extinction conditions, focus will be made on the Sakhra Member in particular with only the uppermost parts of the Sumra Member also being analyzed.

## 4 Methods

### 4.1 Field work in the United Arab Emirates

Field work was carried out by supervisors professor Sylvain Richoz and PhD student Ingrid Urban in January of 2020. A section of the Ghalilah Formation at Wadi Ghalilah was logged and described with samples collected from the uppermost Sumra Member and through the Sakhra Member. Samples 1 to 5 were collected from the Sumra Member and 6 to 44 from the Sakhra Member. The sample resolution was highest at the base of the Sakhra Member, where it was approximately 10 cm between each sample. The resolution was later lowered to about 33 cm between each sample. No samples were collected between 14 and 19 m due to the complete absence of oolites in this part of the formation.

### 4.2 Thin sections for optical microscope and LA-ICP-MS analyses

After macroscopic observation samples WG1, 6, 7, 8, 9, 11, 12A, 12B, 13, 14, 15, 17, 18, 19, 20, 23, 24, 25, 26, 27, 28, 29, 31, 33, 34, 35, 37, 38, 40, and 44 were selected for thin sectioning. Samples were cut using a Struers Discoplan-TS saw and the fresh surface was polished on a Struers Discoplan-25 with a 600 grit diamond plate. Then, a 5 mm thick slice was cut with the same dimensions of a glass slide used for the thin sections, which is about 28X48 mm. Each slab was then glued on a pre-grinded and signed glass slide with a bicomponent epoxy resin, in a proportion 15:2 between Struers' Epofix Resin and Epofix Hardener respectively. After drying the slabs for two days at room temperature, they were cut to a thickness of 1 mm using a higher precision Struers Discoplan-TS cutting and grinding machine. They were reduced to 40-35  $\mu\text{m}$  thick using the same machine and then polished with a 2000 grit diamond plate. In order to be analyzed at LA-ICP-MS, thin sections needed to be quickly pre-etched to be perfectly clean.

### 4.3 Optical petrographic microscope

Thin sections have been carefully described at the Geology Department at Lund University using an Olympus BX53 petrographic optical microscope, equipped with a digital camera (HD and Cam 6.3 series). 2X and 4X magnification with plane polarized light (PPL) was used to determine a number of characteristics in order to describe the samples. These were; lithology according to Dunham classification, corresponding standard microfacies (SMF) (Fig. 9), cement fabric, roundness scale of the grains (1-4 with 4 being the highest roundness, according to Flügel 2010), visual percentage scale (how much of the thin section surface area is covered in grains/bioclasts/oolids compared to matrix or cement), diagenetic effects, microfossil assemblage, porosity, binding stage (to what degree carbonate cement bound certain ooids together, on scales from 1 – 4 with 4 being the most connected, see WG19 B in Appendix 1 for an example of stage 4 binding stage of ooids) and more (according to Flügel, 2010). General sedimentary microstructures were also defined. Magnification 10X and 20X were used to classify ooids according to their morphological criteria (see chapter 2.2). To understand peculiar extinction patterns and mineral replacements, cross polarized light (XPL) was applied when necessary.



<p><b>SMF 1:</b> Spiculitic wackestone or packstone, often with calcisiltite matrix. Subtype emphasizes burrowing.</p> <p><b>SMF 2:</b> Microbioclastic peloidal calcisiltite with fine grainstone and packstone fabrics.</p> <p><b>SMF 3:</b> Pelagic lime mudstone and wackestones with abundant pelagic microfossils. Subtypes differentiate the groups of planktonic organisms.</p> <p><b>SMF 4:</b> Microbreccia, bio- and lithoclastic packstone or rudstone.</p> <p><b>SMF 5:</b> Allochthonous bioclastic grainstone, rudstone, packstone, floatstone, breccia with reef-derived biota.</p> <p><b>SMF 6:</b> Densely packed reef rudstone.</p> <p><b>SMF 7:</b> Organic boundstone. Subtypes try to differentiate the kind of contribution by potential reefbuilders to the formation of reefs and other buildups.</p> <p><b>SMF 8:</b> Wackestones and floatstones with whole fossils and well-preserved endo- and epibiota.</p> <p><b>SMF 9:</b> Strongly burrowed bioclastic wackestone.</p> <p><b>SMF 10:</b> Bioclastic packstone and wackestone with abraded and worn skeletal grains.</p> <p><b>SMF 11:</b> Coated bioclastic grainstone.</p> <p><b>SMF 12:</b> Limestone with shell concentrations. Subtypes characterize shell-providing fossils.</p> <p><b>SMF 13:</b> Oncoid rudstone and grainstone.</p> <p><b>SMF 14:</b> Lag deposit.</p> <p><b>SMF 15:</b> Oolite, commonly grainstone but also wackestone. Subtypes highlight the structure of ooids.</p> <p><b>SMF 16:</b> Peloid grainstone and packstone. Subtypes differentiate non-laminated and laminated rocks.</p> <p><b>SMF 17:</b> Grainstone with aggregate grains (grapestones).</p> <p><b>SMF 18:</b> Bioclastic grainstone and packstone with abundant and rock-building benthic foraminifera or calcareous green algae. Subtypes describe the systematic assignment of the various groups.</p> <p><b>SMF 19:</b> Densely laminated bindstone.</p> <p><b>SMF 20:</b> Laminated stromatolitic bindstone/boundstone.</p> <p><b>SMF 21:</b> Fenestral packstone and bindstone. Subtypes characterize fenestral voids and the contribution of calcimicrobes.</p> <p><b>SMF 22:</b> Oncoid floatstone and wackestone.</p> <p><b>SMF 23:</b> Non-laminated homogenous micrite or microsparite without fossils.</p> <p><b>SMF 24:</b> Lithoclastic floatstone, rudstone or breccia.</p> <p><b>SMF 25:</b> Laminated evaporite-carbonate mudstone.</p> <p><b>SMF 26:</b> Pisoid cementstone, rudstone or packstone.</p>
---

Figure 9. List of standard microfacies types. SMF 15 is further divided into 15C or 15R depending on if the ooids are concentric (C) or radial (R) (from Flügel 2010).

#### 4.4 Samples for SEM analyses

Following microscopy, it was concluded that samples WG8, WG11, WG12A, WG14, WG17, WG19, and WG20 would be analyzed with SEM. Small rock pieces were cut from each sample (5X5X8 mm). They were dried for one night in an air oven at 50 °C. The following day, the pieces were broken in two halves using a pincer to give the cubes the dimensions 5X5X4 mm. Each small cube was mounted on a SEM stub

with double-sided tape, with the fresh surface facing the detectors. To avoid charging effects, the lateral sides of the sample were sputter coated with 6 nm of Pt/Pd using a Cressington sputter coater 108 auto.

#### 4.5 SEM (Scanning Electron Microscope)

SEM analyses were performed at the Geology Department with a variable pressure Tescan Mira3 High Resolution Schottky FE-SEM equipped with an Oxford EDS detector, scanned at 5 kV. SEM images are observed in order to describe the morphology of laminae at microscale, as well as peculiar microstructures related to microbial interaction and diagenetic processes.

#### 4.6 LA-ICP-MS (Laser Ablation—Inductively Coupled Plasma—Mass Spectrometry)

LA-ICP-MS was carried out by Ingrid Urban and Dr. Tomas Naeraa, who gave all technical parameters. The thin sections WG8, WG11, WG12A, WG17, WG18, and WG20 were processed at the Geology Department with a Bruker Aurora- Elite Quadrupole ICP-MS, equipped with a 193 nm Cetac Analyte G2 excimer laser installed with a two volume HelEx2 sample cell with eQC. Samples were processed with a fluence of ca. 2 J/cm<sup>2</sup> and spot analyses between 45x95X50 µm and 37X116 µm with a repetition rate of 10 Hz were carried out. Spot analyses were preferred over line scans. He (0.8 l/min) was used as carrier gas, while Ar (0.95 l/min) was used as make-up gas. RF power was ca. 1300 W. For each analysis, background collection took 30 seconds, while the ablation process needed 30 seconds. Calibration was done with the internal standards NIST 610, NIST 612, NIST 614, and MACS-3. It had the following concentrations: MACS-3 (37.7 wt. %) and ooid (38 wt. %), with MACS-3 being a USGS reference material (Jochum et al. 2012). Data reduction was done with Iolite software (Paton et al. 2011).

Stable isotopes of a number of different elements, both major and trace, were analyzed. Mg<sup>26</sup> as a major element, to verify the bulk composition of ooids (high-Mg calcite, low-Mg calcite, aragonite, dolomite). Among the trace elements, the following were considered: Sr<sup>88</sup>, in order to better discriminate between aragonite and calcite composition of the carbonates (Sandberg 1983). Al<sup>27</sup> and Ti<sup>49</sup> to check for any possible contaminations by silicates. Ba<sup>137</sup>, U<sup>238</sup>, and Zn<sup>66</sup> to correlate the ooids' interaction with organic matter and/or bacteria (Smith et al. 1999; Riding 2006; Kamber & Webb 2007; Newsome et al. 2014; Li et al. 2017). U<sup>238</sup>, Mn<sup>55</sup>, P<sup>31</sup> in order to investigate whether oxic or anoxic conditions were present in the sea water, and to what extent (Klinkhammer & Palmer 1991; Newsome et al. 2014. Rare Earth Elements

(REE) and Yttrium (Y) were analyzed for different purposes: as indicators for relative water depths (Piepgras & Jacobsen 1992), redox conditions (German & Elderfield 1990), microbial activities (Takahashi et al. 2005; 2007), early diagenetic processes (Haley et al. 2004), and contaminations from silicates (Li et al. 2017). Yttrium is often analyzed together with REE as the element frequently occurs in REE deposits.

The particular samples were chosen based on their relatively low degree of micritization, ensuring that the elements analyzed came from as unaltered sources as possible. Analyzes were grouped into four categories: 1. Nucleus, 2. Cortex/Laminae (sub-divided into concentric or radial), 3. Cortoids, 4. Cement. Several ablations also occurred on single ooids, from the nuclei to the edge of the cortex. These so-called transects were made to analyze the variation of trace elements in different parts of the cortex, thereby providing information of elemental changes that occurred on a yearly or decadal interval. The nucleus itself is examined to understand its origin, for example if it derives from a siliciclastic input.

#### 4.7 Processing of LA-ICP-MS data

The data from the analyses were processed using Iolite software and Microsoft Excel, where the Calcium weight percentage (Ca wt%) was set to 40% as an internal standard. Data was processed so that any outliers were removed, and that only data from the time the spots were being made were analyzed. The internal and external errors for the values were also calculated and taken into consideration when producing graphs. Due to Ca ions having a similar charge and size as, Mg, Mn, Sr, and Al, it is possible that these three first elements can replace Ca in Calcite (CaCO<sub>3</sub>), and that Al can bond with O to produce silicates.

To solve this, the new (true) Ca wt% (*Ca wt%<sub>n</sub>*) value is recalculated using the formula:

$$Ca\ wt\%_n = Ca\ wt\%_o \times \frac{100}{40} + \left( \frac{Mg\ ppm \times \frac{uMgCO_3}{uMg} + Mn\ ppm \times \frac{uMnCO_3}{uMn} + Al\ ppm \times \frac{uAl_2O_3}{Al_2} + Sr\ ppm \times \frac{uSrCO_3}{uSr}}{10000} \right)$$

Where *u* is referred to the atomic weight of the element or compound, *Ca wt%<sub>o</sub>* is the old Ca wt% (i.e. 40%), and *ppm* is the initially measured concentration of the elements in parts per million.

The new concentration values in ppm for the elements were then achieved using the following equation:

$$ppm_n = ppm_o \times \left( \frac{Ca\ wt\%_n}{Ca\ wt\%_o} \right)$$

Where *ppm<sub>n</sub>* is the newly calculated concentration, and *ppm<sub>o</sub>* is the old concentration before adjustments to the *Ca wt%<sub>n</sub>*.

The REE + Y concentrations are then normalized to the Post Archean average Australian Shale (PAAS) concentration values, which are concentrations based on the average of 23 Australian shales of post Archean age (McLennan 1989; 2001). This was also used for correlation to Wadi Milaha samples, by applying the equation:

$$ppm_{nPAAS} = \frac{ppm_n}{PAAS\ value}$$

Where *ppm<sub>nPAAS</sub>* is the new concentration normalized to PAAS, and *PAAS value* is the concentration values based on the 23 Australian shales previously mentioned. This last adjustment is as aforementioned only applied to the REE + Y.



After  $ppm_{nPAAS}$  for every REE has been calculated, it is possible to use these new values to further draw conclusions about redox conditions in the water column at the time of the oolites' deposition. Due to the oxidization of  $Ce^{3+}$  to  $Ce^{4+}$  in oxic settings, a negative or positive Ce anomaly compared to PAAS normalization constitutes a proxy for redox conditions in marine settings (German & Elderfield 1990; Shields & Stille 2001). A negative anomaly indicates an oxygenated environment, whereas a positive anomaly indicates an anoxic or increasingly dysoxic one (German & Elderfield 1990; Shields & Stille 2001). This can be investigated further by using the REE values normalized with PAAS and applying the formula:

$$\frac{Pr_{PAAS}}{0,5Ce_{PAAS} + 0,5 Nd_{PAAS}}$$

Where,  $Pr_{PAAS}$ ,  $Ce_{PAAS}$ , and  $Nd_{PAAS}$  are the  $ppm_{nPAAS}$  values for Pr, Ce, and Nd. As suggested by Bau & Dulski (1996), ratios of  $> 1$  using this formula are indicative of oxygenated environments, and ratios of  $< 1$  imply a more dysoxic environment.

## 5 Results

### 5.1 Logs of the outcrop

The log for the Sumra Member (Rhaetian) is shown in figure 10, the Sakhra Member (Hettangian) in figure 11, and a legend in figure 12.

#### 5.1.1 Log of the uppermost Triassic Sumra Member (Rhaetian)

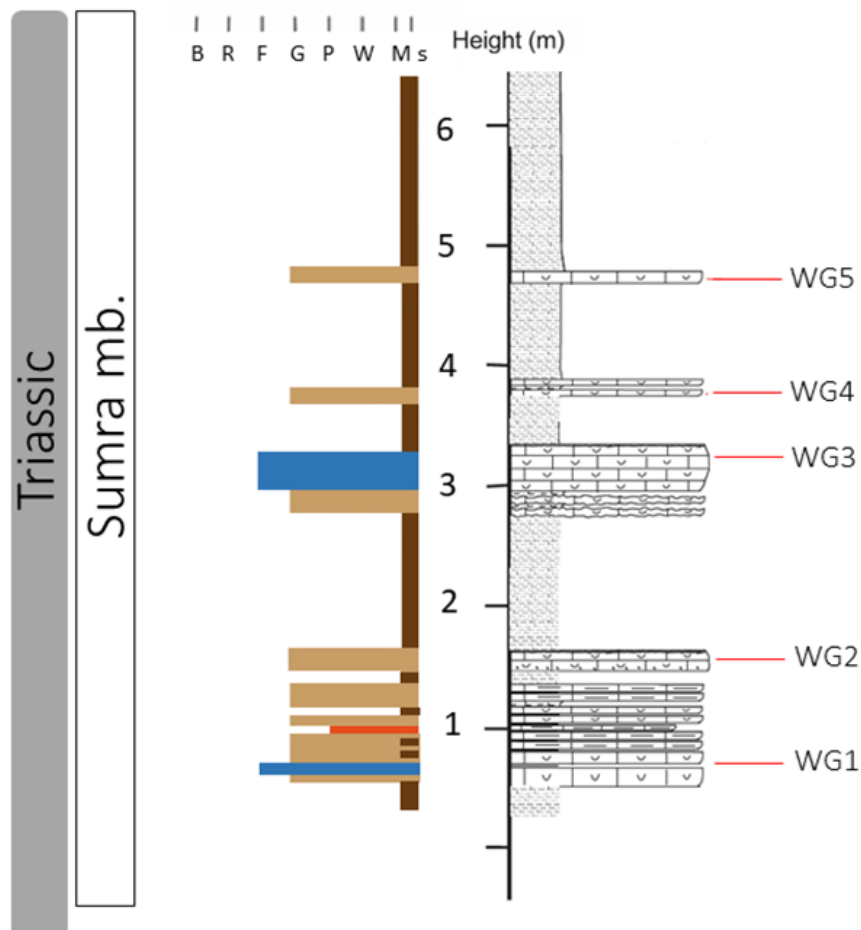


Figure 10: Log of the uppermost Triassic (Rhaetian) Sumra Member.

5.1.2 Log of the Jurassic Sakhra Member (Hettangian)

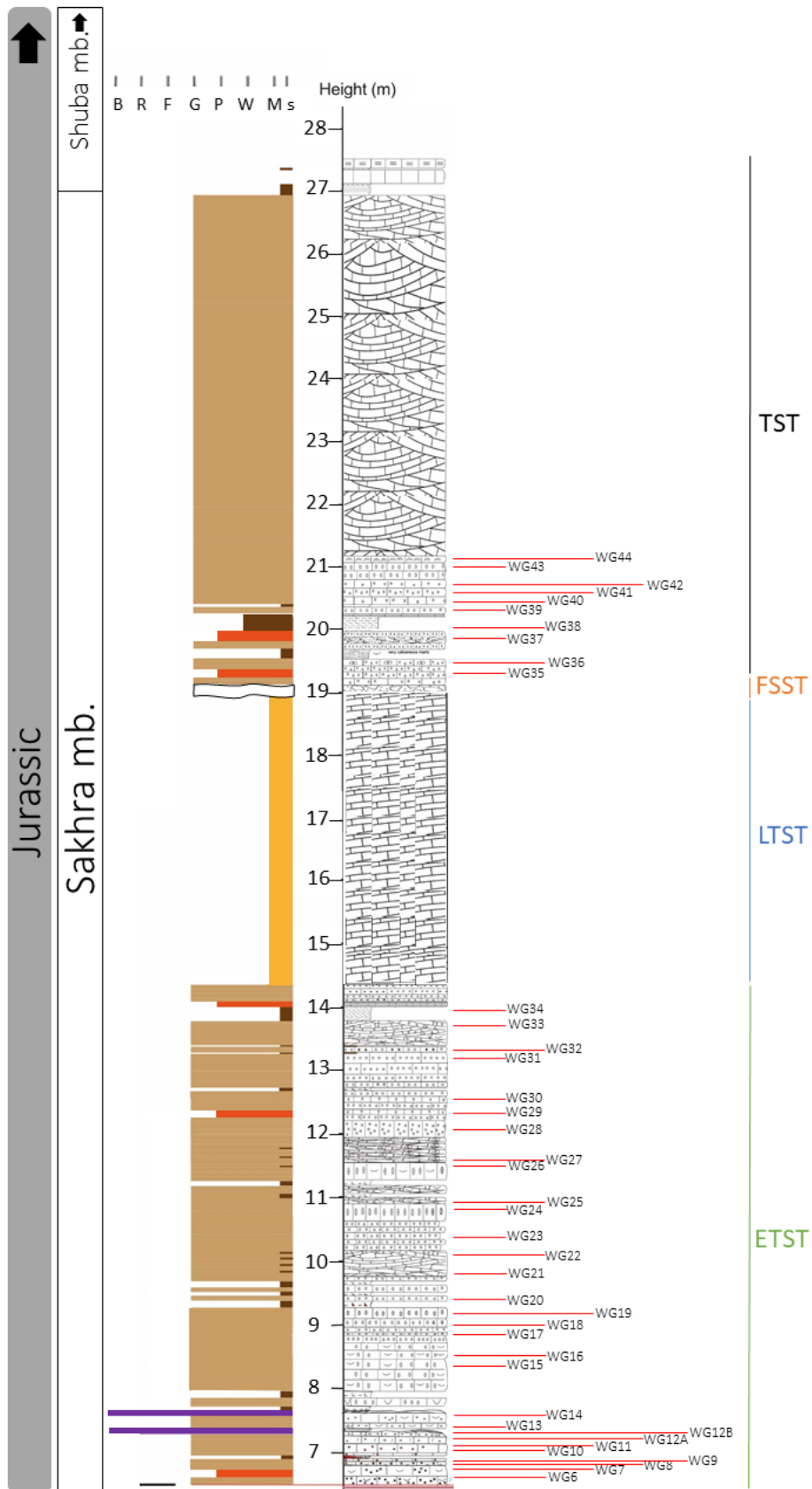


Figure 11: Log of the Sakhra Member at Wadi Ghalilah with sample sizes and interpreted sequence stratigraphical boundaries marked.

### 5.1.3 Legend for the logs

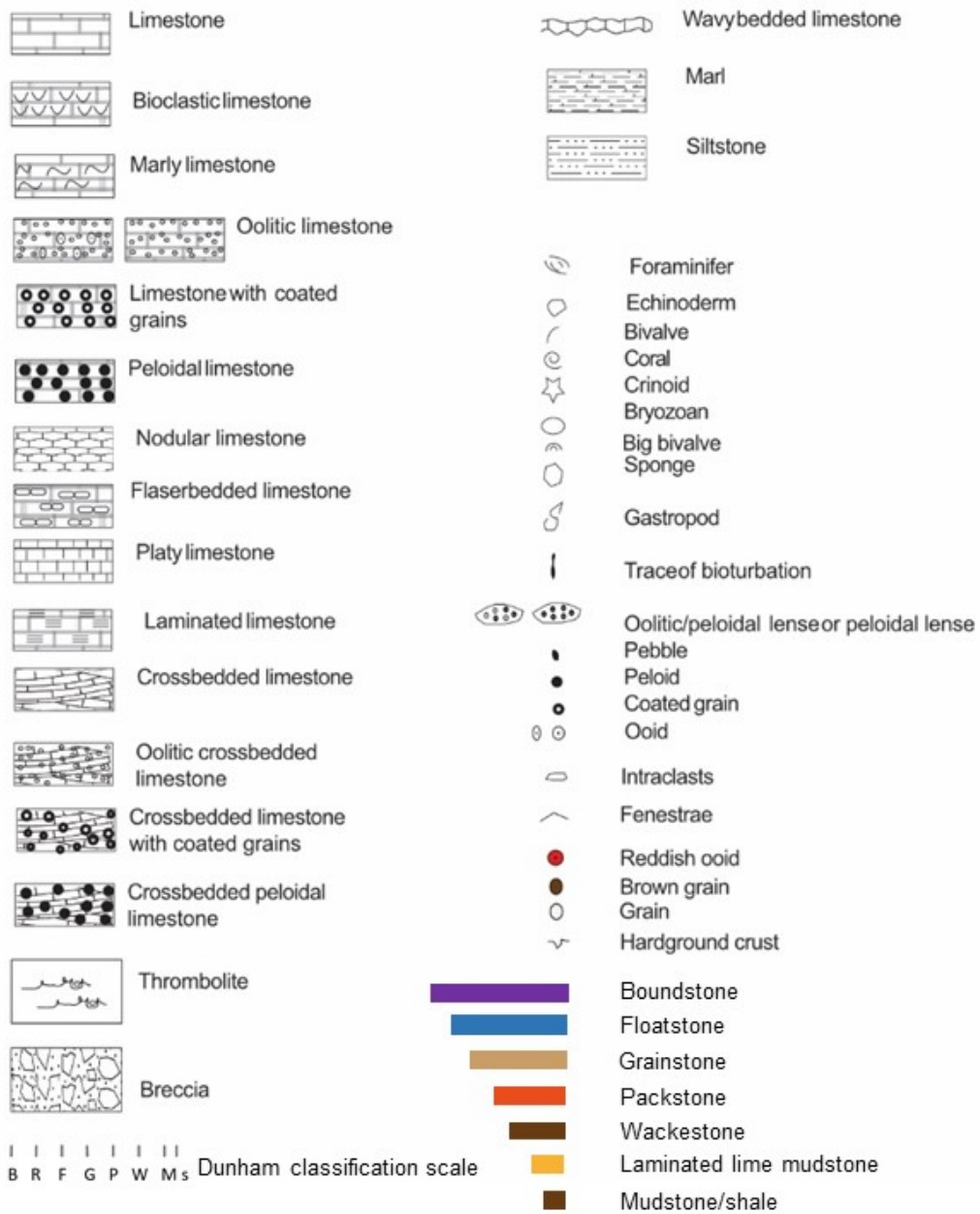


Figure 12: Legend for both of the logs.

## 5.2 Petrographic descriptions and interpretations of the Wadi Ghalilah samples

Associated images for all thin sections can be found in Appendix 1. For sample levels, see Figs. 10–11.

WG 1 – SMF: 12. Lithology: Floatstone. Sorting: moderately sorted. Roundness scale: 2. Visual percentage scale 10%.

The sample is fossiliferous with foraminifera, bivalve shells, ornamented gastropods, and more microfossils which have sharp contacts to the surrounding fine-grained matrix. Calcite filled cracks fissures are observable together with inclusions of pyrite and oxides, as well as stylolite associated porosity.

WG 6 – SMF: 10. Lithology: Packstone with abundant peloids. Sorting: poorly sorted. Roundness scale: 2-3. Visual percentage scale: 40%.

The sample includes gastropods as well as bivalves together with several cortoids. Small scale stylolites are also present. Many particles and microfossils have been replaced with calcite.

WG7 – SMF: 15C. Lithology: Grainstone. Sorting: well/moderately sorted. Roundness scale: 4. Visual percentage scale: 60%. Cement fabric: Mainly mosaic (equant/granular) as well as isopachous around some of the grains. Binding stage: 4. Porosity: Mainly sheltered porosity behind the larger bivalves.

Apart from ooids and cortoids, the sample includes a high degree of coated and rounded grains. Bivalve shells and brachiopods are present as well as aggregate grains, which have likely been transported given the sharp contacts to the surrounding sediment. Mineral replacements occur in the form of calcite, particularly observable in the microfossils.

WG8 – SMF: 15C. Lithology: Grainstone. Sorting: Well sorted. Roundness scale: 4. Visual percentage scale: 60%. Binding stage: 2. Cement fabric: Blocky. Porosity: sheltered and moldic.

The cortoids and skeletal fragments in the sample have been heavily micritized. Bivalves with infilling of micrite can also be observed, which at often times have been recrystallized.

WG9 – SMF: 11. Lithology: Grainstone. Sorting: Very well sorted. Roundness scale: 4. Visual percentage scale: 50%. Cement fabric: Blocky and isopachous rims along the grains.

The grainstone includes a high amount of small scaled coated grains. There are many stylolites throughout as well as elongated larger grains with a high degree of micritization, which have some form of lamination. Large bivalve shells and a possible foram/

gastropod together with cortoids can also be observed.

WG11 – SMF: 15C. Lithology: Grainstone. Sorting: Moderately sorted. Roundness scale: 3-4. Visual percentage scale: 30%. Cement fabric: Isopachous rims. Porosity: Sheltered porosity as well as fracture and stylolite associated.

The sample consists of concentric ooids and cortoids. Some transport and secondary coating have occurred which is the cause for many of the sharp boundaries. Intraclasts are present due to early diagenesis, which would have made these ooids protected from second, later stage diagenesis. Pyrite grains are abundant, particularly within larger fractures. The cracks themselves do not go through the ooids, but rather around them.

WG12A – SMF: 15C. Lithology: Grainstone Sorting: very well sorted. Roundness scale: 4. Visual percentage scale: 60%. Binding stage: 4. Cement fabric: Broken blocky cement, with no clear boundaries or rims around the ooids. Porosity: Sheltered by bivalves.

The concentric ooids in the sample have undergone severe diagenetic alteration where they have started to reach a lumping stage, as well as fitted-fabric-like patterns with stylolites. Cortoids and bivalve shells can still be identified. Pyrite grains are also prominent throughout as well as mineral replacements in the form of calcite.

WG12B – SMF: 7. Lithology: Thrombolithic boundstone.

The sample constitutes microbial build ups with pyrite throughout. The grey areas are micritic, and some bivalves and ostracods can be observed within the thrombolites.

WG13 – SMF: 11. Lithology: Packstone Sorting: Moderately to poorly sorted. Roundness scale: 4. Visual percentage scale: 20%. Porosity: Sheltered. Cement fabric: Blocky/mosaic cement which only occurs in fractures, which does not designate the sample as a grainstone.

The packstone has undergone a high degree of micritization, and likely includes remnants of thrombolites as in some parts similar microbial fabric from WG12B can be observed. The sample goes into a higher energy environment compared to WG12B, which can indicate some hiatus due to the change in environment. Some clear concentric ooids, large bivalves and cortoids are also present.

WG14 – SMF: 7. Lithology: Thrombolithic boundstone.

The sample has a varying degree of micritization, although not particularly heavy. In addition to the microbial fabric which is clotted, scattered and well developed concentric and superficial ooids together with pyrite grains are present, but rare.

WG15 – SMF: 11. Lithology: Coated bioclastic grainstone. Sorting: Poorly sorted. Roundness scale: 3. Visual percentage scale: 30%. Cement fabric: Blocky mosaic.

The sample includes a high degree of micritized bio- & lithoclasts, mostly peloids. It also contains many elongated skeletal parts and cortoids which are significantly larger than the micritized grains. Oncoids are present together with gastropods, bivalves, echinoderms, and some larger brachiopods.

WG17 – SMF: 15R. Lithology: Grainstone. Sorting: Very well sorted. Roundness scale: 4. Visual percentage scale: 60%. Cement fabric: Blocky mosaic.

Some smaller cracks going through both cement and ooids can be observed, which is the result from compaction after lithification. There is little to no micrite, which could be indicative of a high energy environment.

WG18 – SMF: 15R. Lithology: Grainstone. Sorting: Very well to well sorted. Roundness scale: 4. Visual percentage scale: 50%. Binding stage: 2. Cement fabric: Blocky with isopachous rims.

Radial ooids are dominating in the sample and there are very few to no superficial or concentric ooids observable. There has likely occurred some transport of smaller grains, as they differ from the larger ooids which makes up the main part of the sample.

WG19 – SMF: 15R. Lithology: Grainstone. Sorting: Very well sorted. Roundness scale: 4. Visual percentage scale: 50%. Binding stage: 4. Cement fabric: Blocky.

The radial ooids have various shapes and sizes including asymmetrical/eccentric, distorted/deformed, half-moon/shrunken. There are also prominent skeletal fragments and cortoids. Peloids occur in between the ooids together with bivalves and small particles of transported extraclasts. Compared to WG18 there is more micrite which might indicate a transition to a lower energy environment.

WG20 – SMF: 15R. Lithology: Grainstone. Sorting: Very well to well sorted. Roundness scale: 4. Visual percentage scale: 50%. Binding stage: 1-2. Cement fabric: Blocky and mosaic.

A number of the more developed radial ooids are mixed with smaller coated grains. Bivalve shells and cortoids are also present.

WG23 – SMF: 11. Lithology: Peloidal grainstone. Sorting: Very well sorted. Roundness scale: 4. Visual percentage scale: 50%. Binding stage: 1-2. Cement fabric: Isopachous and blocky.

The sample constitutes heavily micritized coated grains, with lots of cement and bioclasts. A few

superficial micritized ooids are also present.

WG24 – SMF: 11 Lithology: Grainstone. Sorting: Very well sorted. Roundness scale: 4. Visual percentage scale: 60%. Cement fabric: Blocky.

The sample has a gray homogenous color of both grains and cement, with some red color streaks in the sample might suggest iron-enriched porewater seeped through. All grains are coated, but no real ooids are actually present.

WG25 – SMF: 15R. Lithology: Grainstone. Sorting: Moderately sorted. Roundness scale: 4. Visual percentage scale: 60%. Cement fabric: Isopachous.

Radial and superficial ooids are present, and the sample shows signs of diagenetic processes such as cracks filled with secondary cement and calcite. Skeletal parts and shells of bivalves can also be observed.

WG26 – SMF: 15R. Lithology: Grainstone. Sorting: Very well sorted. Roundness scale: 4. Visual percentage scale: 50%. Binding stage: 3. Cement fabric: Isopachous, probably drusy mosaic.

Some of the ooids in the sample are superficial, others deformed and elongated. Several skeletal grains and cortoids are also visible. Compared to the two previous samples, the ooids are becoming more developed here.

WG27 – SMF: 15R. Lithology: Grainstone. Sorting: Moderately sorted. Roundness scale: 4. Visual percentage scale: 40%.

Very few skeletal parts are present, however they are normally larger than the ooids. Calcite crystals are visible in XPL, and in the lower part of the thin section the color of ooids switches distinctively to red and the cement fabric is more mosaic in nature. A large bivalve shell is also visible in this red part even on a macroscopic scale.

WG28 – SMF: 11. Lithology: Grainstone. Sorting: Moderately to poorly sorted. Roundness scale: 3. Visual percentage scale: 60%. Porosity: Sheltered. Cement fabric: Mosaic/isopachous

Skeletal parts are abundant in the sample, along with mainly peloids and coated grains which are often elongated and heavily micritized.

WG29 – SMF: 10. Lithology: Packstone. Sorting: Very well to well sorted. Roundness scale: 4. Visual percentage scale: 40/60%. Porosity: Sheltered.

The abundant cortoids and skeletal fragments like the coated bivalve shells in the sample seem to be aligned laterally, which might indicate water flow direction or be the result of diagenetic compaction processes. Given the difference in size between the grains in the sample and the alignment of the larger grains

however, it is safe to assume a flow direction rather than diagenetic processes being the reason for this alignment.

WG31 – SMF: 11. Lithology: Grainstone. Sorting: Well sorted. Roundness scale: 4. Visual percentage scale: 60%. Binding stage: 4. Cement fabric: Blocky.

There are coated grains throughout the sample with a heavy degree of micritization and very few cortoids. Stylolites have also formed indicating diagenetic alteration.

WG33 – SMF: 15C. Lithology: Grainstone. Sorting: Very well sorted. Roundness scale: 4. Visual percentage scale: 60%. Binding stage: 3. Cement fabric: Mosaic

Concentric ooids are dominating but most are micritized which makes distinguishing difficult. Some ooids and coated grains have been replaced with calcite crystals. These calcite crystals are very abundant throughout the sample and can be easily seen, especially in XPL. Sample contains little to no skeletal parts, but some pyrite grains are present.

WG34 - SMF: 3. Lithology: Mudstone/wackestone almost entirely of peloidal micrite. Pyrite grains as well as red-colored stylolites can be observed which are filled with clay minerals.

WG35 – SMF: 18-For. Lithology: Peloidal bioclastic packstone. Sorting: poorly to moderately sorted. Roundness scale: 4. Visual percentage scale: 30-50%. Binding stage: 1.

The sample includes abundant benthic foraminifera, bivalves, and gastropods, as well as cracks filled with cement. Sharp boundaries between the bio and lithoclasts are due to transport, and the transported clasts all have a significantly higher peloid count.

WG37 – SMF: 16. Lithology: Non laminated peloidal packstone. Sorting: Moderately sorted. Roundness scale: 4. Visual percentage scale: 60%

The sample mainly consists of coated bioclastic grains with heavily micritized ooids, remnants of bivalve shells, abundant peloids, and pyrite.

WG38 – SMF: 3. Lithology: Peloidal wackestone. There is a heavy degree of micritization together with stylolites cutting through the sample with inclusions of clay minerals and oxides.

WG40 – SMF: 11. Lithology: Grainstone. Sorting: very well sorted. Roundness scale: 4. Visual percentage scale: 50%

Coated grains with a high degree of micritization together with bivalve shells and cortoids are the

main constituents of this sample.

WG44 – SMF: 15C. Lithology: Grainstone Sorting: Very well sorted. Roundness scale: 4. Visual percentage scale: 50/60%.

The sample includes predominantly superficial concentric ooids and a varying degree of micritization. This is a distinct change in energy from WG40 where it goes from smaller grain sizes to larger. Bivalves and gastropods are present, with some bivalve shells even being macroscopic.

### 5.3 Summary of thin section observations

The vast majority of the analyzed samples are represented by oolitic grainstone with very few to no microfossils. The microfossils are almost entirely composed of bivalves, and it is only the thrombolites and the later occurring foraminifera which seemingly breaks this trend. The ooids are mainly concentric in the lower part of the Sakhra Member and transitioning into radial after the first few meters. All ooids have been classified as either concentric or radial, without designating micritic ooids. Although several samples have endured higher degrees of micritization, the ooids' laminae have not been completely obliterated by this micritization, as distinguishing the crystal orientation is still possible.

The vast majority of the samples are well-sorted with a high roundness scale, and the main cement types are mainly alternating between blocky and isopachous. Mosaic cement becomes more common towards the top of the member but is far less common than blocky and isopachous.

Furthermore, micritization throughout the samples appear to be oscillating in three intervals, which will be described in the next segment.

### 5.4 Micritization intervals

In regards to the observed thin sections, there are three apparent micritization intervals distinguishable. In these intervals, the laminae of ooids as well as the surrounding matrix and cement, transition from having been exposed to a high degree of micritization into being less affected by micritization (i.e. more clear and distinguishable features in the sample), and finally back to being more micritized further up in the section. These micritization intervals have been named MI 1, MI 2, and MI 3 (Fig. 13), and they all follow the same previously described “cyclicality” or interval changes. The three cycles range from WG 7 to WG 17 for MI 1, WG 17 to WG24 for MI 2, and WG 24 to WG 33 for MI 3, where after this these types of intervals are non-observable.

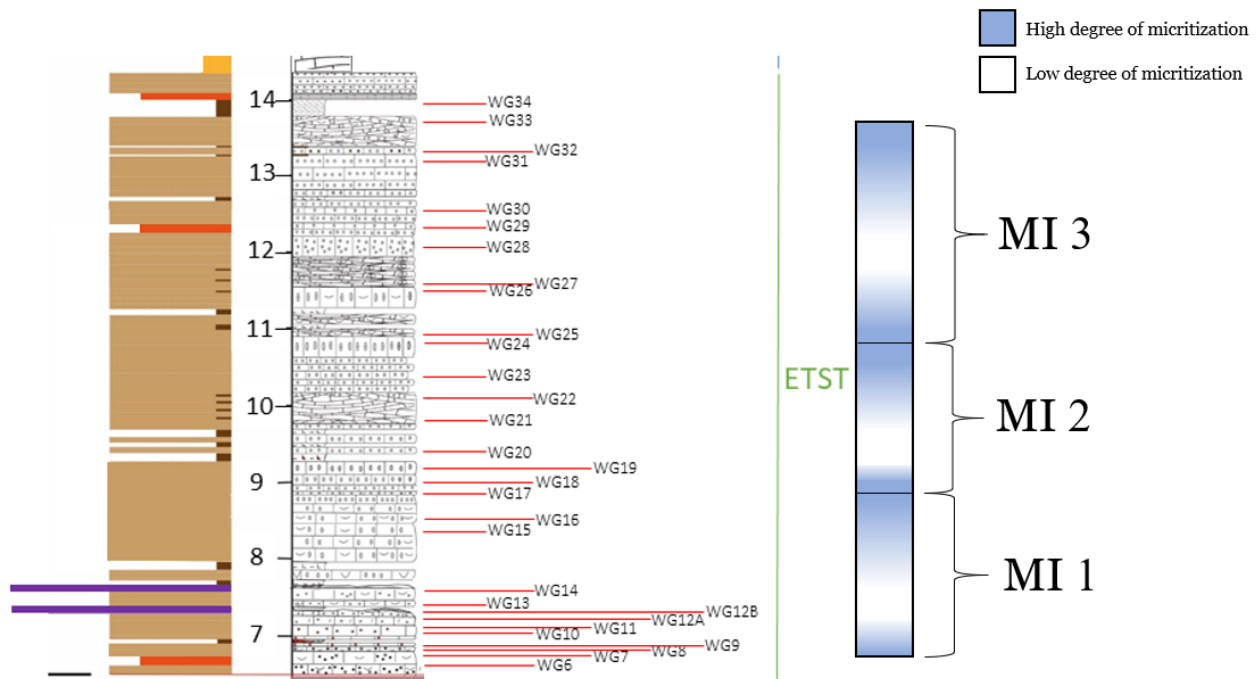


Figure 13: The three described Micritization Intervals ranged between WG7 – WG17 (MI 1), WG17 – WG24 (MI 2), and WG24 - WG33 (MI 3). Each interval starts with a sample with a high degree of micritization, transitioning into samples with lower micritization before ending with high degrees of micritization again.

## 5.5 Sequence stratigraphy

Sequence stratigraphy has been interpreted for the Sakhra Member at Wadi Ghalilah and is marked in the log at chapter 5.1.2. The Sakhra Member constitutes an early transgressive systems tract (ETST) in the first 7 m. Following this, the 5 m of laminated lime-mudstone is interpreted to indicate the gradual transition into a late transgressive systems tract (LTST). Above this mudstone there is a thin layer of breccia, which is here interpreted as a brief period of a falling stage systems tract (FSST). The overlying final meters of the Sakhra Member indicates the start of a new transgressive systems tract (TST) which can be observed into the overlying Shuba Member. The sequence stratigraphy will be further discussed in chapter 6.3.

## 5.6 SEM

Conducting SEM analyses of the samples WG8, WG11, WG12A, WG14, WG17, WG19, and WG20 had the goal of describing the morphology of laminae at microscale, as well as peculiar microstructures related to microbial interaction and diagenetic processes. Compared to the optical microscope, the micritization made it far more difficult for classifying the ooids in SEM, as it proved difficult to observe any particular crystallographic orientations. An example of this is WG12A, where concentric lamination of the ooid cor-

tex can be observed clearly in the optical microscope, although not in the SEM (Fig. 14). Ooids in other samples were simple enough to locate in the SEM, however there were few new conclusions to be drawn from this. Examples of this are the radial ooids in WG19 and WG20. Although very clear in the optical microscope, the radial lamination in WG19 and WG20 was not easily distinguishable in the SEM and if classification of these ooids would have been made judging from only SEM, they would have been distinguished as micritic or concentric (Figs. 15 & 16). However, the optical microscope should be favored in this situation. This is because there are clear radial orientations of the crystal structure visible in the optical microscope. Such clear lamination could not have been induced by microborers, but was rather created when the ooids were formed in suspension. Micritization of the laminae would almost completely obliterate the crystal orientation of the calcite growth, and not be so perfectly aligned as we see in the optical microscope.

In samples WG8 (Fig. 17) and WG11 (Fig. 18) ooids were unfortunately cut off in a way that any meaningful conclusions could be drawn. In WG14 (Fig. 19), the thrombolithic fabric which is seen also in the optical microscope was dominant, but the clear ooids which were found at parts throughout this fabric could not be observed in SEM.



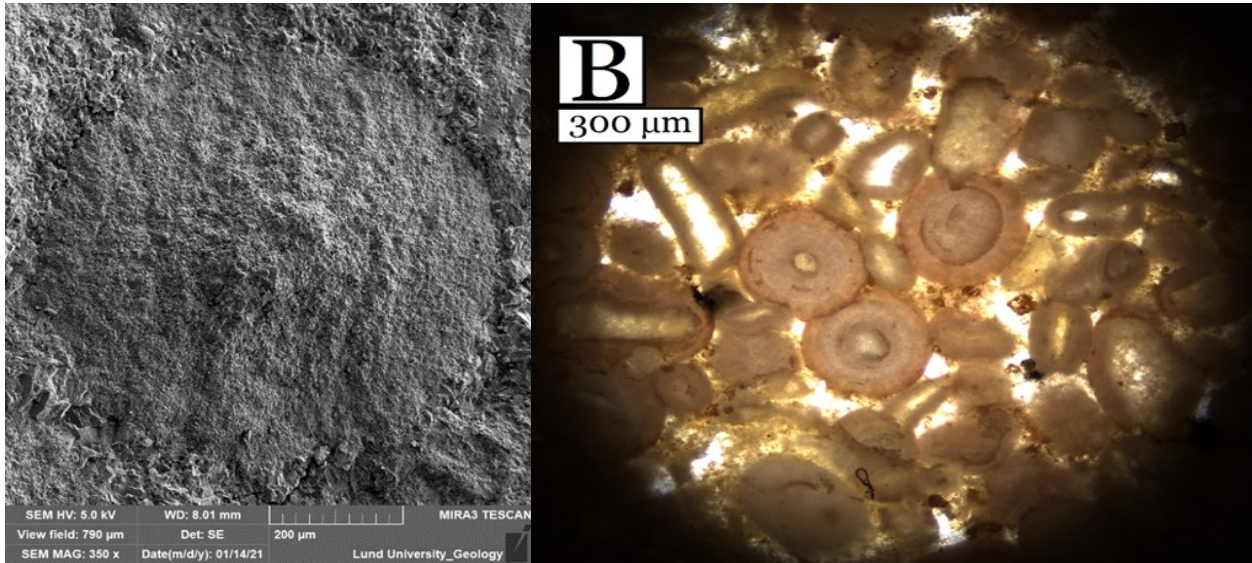


Figure 14: Concentric ooid in sample WG12A in SEM (left). The concentric crystallographic orientation is not visible in SEM, but more clear in the optical microscope.

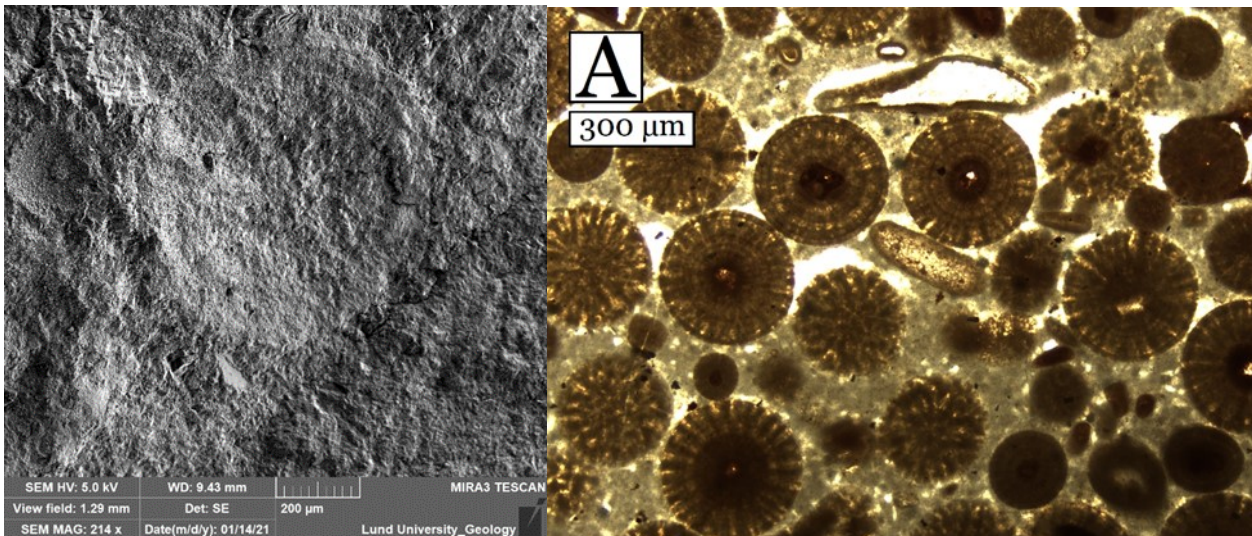


Figure 15: Radial ooid from sample WG 19 in SEM (left) and optical microscope (right)

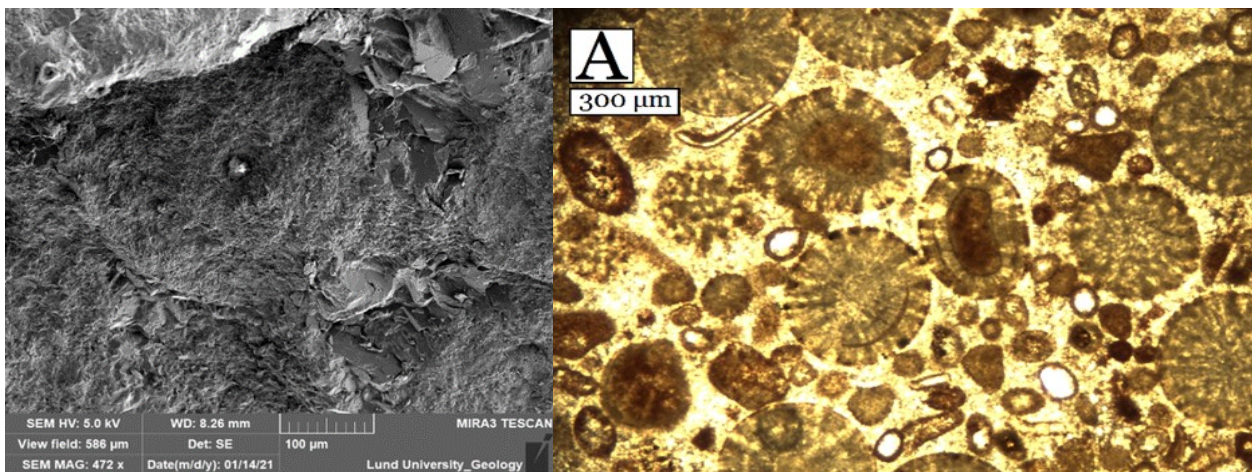


Figure 16: Radial ooid from sample WG 20 in SEM (left) and optical microscope (right).



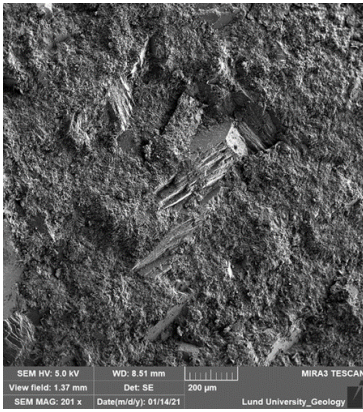


Figure 17: WG8 in SEM, cut off fragment of ooid, cortoids or coated grain.

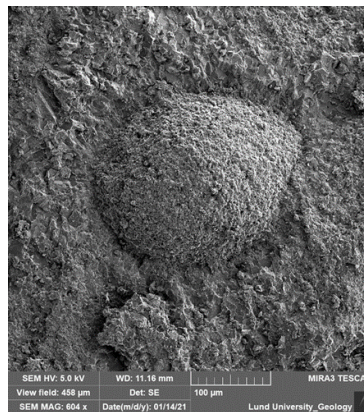


Figure 18: WG11 in SEM, whole ooid.

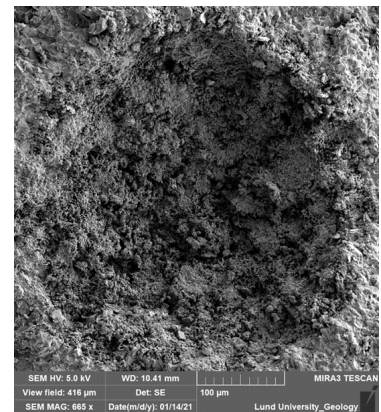


Figure 19: Remnant of ooid in sample WG14

## 5.7 LA-ICP-MS

Geochemical results are presented as graphs from both Wadi Ghalilah and Wadi Milaha. Results from Wadi Milaha were obtained by Ingrid Urban.

### 5.7.1 Average elemental concentrations

The average elemental concentrations plotted in Fig. 20 shows that the four categories follow the same trend overall, with mainly the nuclei and radial laminae of ooids having the highest average elemental concentrations.

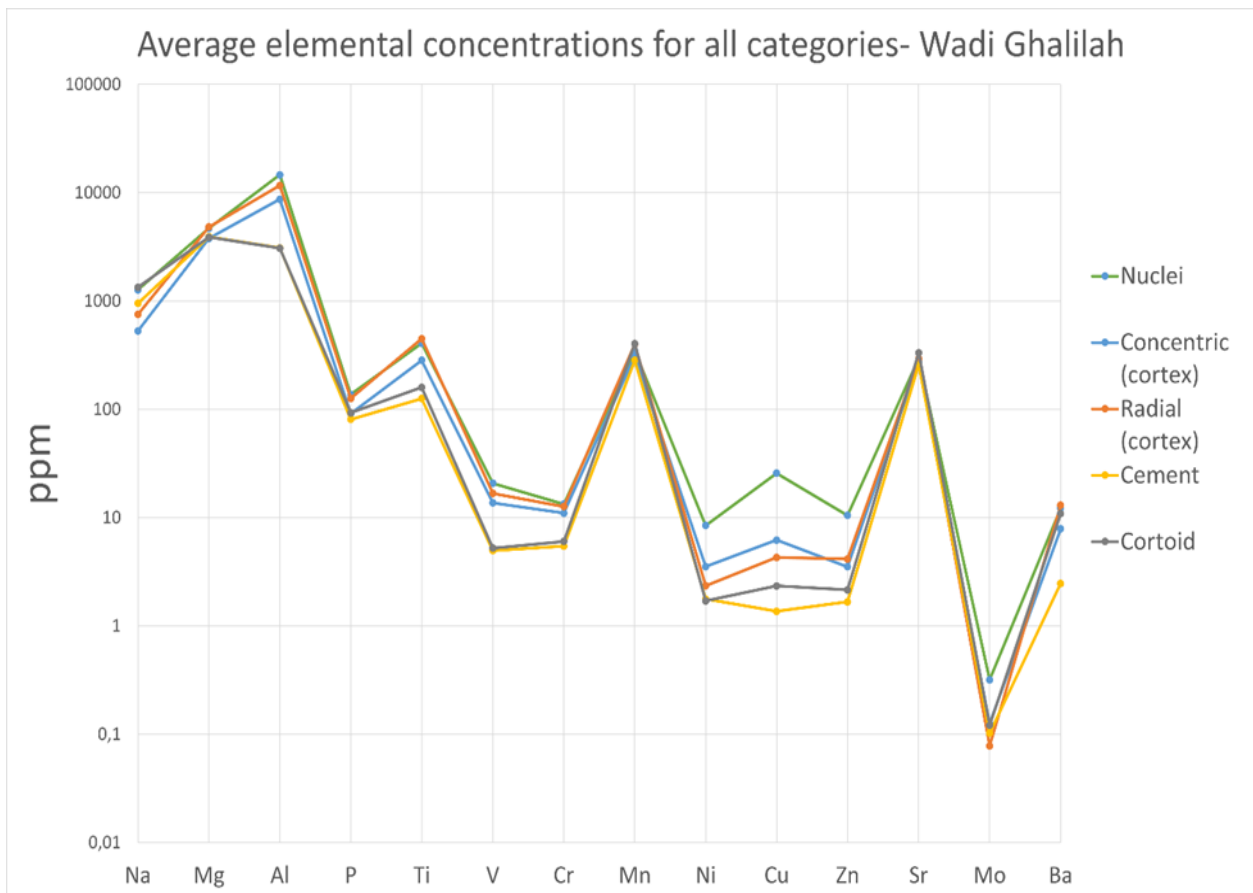


Figure 20: Average major and trace element concentrations summarized for all four categories (nuclei, cortex, cement, cortoids), with the cortex (laminae) category being divided in concentric and radial. The logarithmic scale shows that all categories seemingly follow the same trend despite some difference in the order of magnitude. Elements which frequently replace Ca in  $\text{CaCO}_3$  and bind with  $\text{O}_2$  to form silicates (Such as Mg, Sr, and Al) have the largest concentrations, with certain trace elements included exponentially less.

### 5.7.2 REE + Y concentrations

REE + Y results are here presented in two graphs, one for Wadi Ghalilah (Fig. 21) and one for Wadi Milaha (Fig. 22). Results from both graphs have been normalized according to PAAS, and they seemingly

follow the same trend. As Wadi Ghalilah ooids were all distinguished as non-micritized, these should be correlated for the most accurate comparisons. From the REEs, it is mainly Ce, Pr, and Nd which will be taken into account in order to draw further conclusions about the redox conditions at the time of deposition.

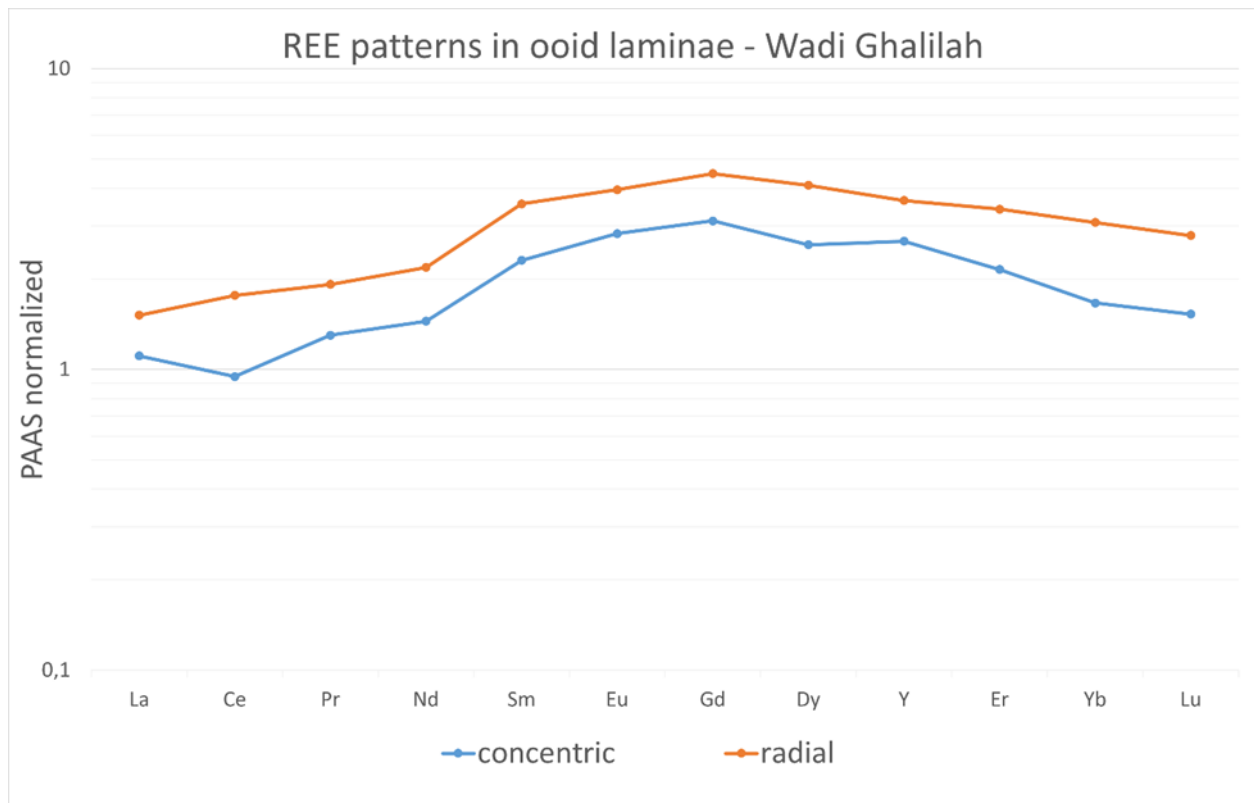


Figure 21: Average REE + Y concentrations from Wadi Ghalilah ooid laminae. Average concentrations in ppm have been normalized according to PAAS (McLennan 1993). This will allow for certain proxies to be applied regarding redox conditions, and in particular it is the Ce, Pr, and Nd values from this graph which will be used for this purpose.

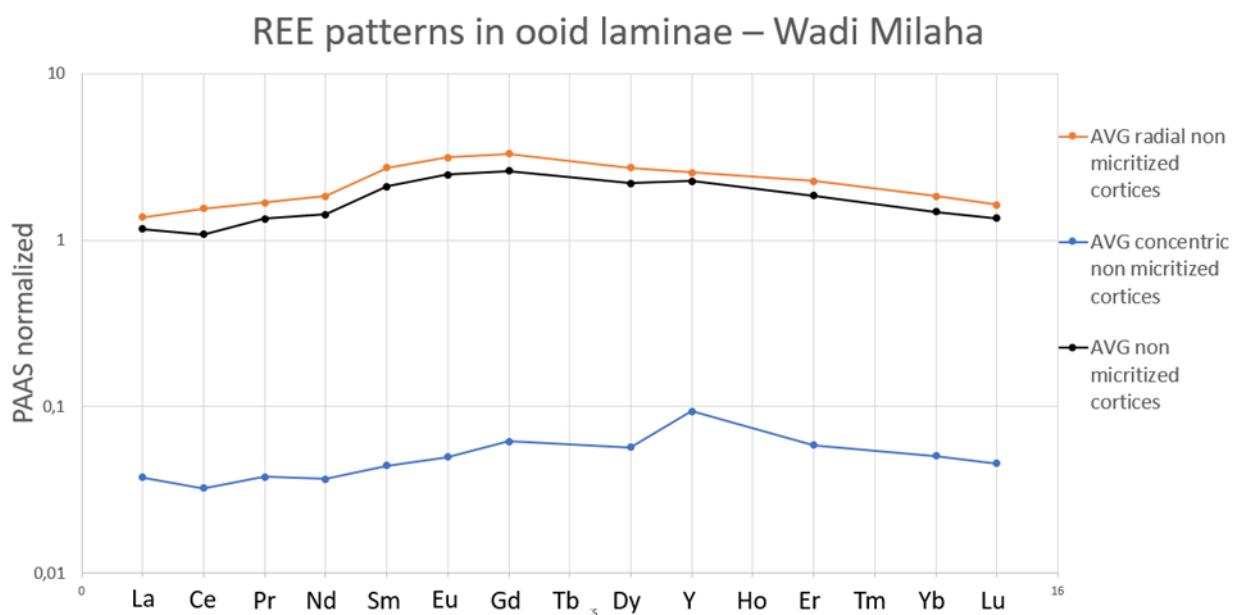


Figure 22: REE+ Y concentrations from Wadi Milaha ooid laminae., also normalized to PAAS. AVG = average.

### 5.7.3 Ooid laminae major and minor elemental concentrations

When it comes to major and minor elements analyzed in the laminae of ooids, there are in general higher concentrations of most elements in Wadi Ghalilah samples than Wadi Milaha, and radial ooids have on average higher concentrations than concentric (apart from Ni, Cu, and Mo) (Fig. 23). Both localities also have similarly low-Mg calcite (Figs. 24 & 25). In Wadi Ghalilah, the radial ooids become slightly more Mg-rich than the concentric ones, although still falling under the category of low-Mg calcite (less than 4% mol).

Examples of elements which follow the overall trend of higher concentrations in Wadi Ghalilah as well as higher concentrations in radial compared to concentric ooids are: Mn (Figs. 26 & 27) and Ti (Figs. 28 & 29). Zn (Figs. 30 & 31) and Sr (Fig 32 & 33), however breaks this trend and Wadi Milaha have slightly higher Sr concentrations than Wadi Ghalilah, although radial ooids still have the highest concentration in both localities. All average values and concentrations for both Wadi Ghalilah and Wadi Milaha are summarized in table 1. However considering the error margins Zn and Sr are more or less within the same value range at both localities.

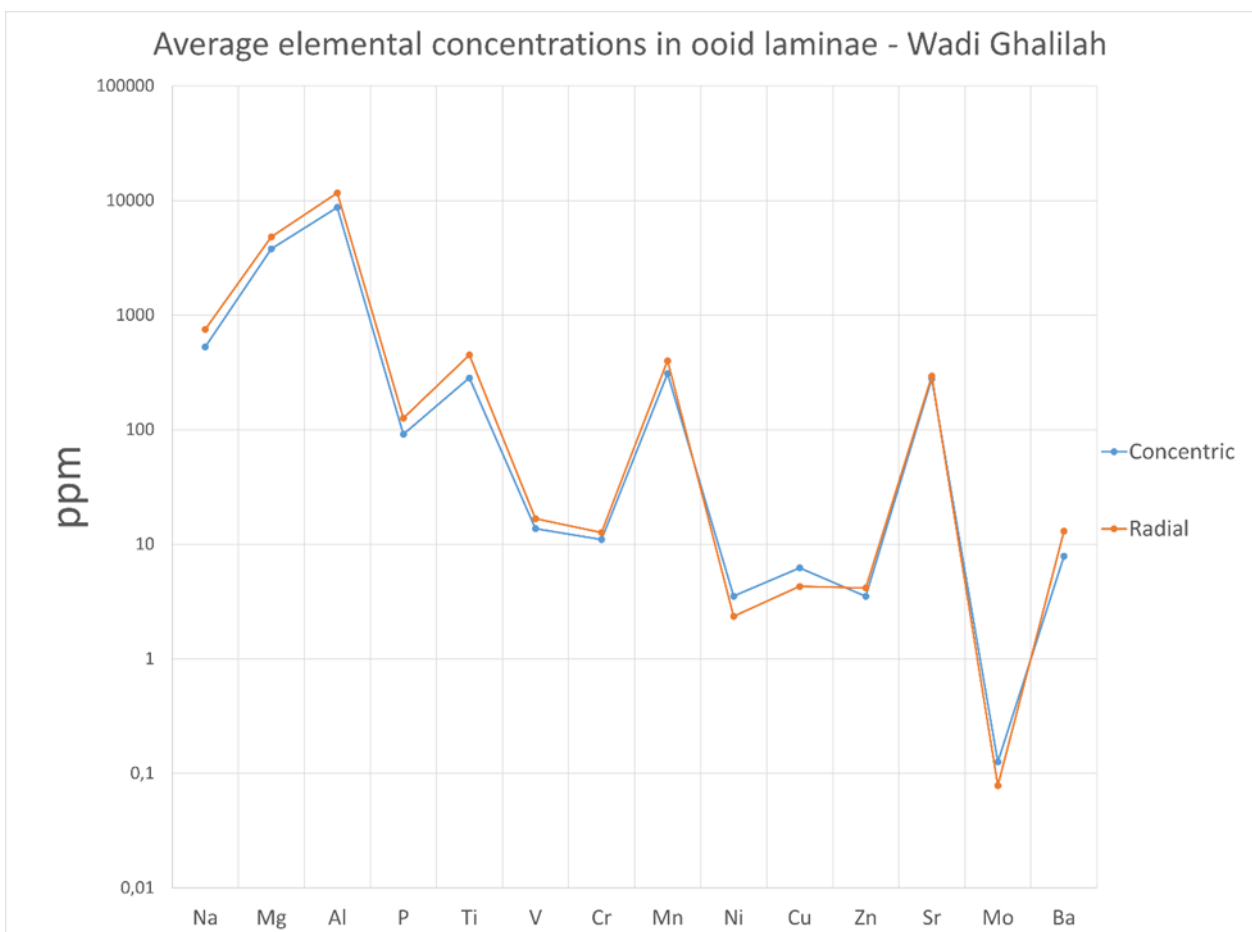


Figure 23: Simplified graph from Figure 20 displaying average elemental concentrations only in ooid laminae plotted in ppm. The orange line representing radial ooids follows the same trend as concentric ooid concentrations but higher, except for Ni, Cu, and Mo.

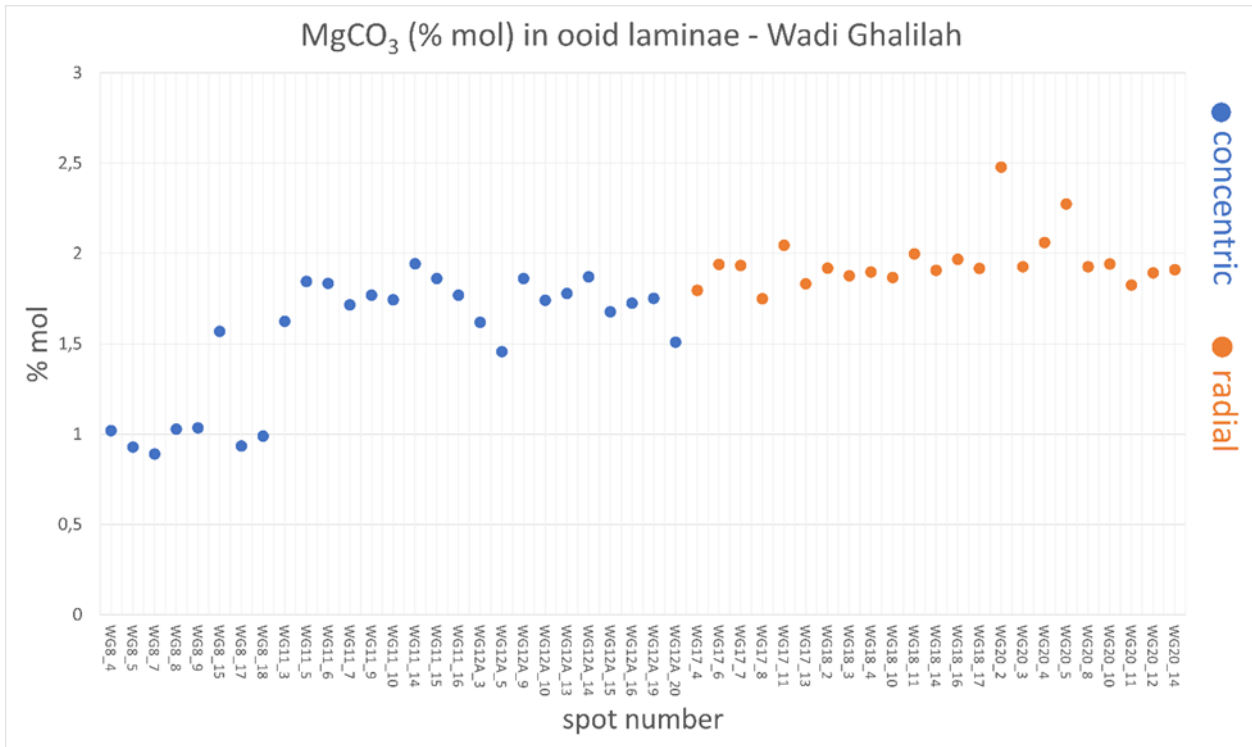


Figure 24: MgCO<sub>3</sub> in ooid laminae from Wadi Ghalilah. Generally, more than 4% mol is considered high-Mg calcite, below this as low-Mg calcite. Average values: Concentric = 1,54%, Radial = 1,95%.

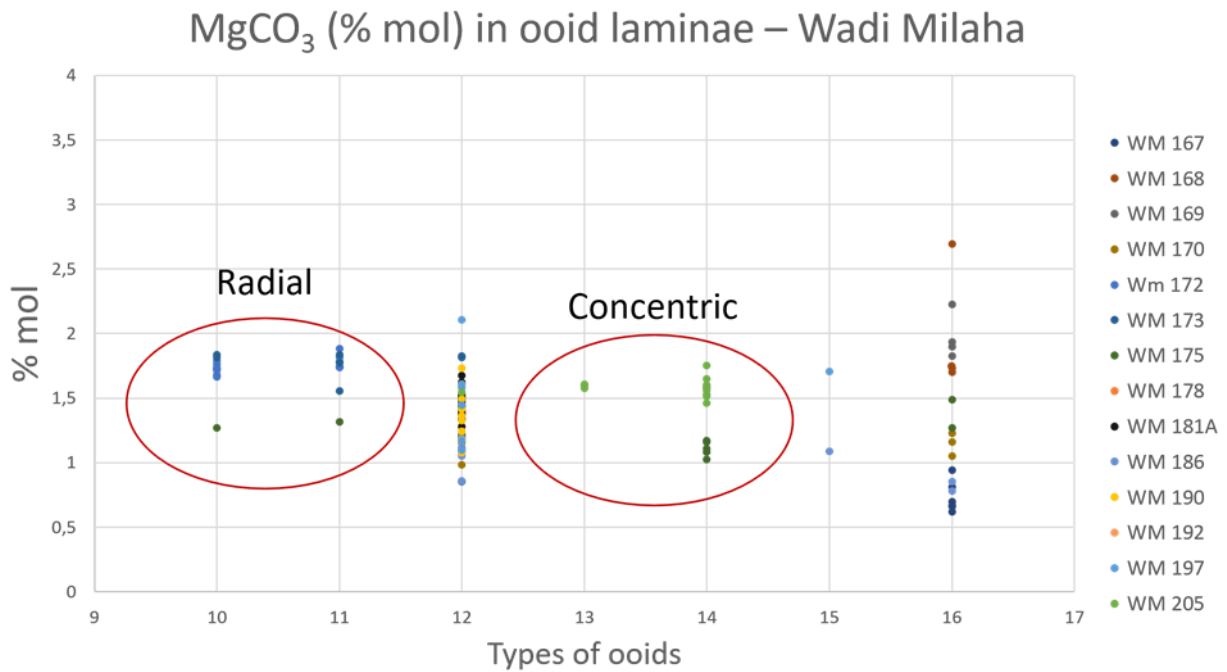


Figure 25: MgCO<sub>3</sub> (%) in ooid laminae from Wadi Milaha. 10 & 11 = Radial laminae, 13 & 14 = Concentric laminae, 12 = Micritized laminae, 15 = Recrystallized laminae, 16 = Laminae from superficially coated grains. Average values: Concentric = 1,46 %, Radial = 1,7 %.

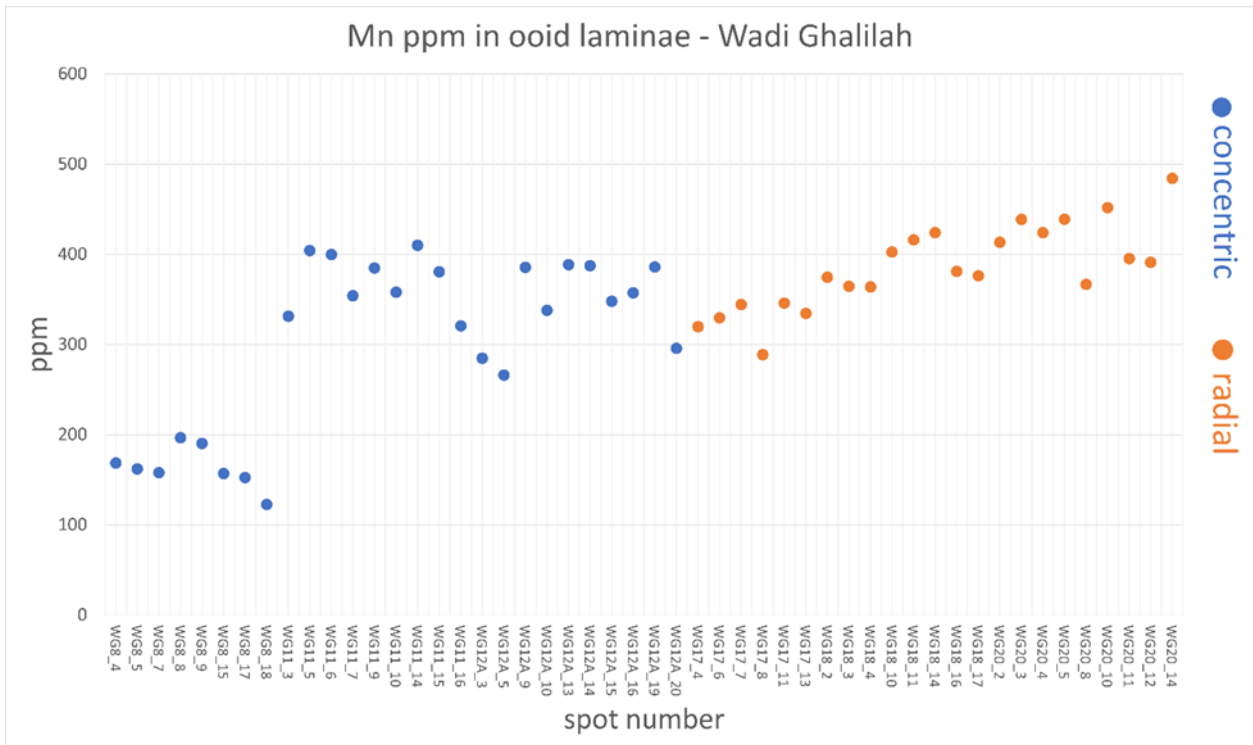


Figure 26: Figure 30: Mn ppm in ooid laminae from Wadi Ghalilah. Average values: Concentric = 299 ( $\pm 28,7$ ) ppm, Radial = 385 ( $\pm 37,9$ ) ppm. See Appendix 3 for more details and images on spot number references

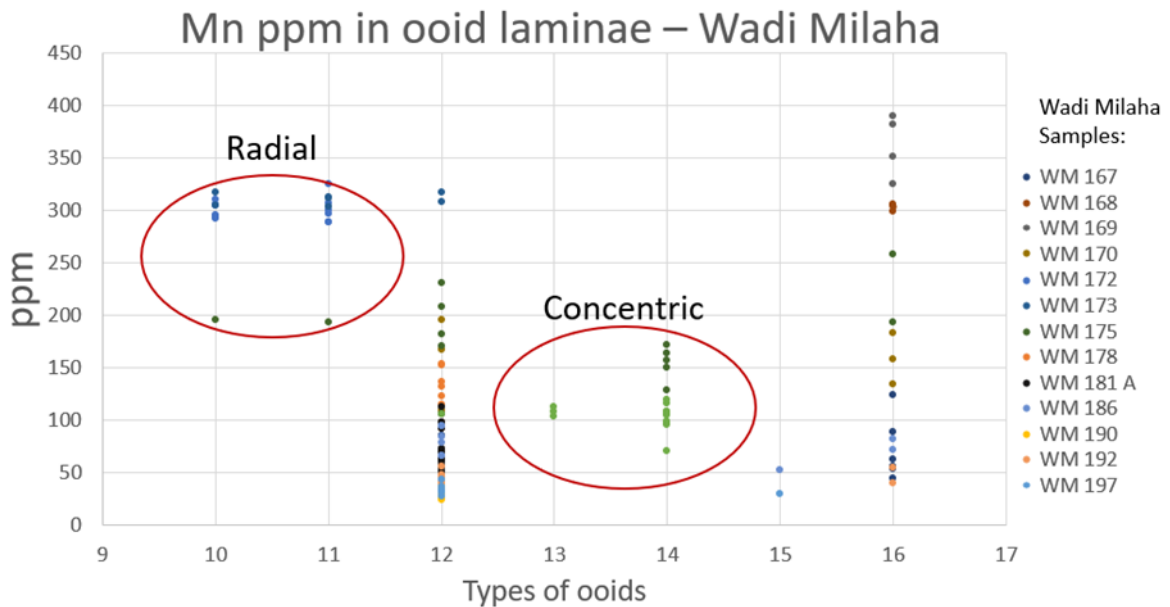


Figure 27: Mn ppm in ooid laminae from Wadi Milaha. 10 & 11 = Radial laminae, 13 & 14 = Concentric laminae, 12 = Miticritized laminae, 15 = Recrystallized laminae, 16 = Laminae from superficially coated grains. Average values: Concentric = 120 ppm, Radial = 270 ppm.

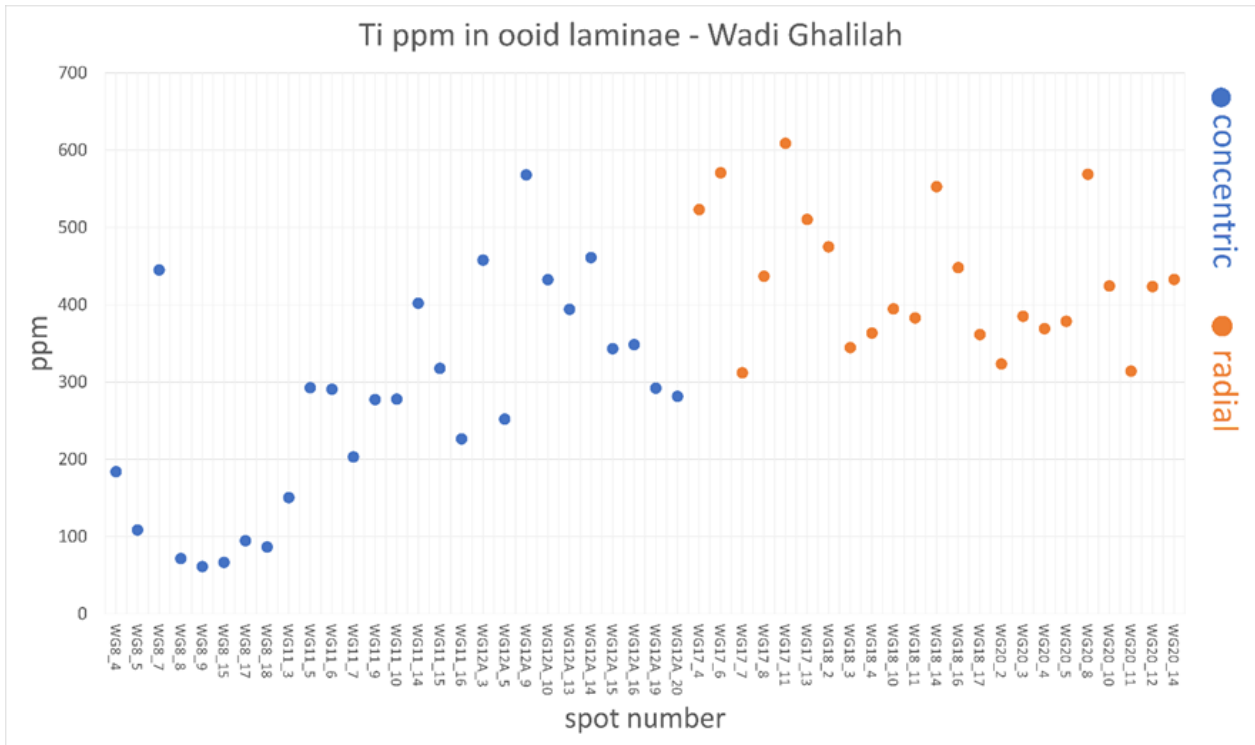


Figure 28: Ti ppm in ooid laminae from Wadi Ghalilah. Average values: Concentric = 273 ( $\pm 13,5$ ) ppm, Radial = 430 ( $\pm 17,2$ ) ppm. See Appendix 3 for more details and images on spot number references.

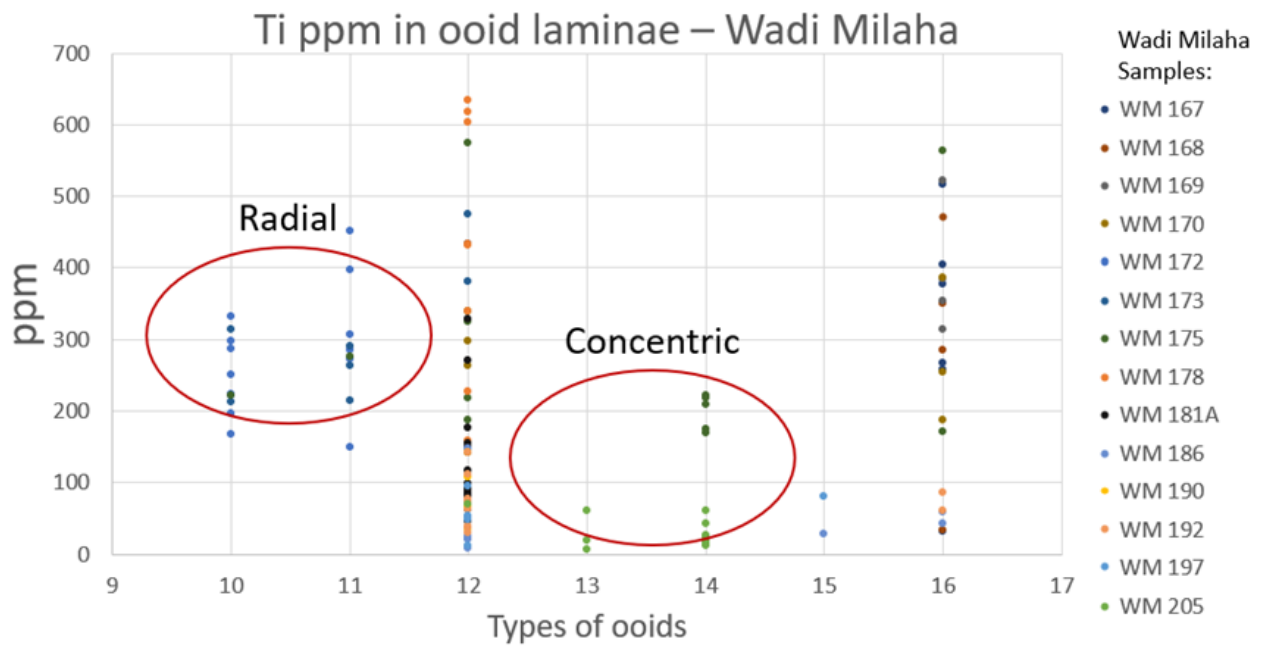


Figure 29: Ti ppm in ooid laminae from Wadi Milaha. 10 & 11 = Radial laminae, 13 & 14 = Concentric laminae, 12 = Mi-criticized laminae, 15 = Recrystallized laminae, 16 = Laminae from superficially coated grains. Average values: Concentric = 87 ppm, Radial = 280 ppm.

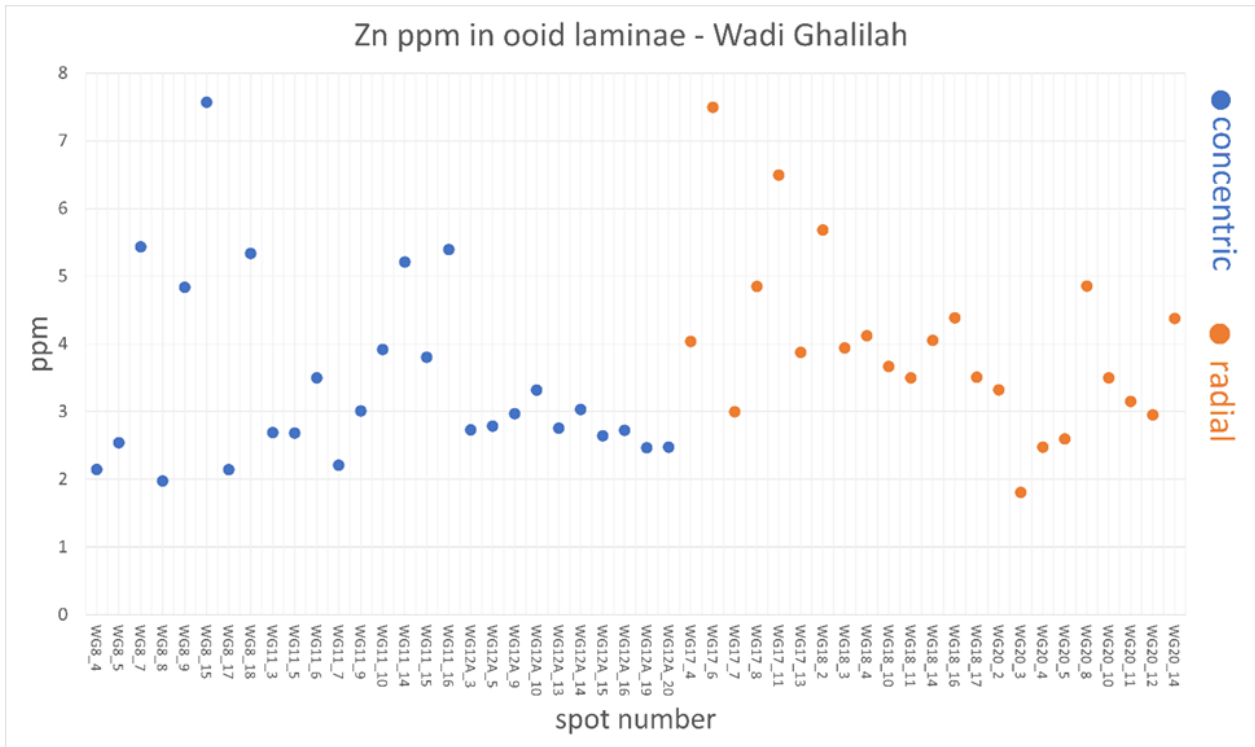


Figure 30: Zn ppm in ooid laminae from Wadi Ghalilah. Average values: Concentric = 3,42 ( $\pm 0,8$ ) ppm, Radial = 3,98 ( $\pm 1,0$ ) ppm. See Appendix 3 for more details and images on spot number references.

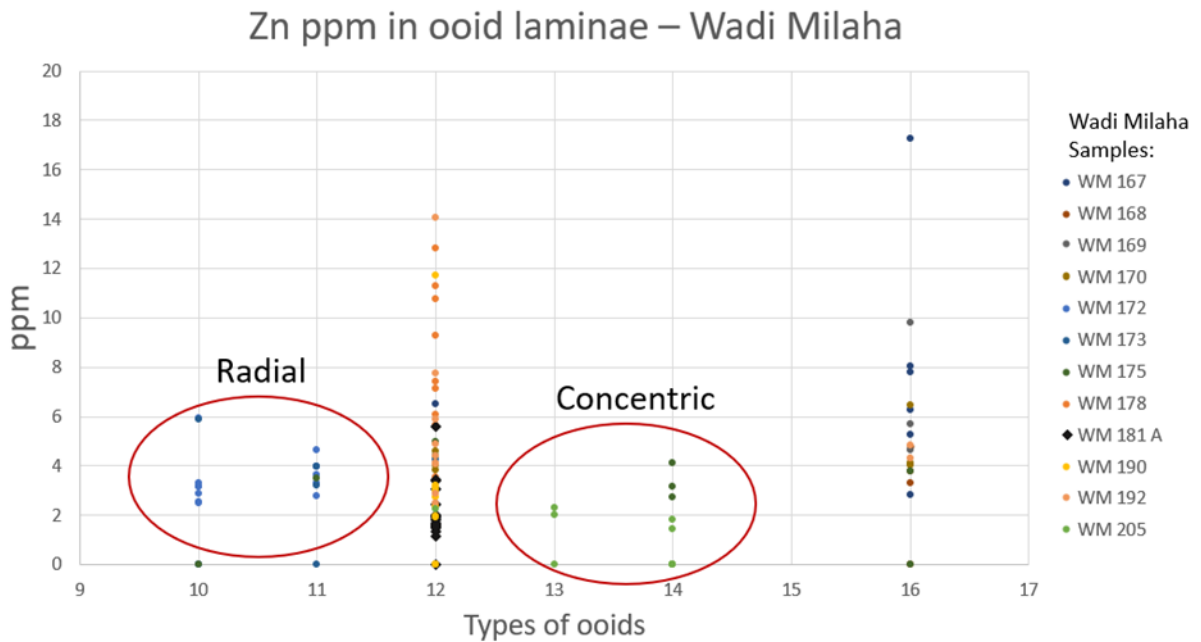


Figure 31: Zn ppm in ooid laminae from Wadi Milaha. 10 & 11 = Radial laminae, 13 & 14 = Concentric laminae, 12 = Mi-criticized laminae, 15 = Recrystallized laminae, 16 = Laminae from superficially coated grains. Average values: Concentric = 2,6 ppm, Radial = 3,5 ppm



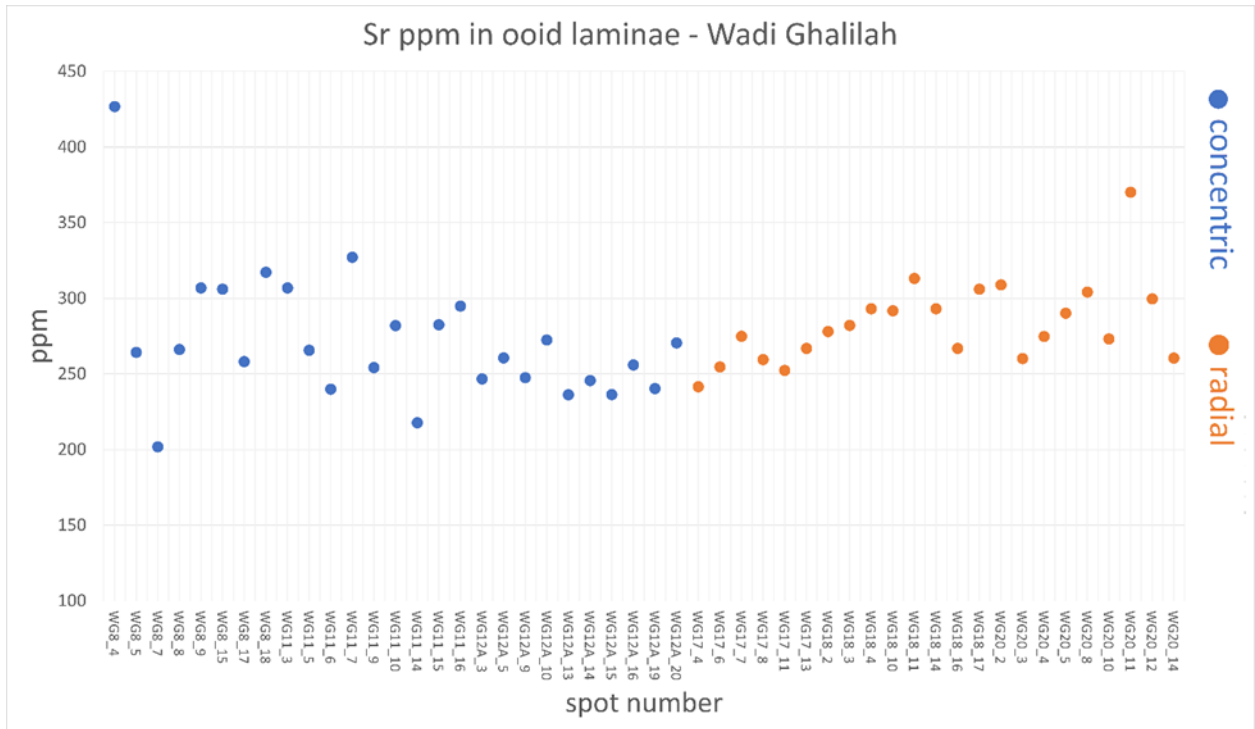


Figure 32: Sr content in Wadi Ghalilah ooid laminae. Around 8000 ppm is a typical Sr concentration for aragonite. Average values: Concentric = 271 ( $\pm 10,8$ ) ppm, Radial = 283 ( $\pm 12,2$ ) ppm.

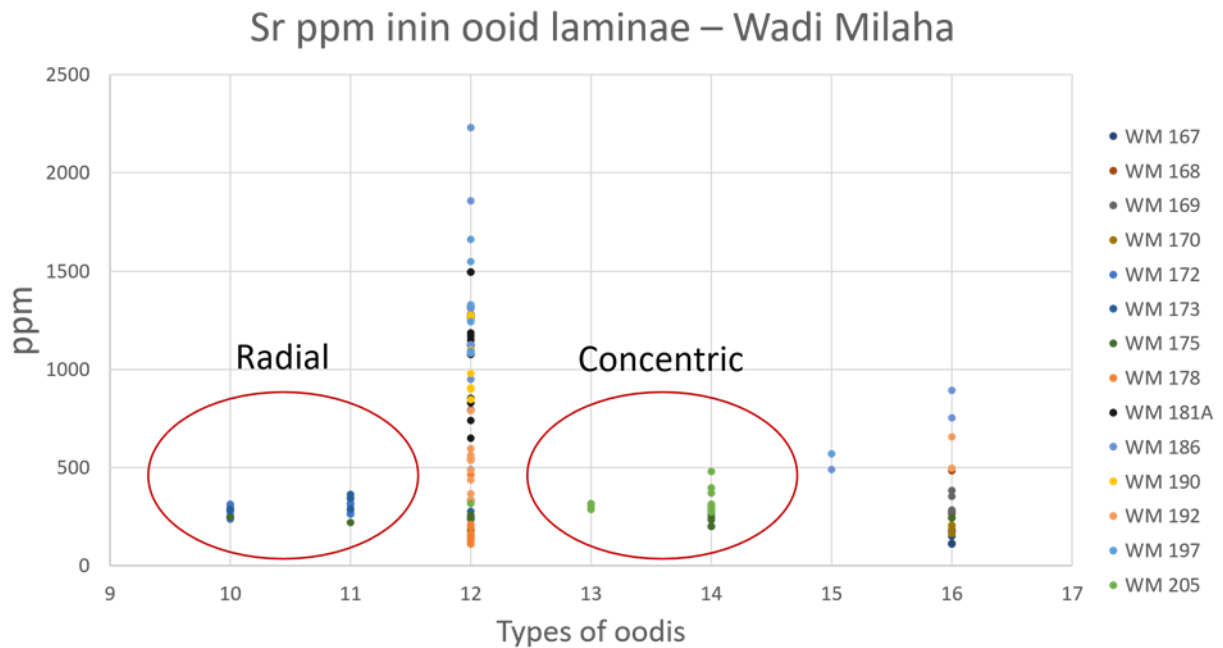


Figure 33: Sr ppm in ooid laminae from Wadi Milaha. 10 & 11 = Radial laminae, 13 & 14 = Concentric laminae, 12 = Mi-critized laminae, 15 = Recrystallized laminae, 16 = Laminae from superficially coated grains. Average values: Concentric = 285 ppm, Radial = 295 ppm



Table 1: Summary of the previous graphs. WM = Wadi Milaha, WG = Wadi Ghalilah

Ooid type and locality	MgCO <sub>3</sub> (%)	Mn (ppm)	Ti (ppm)	Zn (ppm)	Sr (ppm)
Concentric (WM)	1,46%	120	87	2,6	285
Concentric (WG)	1,54%	299	273	3,42	271
Radial (WM)	1,70%	270	280	3,5	295
Radial (WG)	1,95%	385	430	3,98	283

## 5.8 Transects

As previously stated, radial ooid laminae and their nuclei tend to be composed of higher concentrations of almost all the examined elements. Some differences between the two ooid types are however more noticeable and drastic than others, which allows for some conclusions to be drawn regarding their respective formational environments. Six transects, three of concentric ooids and three of radial ooids, have been made for each of the elements Al, Ti, U, Ba, Mn, P, Zn, and Sr. Here, example comparisons of concentric and radial ooid transects will be shown as well as general trend from concentric to radial ooids. For full references of all six transects of every element, see Appendix 2.

Transects have shown that Al (Fig. 34) and Ti (Fig. 35) are barely present in concentric ooid nuclei but is later absorbed in the laminae, whereas in radial ooids these elements are also present in the nucleus to a significantly larger extent. It appears therefore that the concentric ooids do not have a siliciclastic nucleus, whereas radial ones do. This trend is also followed by U and Ba (Fig. 36 & 37), and slightly for Mn (Fig. 38, and P (Fig. 39). It is however not as prominent for Sr (Fig. 40) and Zn (Fig. 41) (except for Zn in WG18, which has around 10 times higher concentrations than the other two radial samples). The concentrations of most of these elements in different parts of the laminae seem to be relatively constant except for Sr and Zn, which really fluctuates the most.

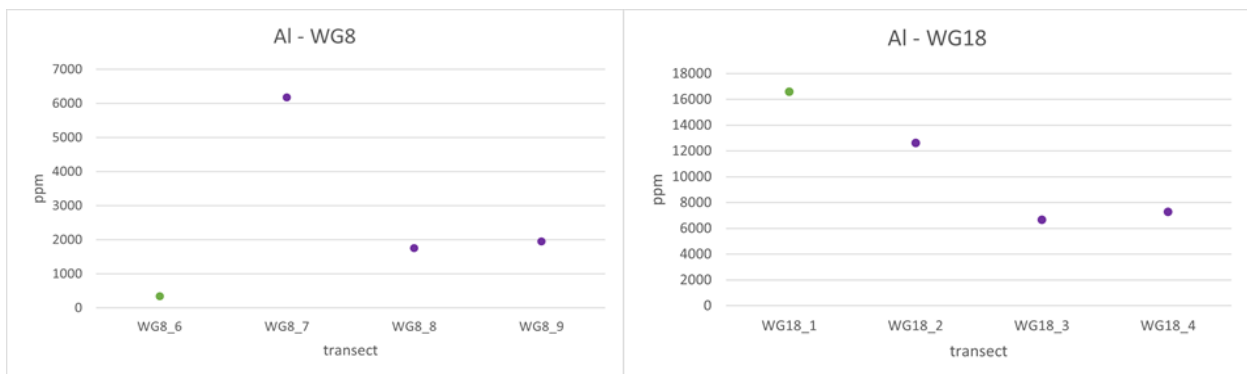


Figure 34: Al concentrations in concentric ooid (left), and radial ooid (right). Green dot = nucleus. Purple dots = laminae. Data points further to the right in the diagram represents spots further away from the nucleus. See Appendix for reference of spots and further Al transects.

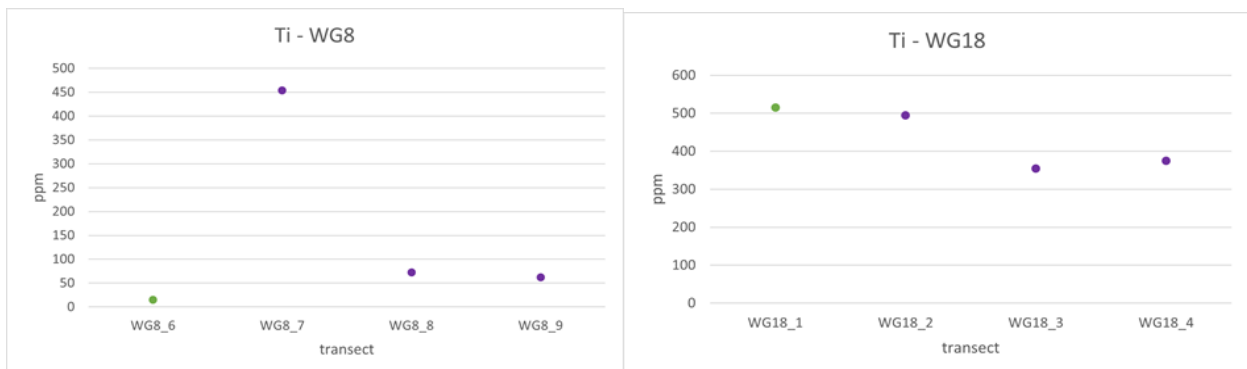


Figure 35: Ti concentrations in concentric ooid (left), and radial ooid (right). Green dot = nucleus. Purple dots = laminae. Data points further to the right in the diagram represents spots further away from the nucleus. See Appendix for reference of spots and further Ti transects.

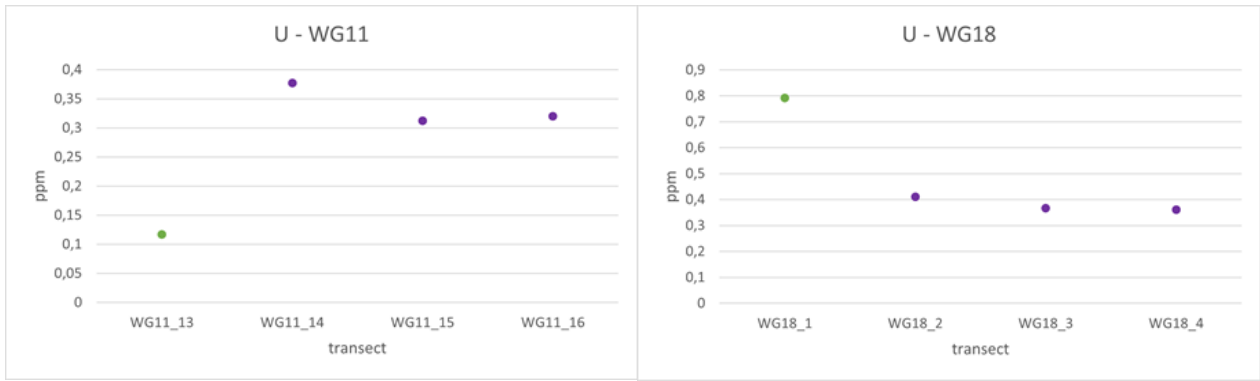


Figure 36: U concentrations in concentric ooid (left), and radial ooid (right). Green dot = nucleus. Purple dots = laminae. Data points further to the right in the diagram represents spots further away from the nucleus. See Appendix for reference of spots and further U transects.



Figure 37: Ba concentrations in concentric ooid (left), and radial ooid (right). Green dot = nucleus. Purple dots = laminae. Data points further to the right in the diagram represents spots further away from the nucleus. See Appendix for reference of spots and further Ba transects.

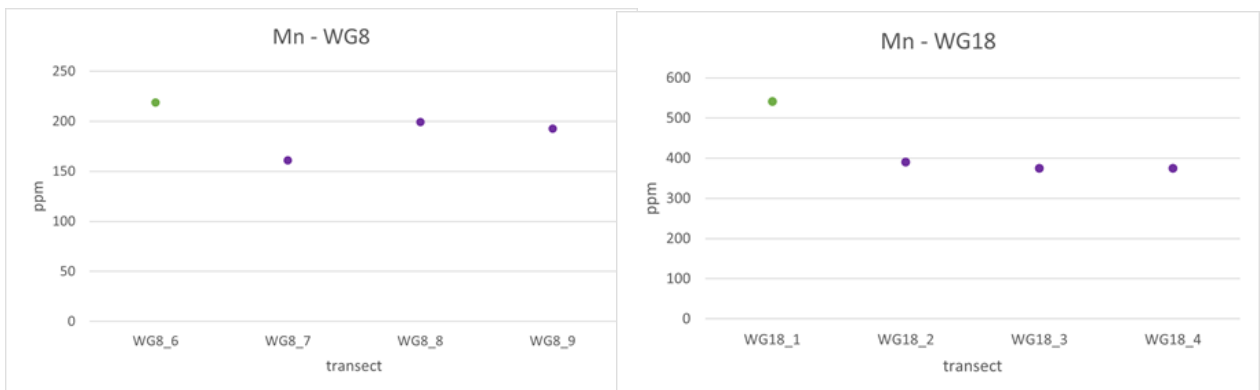


Figure 38: Mn concentrations in concentric ooid (left), and radial ooid (right). Green dot = nucleus. Purple dots = laminae. Data points further to the right in the diagram represents spots further away from the nucleus. See Appendix for reference of spots and further Mn transects.

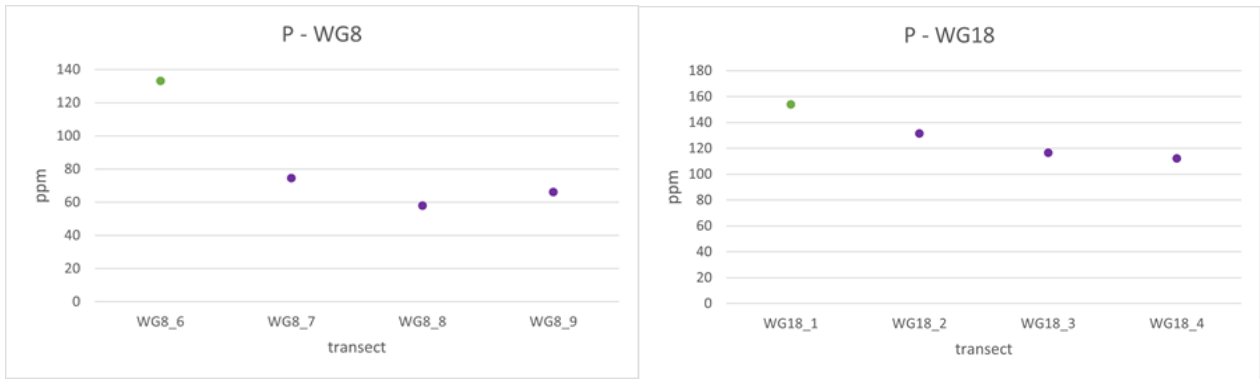


Figure 39: P concentrations in concentric ooid (left), and radial ooid (right). Green dot = nucleus. Purple dots = laminae. Data points further to the right in the diagram represents spots further away from the nucleus . See Appendix for reference of spots and further P transects.

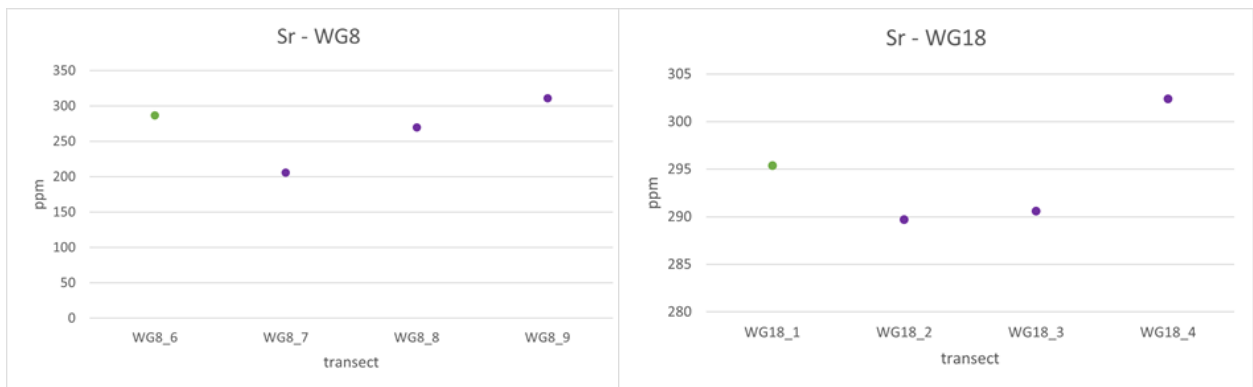


Figure 40: Sr concentrations in concentric ooid (left), and radial ooid (right). Green dot = nucleus. Purple dots = laminae. Data points further to the right in the diagram represents spots further away from the nucleus. See Appendix for reference of spots and further Sr transects.

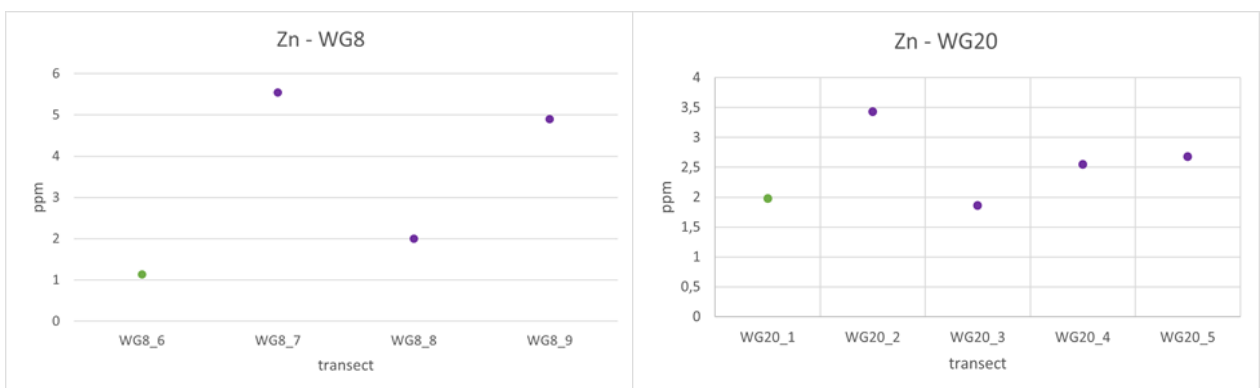


Figure 41: Zn concentrations in concentric ooid (left), and radial ooid (right). Green dot = nucleus. Purple dots = laminae. Data points further to the right in the diagram represents spots further away from the nucleus. See Appendix for reference of spots and further Zn transects.

## 5.9 Ce anomaly and redox conditions

As mentioned in chapter 4.7, due to the oxidization of  $Ce^{3+}$  to  $Ce^{4+}$  in oxic settings, a negative or positive Ce anomaly compared to the REE normalized with PAAS constitutes a proxy for oxygen levels and redox conditions in marine settings (German & Elderfield 1990; Shields & Stille 2001). In the case of Wadi Ghalilah, concentric ooids on average have a negative Ce anomaly, and radial ooids have a positive one (Fig. 25). This would imply that there is an increase in anoxia between the lower concentric samples and the radial ones. This can further be investigated by using the REE values normalized with PAAS and applying the formula:

$$\frac{Pr_{PAAS}}{0,5Ce_{PAAS} + 0,5Nd_{PAAS}}$$

As suggested by Bau & Dulski (1996), ratios of  $> 1$  using this formula are indicative of oxygenated environments, and ratios of  $< 1$  imply an increasingly dysoxic environment. For the average of concentric ooids, this ratio equals 1,07, and for radial ooids this ratio is = 0,97. This implies, just like the initial PAAS normalization, an increasingly dysoxic to anoxic environment as we go further into the Hettangian.

## 6 Discussion

### 6.1 Petrographic analyses

As shown in the results and summary of the petrographic descriptions, the main lithology of the Sakhra Member is constituted of oolitic grainstone with thrombolites, herein interpreted as anachronistic facies deposited in connection to the ETME. Although not visible at the Wadi Ghalilah locality, a sub-marine dissolution surface believed to be the cause of ocean acidification is visible between the Sumra and Sakhra Members at Wadi Milaha, marking the end of the extinction interval. This erosion surface also aids in correlation with other globally recognized T -J marine sections and their respective depositional hiati (Pálffy et al. 2021).

The ooids in the Sakhra Member generally transition from concentric to radial further up in the section, with varying degrees of micritization visible in the samples. The three proposed micritization intervals (MI 1, MI 2, and MI 3), might be due to the effects of Milankovitch cyclicality, as the change in water level (and thereby water energy) could affect to what extent microbes can break down the ooid laminae in the sediment. At higher water energy environments, there

would be less micritization. If the micritization intervals are not caused by Milankovitch cyclicality, it is still highly plausible that Milankovitch cyclicality on the scale of 100 kyrs has had an effect on the deposition of the Sakhra Member. This is because the Ghalilah Formation was deposited in a quiet part of the Tethys ocean where the effects of tectonic activity would have been limited or non-existing for a long time.

The only part of these three intervals which can be correlated to geochemical analyses are transects of U and Ba from WG8 to WG20 in MI1. U seems to follow the trend displayed in the micritization intervals (Fig. 16), with relatively higher values in WG8 indicating more micritization, decreasing slightly to WG11 and WG 12A, before reaching its highest measured concentrations in the radial ooids of WG17, WG18, and WG20. For Ba, the concentrations increase from WG8 to WG11 and WG12A, which somewhat contradicts the U observations. It would therefore be interesting to see how for example U and Ba vary further up in the section. This could result in more accurate interpretations of the micritization intervals which was present at the time of deposition, apart from just visual observations.

### 6.2 SEM interpretations

SEM observations mainly served as reference material for the optical microscope. At times, SEM and optical microscope observations seemed to counteract one another, however the optical microscope was favored in these cases. This is due to the nature of the crystal orientation in the ooids, which could not have been induced by microborers. More severe microbial interaction would have resulted in a more sporadic destruction of the laminae rather than the oriented structures which are observable in the optical microscope. Although some ooids could be designated as micritic, it does not change the overall assignment of SMF.

### 6.3 Sequence stratigraphy

As mentioned in chapter 5.6, between meters 7-14 when referring to the log the Sakhra Member has been interpreted to initially be in an ETST, where accommodation space (AS) is gradually starting to increase. This is based on the deposition of the cross laminated oolitic grainstones which constitutes the main lithology in this part of the formation. This is before transitioning into a LTST with laminated lime-mudstone between meters 14 and 19 where AS is increasing faster than carbonate production can keep up, resulting in deeper marine settings than the ETST. Above this, there is a sharp boundary between the mudstone and a small-scale breccia, indicating that a regression has taken place and that we are missing the maximum flooding interval and subsequent High Stand Systems

Tract (HSST) in this area. Moreover, it is plausible that the breccia is karstic in nature, as another nearby locality by the name of Wadi Naqab (also displaying the Ghalilah Formation about 30 km SSE from Wadi Ghalilah), has a clear karst surface with a breccia at the same level. This breccia interval is then characterized as a Falling Stage Systems Tract (FSST) assuming that brief subaerial exposure has occurred. The final meters of the section are characterized as the start of another TST which continues into the overlying Shuba Member. These observations have been made considering the under and overlying Members in Wadi Ghalilah as well as Wadi Milaha, in order to get a sense of the larger scale systems at play. These sequence stratigraphy results are also coincident with more globally observed Hettangian transgressions (Pálffy et al. 2021).

#### 6.4 Milankovitch cyclicity

Given the nature of large parts of the Sakhra Member, it is highly plausible that it is influenced by Milankovitch cyclicity. Since the Hettangian is a very short stage of about 2 Myrs, large scale tectonic movements resulting in significant sea level changes are unlikely to have caused the high resolution changes displayed at Wadi Ghalilah. To be able to draw certain conclusions about the effect of Milankovitch cyclicity on the studied sections there would have been need for other methods, such as magnetic susceptibility and time-series analyses. It seems most probable however that the 100 kyrs eccentricity cycle is dominant, with obliquity and precession being less visible in large parts of the sections.

#### 6.5 Previous analyses of the Ghalilah Formation

Al-Suwaidi et al. (2016), Höning (2017), and Ge et al. (2019), are some of the authors who have examined the Ghalilah Formation in recent years, and to which I have looked for comparisons and theories which could be essential to understand its depositional history. However, there are several conflicting observations which would benefit from further work. For example, Ge et al. (2019) recognizes 3 coarsening upward cycles in the Sakhra Member which these authors connect to Milankovitch cycles about 30-40 kyrs apart. The warm climate which resulted from the CAMP volcanism would have also been a reinforcing mechanism for the effects of the cycles (Ge et al. 2019). Moreover, these coarsening upwards cycles also contain three ooid cycles named C1, C2, and C3 (Fig 42.). From C1 to C3, Ge et al. (2019) show a transition from mainly calcitic to aragonitic ooids, more micritization, and all cycles are constituted of mudstone in the lower part and packstone/grainstone in the top. These three

ooid cycles were not recognized in this study partly due to differences in the examined outcrop (the two examined localities, while both in Wadi Ghalilah, are some distance from each other), and the fact that geochemical analyses were only made on the lower part of the Sakhra Member in this study. Moreover, in this study point to point analyses (spot analysis) were made instead of bulk rock analysis, and we could provide more accurate results on individual categories such as ooid laminae.

According to Ge et al. (2019) there is a possible recovery period after the ETME where the ooids are more Mg-rich. This could be possible for more deeper marine settings, however in the Sakhra Member the cement types are mainly blocky cements which are typical for low Mg-calcite settings. Since the LA-ICP-MS analyses of the early Hettangian ooids in this study all implied low-Mg calcite, there is also a contradiction in these results. However, ooids further up in the

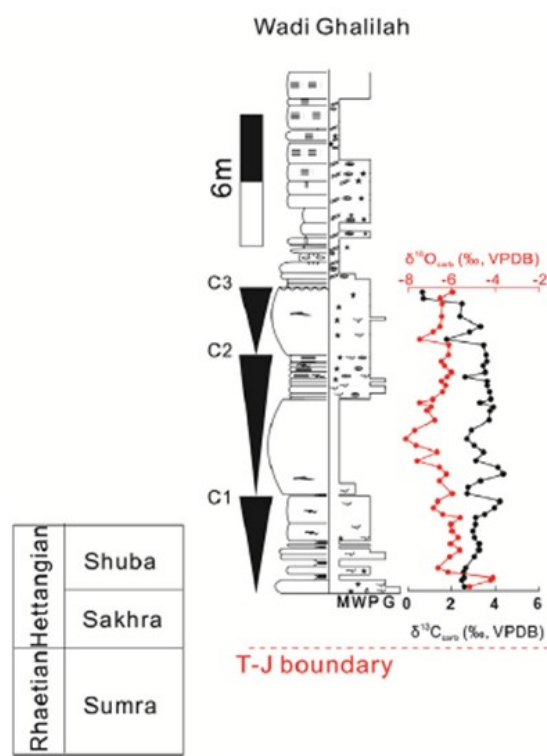


Figure 42: The three proposed ooid cycles in Wadi Ghalilah by Ge et al. (2019).

section should be analyzed in order to fully understand this trend, as the observations from this study could be limited to samples in the lower part of the section. However, Ingrid Urban's analyses of Wadi Milaha ooids further up in the section does not imply a change in this regard, but are still composed of low-Mg calcite similarly to the ones from the lower Sakhra Member.

Results are more difficult to compare with those from Hönig et al. (2017), as there are conflicting opinions on the precise placement of the T-J boundary. This is of course a major bottleneck for accurate correlations to be drawn concerning post extinction conditions. The proposed models of sea level evolution used by Hönig et al. (2017) does however seem to correlate regardless of where the T- J boundary is placed, and the globally recognized transgressions with a deepening towards the Shuba Member is quite similar. It is then instead the cause of the initial transgressions and whether ocean acidification occurred which seems to be the major points of contrast.

## 6.6 LA-ICP-MS interpretations

### 6.6.1 Average ooid elemental concentrations

Similarly to Wadi Milaha, radial ooids have higher concentrations in almost all analyzed elements compared to concentric ones except for Ni, Cu, and Mo where concentric ooids have higher values. Moreover, there is a higher recorded concentration of all elements compared to Wadi Milaha. The higher Zn concentrations in Wadi Ghalilah may imply lower water energy conditions than Wadi Milaha, and the higher Mn content could constitute more anoxic and dysoxic conditions (Tribovillard et al. 2006). Although the error margins of the recorded Zn concentrations make these conclusions more uncertain. As the overall higher Al and Ti concentrations are interpreted as the result from more contamination from silicates, this might be an indication that Wadi Ghalilah was more proximal to continental sources than Wadi Milaha.

In Wadi Ghalilah, the radial ooids become slightly more Mg-rich than the concentric ones, although still falling under the category of low-Mg calcite (less than 4% mol). This is despite a general aragonitic sea at the time (Stanley & Hardie 1999), and as there is similarly low Mg-calcite in Wadi Milaha, this could be a phenomenon more locally limited to these areas at the time of the T-J transition.

It is unclear why Sr seems to be one of the only elements which occurs in slightly greater concentrations in Wadi Milaha than Wadi Ghalilah. However, considering the error margins it is more likely that these concentrations are more or less equal, as Sr should be equally incorporated in the calcite of Wadi Ghalilah and Wadi Milaha ooids regardless of the respective localities distance from terrestrial areas (barring it is not deep enough to be below the CCD, which of course the localities show no indication of).

In regards to the error margins of the majority of the other examined elements, they are not significant enough to draw away from the conclusions that in general, higher elemental concentrations are recorded at Wadi Ghalilah.

### 6.6.2 Transects

As the transects have shown, Al and Ti are barely present in concentric ooid nuclei but is later included in the laminae, and is present in the nuclei of radial ooids to a large extent. If the radial ooids have more siliclastic nuclei, this might indicate an increased degree of continental weathering between the time of deposition between WG12A and WG17.

In the case of U, the slight increase from the concentric to the radial ooids might be attributed to increased microbial activity in the radial samples. This could also be coupled with the aforementioned increase in weathering and temperature in the early Jurassic, as well as the subsequent transport of nutrients to the basin. This increase associated with an increase in P and shift in Ce ratios could as well be attributed to a decrease in oxic conditions. This will also be discussed under the next chapter 6.7.

## 6.7 Redox conditions

### 6.7.1 Ce ratios and calculations

Apart from the method used in this study to investigate redox conditions in marine setting:

$$\frac{Pr}{0,5Ce+0,5Nd}$$

there is an older and more widely used approach which can be applied. This method takes into account the La PAAS normalized concentrations instead of Nd by using the formula:

$$\frac{Ce}{0,5La+0,5Pr}$$

, which when results in ratios <1 indicates oxic conditions, and >1 indicates more dysoxic or anoxic conditions (Bau & Dulski 1996). However, La is not as commonly incorporated in seawater, which results in the downside that this ratio could rather represent relative anomalies of La rather than Ce (Bau & Dulski 1996). Therefore, the first proposed ratio has been preferred in this case.

Still, applying the formula which does take La concentrations into account, concentric ooids have an average value of 0,7896, whereas radial ones receive a value of 1,027, still indicating an increase in dysoxia.



### 6.7.2 Hypotheses of varying P concentrations in ooids

The inclusion of phosphorous and phosphate minerals such as carbonate fluorapatite (CFA) in ooids occurs in early diagenetic stages in marine environments (Li et al. 2011). As shown by the transects, P inclusion varies between the nuclei and laminae of the ooids. Li et al. (2011) propose two hypotheses for the inclusion of P and CFA in ooids on anachronistic carbonate platforms (Fig 43): 1 - deepwater source, and 2 - sediment source. For deep water source, P enrichment is assumed to originate from the decay of organic matter in anoxic deep water environments. This P is then introduced to more shallow water environments through episodes of upwelling. For the sediment source model, dissolved phosphate is released from the decay of organic matter in the sediments and reacts with ferric oxides, before being bound onto the ooid surfaces by microbes. As the P inclusion in ooid nuclei and laminae generally increases from WG8 to WG20 (with the exception of WG12A which has about equal P concentrations as WG20), it can potentially be correlated to the increase of anoxia as evident by the Ce anomaly. Since the Ce anomaly has shown that there is a slight increase in dysoxic conditions after the initial transition into the Hettangian, the increase in P could be

attributed to more dysoxic bottom waters, and when upwelling occurs it would result in higher P concentrations. It could then be plausible that the deep water source model can be applied to the events transpiring at the T-J boundary in Wadi Ghalilah and Wadi Milaha. At WG12A however where there seems to be an anomaly, it is more likely that it is the sediment source model which is more prominent, as it occurs directly below the first layer of thrombolites.

### 6.7.3 Shift in Ce ratios and its implications

Considering the Ce anomalies in concentric and radial ooids compared to PAAS (Fig. 21) the depositional environment at Wadi Ghalilah likely transitioned from oxic to more dysoxic within the first few meters of the formation. This can be coupled with the relative increase in P and U, as more dysoxic and anoxic environments promotes an increase in P. As this P then reaches more shallow waters due to upwelling, it in turn promotes increased microbial activity. This would lead to an increase of U in the laminae of ooids (Newsome et al. 2014).

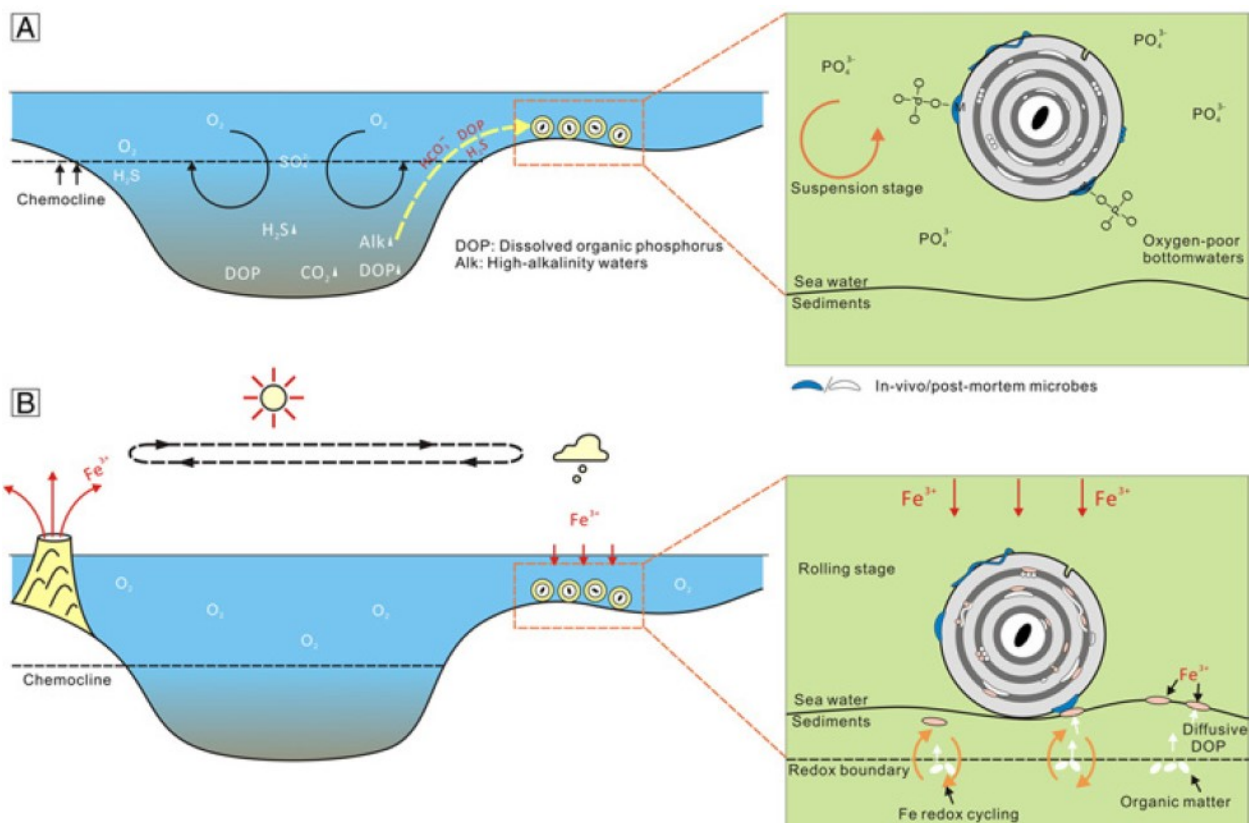


Figure 43: Li et al. (2011)'s two hypotheses for P (CFA) inclusion in ooids from the end-Permian mass extinction recorded in Southern China: A - Deep water source, B - Sediment source.

The initial cause of the dysoxic conditions might be attributed to increased continental weathering, as evident by the increase of silicates in radial ooids compared to concentric. This initial weathering would bring in nutrients to the water which causes an increase in biological productivity and thereby slightly increased bottom water anoxia.

#### 6.7.4 Th/U ratios as redox proxies

In addition to the previously mentioned Ce proxy for measurements of marine redox conditions, U is also a valid proxy of the same conditions which is unrelated to detrital contamination (Tribovillard et al. 2006). Under oxic settings U and Th coexist as soluble ions, but under anoxic conditions the U ions become insoluble and bind to the sediment floor (Wignell & Twitchett 1996). Th ions on the other hand are not affected by anoxia in the same manner as U ions, which results in a relative enrichment of U ions in anoxic environments (Wignell & Twitchett 1996). Higher values of the Th/U ratio would then imply higher oxidized environments. This method is however not as effective when it comes to analysis of limestone and carbonates (Klinkhammer & Palmer 1991), which is why Th has not been analyzed in this study and the Ce anomaly has been preferred as a redox indicator.

### 6.8 Ocean acidification

#### 6.8.1 The “Unreefing” model and global perspectives

Pálffy et al. (2021) analyzed several T-J boundary sections in the Transdanubian Range in Hungary and made comparisons with the Dachstein platform in the Austrian Alps. Comparisons were also made with numerous other T-J boundary sections including results from Wadi Milaha made by Al Suwaidi et al. (2016). The authors describe the demise of the Dachstein coral reef in the Northern Calcareous alps using a new model termed “Unreefing”. By correlating the results from

the examined localities, the authors suggest that the environmental crisis of the ETME resulted in the extinction of reef builders, in turn leading to the transition from a rimmed carbonate shelf into a carbonate ramp system related to the early Hettangian transgression. The transgression was then likely more related to the fact that carbonate production was halted rather than tectonic activity (Pálffy et al. 2021). This made the Dachstein lagoonal area become unprotected and exposed to wave erosion, and ocean acidification halted carbonate production and even led to dissolution in the shallower environments (Pálffy et al. 2021). This phenomenon resembles closely that of what we see in the UAE, where the coral boundstones and floatstones with coral residue of the underlying Sumra Member disappear in a similar manner to the Dachstein coral platforms. Pálffy et al. (2021) however claim that the vulnerability of the Dachstein could be related to its geographic origins, which is in more northern latitudes than the UAE at that time.

Pálffy et al. (2021) base their claim on the fact that many other carbonate platforms survived the crisis, and include the Ghalilah formation as an example (Fig. 44). The authors stress the importance of further studies investigating the latitudinal threshold of the “unreefing” model, and state that “Validity of the model could be verified by finding examples of other reef crises and coincident platform terminations in the global stratigraphic record”. Considering the results from this study, it seems plausible that the unreefing model can also be applied to the Ghalilah formation on the Arabian platform. This is in the sense that the earliest Hettangian transgressions were coupled with the demise of corals, calcareous sponges, and many other carbonate producing organisms. The demise of the reef-builders were, similarly to the Dachstein, likely caused by ocean acidification as the sub-marine erosion surfaces in Wadi Milaha, anachronistic oolites and thrombolite facies would suggest. All of these parallels speak for the fact that this model is applicable to these localities as well.

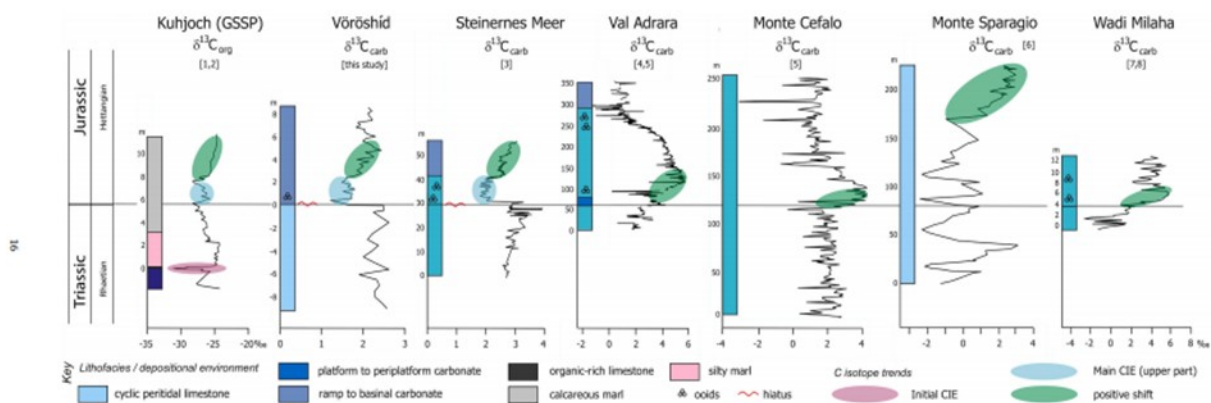


Figure 44: A comparison of seven T-J boundary sections from different studies. In this figure, Wadi Milaha (i.e. the Ghalilah Formation) has not been assigned a red line indicating a carbonate depositional hiatus (from Pálffy et al. 2021).



### 6.8.2 Ocean acidification in Wadi Ghalilah

Past studies of the Ghalilah Formation (e.g. Al-Suwaidi et al. 2016 & Hönig et al. 2017) have mainly proposed that ocean acidification was not a global phenomenon which affected the Wadi Ghalilah and Wadi Milaha after the ETME. However, field observations from this study did conclude that there is a sub-marine dissolution surface just below the first oolites in the Sakhra Member, indicating that a brief period of ocean acidification is still feasible despite the continuous carbonate deposition later on. This erosion surface is not visible in Wadi Ghalilah but can be seen clearly in Wadi Milaha below the Sakhra Member. Field evidence such as this smooth dissolved surface, nearby recycling of clasts, as well as the absence of cavities over a large area implies that this erosive surface was rather caused by acidification as opposed to subaerial exposure. Moreover, the selective nature of the extinction, its presence during a TST at the start of the Hettangian which is also visible on more global scales, tend to support the hypothesis of a short term acidification event even at these tropical latitudes (around 20 degrees South at this time, Stämpfli & Borel 2002). The presence of the subsequent distinctive anachronistic facies is then caused by the oversaturation of carbonates following the acidification event.

This would imply that there have been a widespread, perhaps even global, ocean acidification as a result from the CAMP eruptions. We do however not know with certainty how much of the Hettangian is actually missing in the geological record due to the resulting halt in carbonate deposition. Estimates of the Hettangian's duration is highly controversial, with ages of 2.0 +/- 0.5 Ma suggested in the present Geological Time Scale based on U-Pb dating from volcanic ashes (Ogg et al. 2016), 4.1 Myr by Weedon et al. (2019) based on ammonoid biostratigraphy and arguments of previously undiscovered hiatus. Estimates from the Mochras core in Wales which has an extremely well-preserved Early Jurassic record implies a 2.3+/-0.5 Myr age interval for the Hettangian (Storm et al. 2020). Most suggested ages fall around the 2.0 Myr range and considering these and a number of other suggested ages, Pálffy et al. (2021) argue that the hiatus at the T-J boundary is likely not longer than a few hundreds of thousands of years.

### 6.9 Comparison to modern day events

It is particularly interesting to study the ETME and its implications in regards to the current political climate and our global greenhouse gas emissions today. The similarities between the greenhouse gas emissions from the CAMP eruptions and modern time emissions are many. With a new historical high of 33,1 Gt in 2019 however, we now emit around 1100 times more

CO<sub>2</sub> per year than CAMP did annually during its 800 kyrs of activity, if we compare with the results of Heimdal et al. (2020) and annual CO<sub>2</sub> pollution (IEA 2019), and that is not counting any other greenhouse gases. Since the Earth is vastly different between the Mesozoic and modern day, applying the ETME as a perfect model for the future is highly unlikely, but the similarity between the excess greenhouse gas emissions makes it an interesting point for debate. This is also due to the fact that ocean acidification is a predicted effect of anthropogenic CO<sub>2</sub> emissions (Wootton et al. 2008, IPCC 2018). It is not possible to simply compare the difference in emissions and draw the conclusion that another mass extinction about 1000 times worse than the ETME will take place. Due to the differences in ocean water chemistry, thermohaline circulations, and buffering ability modern day oceans will likely not be affected in entirely the same way and rate as during the Mesozoic. What can be said however, is that calcifying organisms such as corals will be, and already are, particularly vulnerable to the drastic changes in pH and temperature which are already noticeable in the oceans. We already see the start of this in the form of coral bleaching, and at the rate this is proceeding it seems more likely than not that a scenario similar to the EMTE is not far from becoming a reality. It is therefore up to us if we will allow our own geological marine records to be erased by acidification, and only be followed by anachronistic facies marking the extinction we caused.

## 7 Conclusions

The early aftermath of the ETME has been studied in the Ghalilah Formation at Wadi Ghalilah. The lithology constitutes oolitic grainstones and thrombolites, interpreted as anachronistic facies. These facies, together with an underlying erosive surface visible at Wadi Milaha, are indications that ocean acidification was widespread in the Tethys Ocean, as it also affected the tropical latitudes of the UAE during the time corresponding to the T-J boundary interval. This acidification caused the disappearance of reef builders such as corals and other calcifying organisms, resulting in the Hettangian transgressions recorded at the boundary of the Sumra and Sakhra Members. The discussed 'unreefing model', as coined by Pálffy et al. (2021), could be used to describe the sea level oscillations transpiring at Wadi Ghalilah at the time of the T – J boundary. Mainly that the transgressions of the Hettangian can likely be attributed to the demise of many of the carbonate producing organisms in the Rhaetian, and that there is a shift from a rimmed carbonate shelf in the Rhaetian to a carbonate ramp in the Hettangian. The shallow marine environments present around Wadi Ghalilah and Wadi Milaha at the time of the ETME were highly sensitive to an environmental crisis of this

magnitude, which is also apparent in the ecosystem changes and the perturbations of the carbon cycle. The sedimentological, geochemical and biological changes can be correlated to the extreme influx of CO<sub>2</sub> to the ocean-atmospheric cycle at the time. The CAMP eruptions have thereby had sedimentological and geochemical consequences noticeable on a global scale.

Geochemical analyses of ooids have shown an increased amount of silicates in the nuclei of radial ooids, which could imply increased rates of continental weathering after the onset of the Hettangian. This weathering could have brought nutrients to the basin and promoted an increase in biological productivity at Wadi Ghalilah, as there is also an increase of P at this time. This increase can be indicative of higher levels of bottom water anoxia as a result of the increased biological productivity. This is also supported by a shift in Ce ratios between the time of deposition of the concentric and radial ooids, implying a slight increase in anoxic conditions.

To further investigate the aftermath of the ET-ME, more work could be done to analyze ooids from other globally recognized Hettangian marine sections to see if they display the same trends as shown in this study. Furthermore, there are other localities in the UAE, such as Wadi Naqab, which can be compared to these results similarly to Wadi Milaha.

## 8 Acknowledgements

Thank you to my supervisors Sylvain Richoz and Ingrid Urban for all their help ever since the start of the project. Their input and assistance is what made this thesis possible. A big thanks as well to Anders Lindskog who guided me through the process of making thin sections, Toms Naeraa for his help with conducting LA-ICP-MS and data processing in Iolite, and Mikael Calner for valuable input on the sedimentological interpretations.

## References

- Al-Suwaidi, A. H., Steuber, T., & Suarez, M. B., 2016: The Triassic-Jurassic boundary event from an equatorial carbonate platform (Ghalilah Formation, United Arab Emirates). *Journal of the Geological Society*, 173(6), 949-953. doi:10.1144/jgs2015-102
- Anderson, N. T., Cowan, C. A. & Bergmann, K. D., 2020: A case for the growth of ancient ooids within the sediment pile: *Journal of Sedimentary Research* 90, 843-854. doi: 10.2110/jsr.2020.45
- Ariztegui, D., Plee, K., Farah, R., Menzinger, N., & Pacton, M., 2012: Bridging the gap between biological and sedimentological processes in ooid formation: Crystalizing FA FOREL's vision. *Archives des Sciences* 65, 93-102.
- Bau, M. & Dulski, P., 1996: Distribution of yttrium and rare-earth elements in the Penge and Kuman iron-formations, Transvaal Supergroup, South Africa: *Precambrian Research* 79, 37-55. doi: 10.1016/0301-9268(95)00087-9
- Bonis, N. R. & Kuerschner, W. M., 2012: Vegetation history, diversity patterns, and climate change across the Triassic/Jurassic boundary: *Paleobiology* 38, 240-264. doi: 10.1666/09071.1.short
- Calner, M., 2005: A Late Silurian extinction event and anachronistic period: *Geology* 33, 305. doi: 10.1130/g21185.1
- Carozzi, A. V., (ed.) 1960: *Microscopic sedimentary petrography*. John Wiley & Sons, London. 485 pp
- Davies, J. H. F. L., Marzoli, A., Bertrand, H., Youbi, N., Ernesto, M. & Schaltegger, U., 2017: End-Triassic mass extinction started by intrusive CAMP activity: *Nature Communications* 8. 8 pp. doi: 10.1038/ncomms15596
- Deenen, M. H. L., Ruhl, M., Bonis, N. R., Krijgsman, W., Kuerschner, W. M., Reitsma, M. & Van Bergen, M. J., 2010: A new chronology for the end-Triassic mass extinction: *Earth and Planetary Science Letters* 291, 113-125. doi: 10.1016/j.epsl.2010.01.003
- De Matos, J.E. (1997). Stratigraphy, Sedimentation and Oil Potential of the Lower Jurassic to Kimmeridgian of the United Arab Emirates; Outcrop and Subsurface Compared: *PhD Thesis at the University of Aberdeen*.
- Diaz, M. R., Eberli, G. P., Blackwelder, P., Phillips, B., & Swart, P. K., 2017: Microbially mediated organomineralization in the formation of ooids. *Geology*, 45(9), 771-774.
- Duguid, S. M., Kyser, T. K., James, N. P., & Rankey, E. C., 2010: Microbes and ooids. *Journal of Sedimentary Research*, 80(3), 236-251.
- Dupraz, C., Reid, R. P., Braissant, O., Decho, A. W., Norman, R. S., & Visscher, P. T., 2009: Processes of carbonate precipitation in modern microbial mats. *Earth-Science Reviews* 96 (3), 141-162.
- Ge, Y., Al-Suwaidi, A., Shi, M., Li, Q., Morad, S. & Steuber, T., 2019: Short-term variation of ooid mineralogy in the Triassic-Jurassic boundary interval and its environmental implications: Evidence from the equatorial Ghalilah Formation, United Arab Emirates: *Global and Planetary Change* 182, 15 pp.
- Ge, Y., Shi, M., Steuber, T., Al-Suwaidi, A. H. & Suarez, M. B., 2018: Environmental change during the Triassic-Jurassic boundary interval of an equatorial carbonate platform: Sedimentology and chemostratigraphy of the Ghalilah Formation, United Arab Emirates: *Palaeogeography, Palaeoclimatology, Palaeoecology* 502, 86-103. doi: 10.1016/j.palaeo.2018.04.026
- German, C. R., & Elderfield, H., 1990: Application of

- the Ce anomaly as a paleoredox indicator: the ground rules. *Paleoceanography* 5(5), 823-833. doi:10.1029/PA005i005p00823
- Greene, S. E., Martindale, R. C., Ritterbush, K. A., Bottjer, D. J., Corsetti, F. A. & Berelson, W. M., 2012: Recognising ocean acidification in deep time: An evaluation of the evidence for acidification across the Triassic-Jurassic boundary: *Earth-Science Reviews* 113, 72-93. doi: 10.1016/j.earscirev.2012.03.009
- Groves, J. R. & Calner, M., 2004: Lower Triassic oolites in Tethys: a sedimentologic response to the end-Permian mass extinction: Geological Society of America annual meeting, Denver, 336.
- Guex, J., Pilet, S., Müntener, O., Bartolini, A., Spangenberg, J., Schoene, B., Sell, B., & Schaltegger, U., 2016: Thermal erosion of cratonic lithosphere as a potential trigger for mass-extinction. *Scientific reports* 6, 1-9 doi:10.1038/srep23168.
- Haley, B. A., Klinkhammer, G. P., & McManus, J. (2004). Rare earth elements in pore waters of marine sediments. *Geochimica et Cosmochimica Acta*, 68(6), 1265-1279. doi:10.1016/j.gca.2003.09.012
- Hautmann, M., Benton, M.J., Tomašových, A., 2008: Catastrophic ocean acidification at the Triassic-Jurassic boundary. *Neues Jahrbuch für Geologie und Paläontologie -Abhandlungen* 249 (1), 119–127.
- Hautmann, M., 2012: Extinction: End-Triassic Mass Extinction: eLS. doi: 10.1002/9780470015902.a0001655.pub3
- Heimdal, T. H., Callegaro, S., Svensen, H. H., Jones, M. T., Pereira, E. & Planke, S., 2019: Evidence for magma–evaporite interactions during the emplacement of the Central Atlantic Magmatic Province (CAMP) in Brazil: *Earth and Planetary Science Letters* 506, 476-492. doi: 10.1016/j.epsl.2018.11.018
- Heimdal, T. H., Jones, M. T. & Svensen, H. H., 2020: Thermogenic carbon release from the Central Atlantic magmatic province caused major end-Triassic carbon cycle perturbations: *Proceedings of the National Academy of Sciences* 117, 11968-11974. doi: 10.1073/pnas.2000095117
- Hillebrandt, A. V., Kuerschner, W. M., & Krystyn, L., 2007: A candidate GSSP for the base of the Jurassic in the Northern Calcareous Alps (Kuhjoch section, Karwendel Mountains, Tyrol, Austria): *ISJS Newsletter* 34, 2-20.
- Hillebrandt, A. V., Krystyn, L., Kuerschner, W. M., Bonis, N. R., Ruhl, M., Richo, S., Schnobben, M. a. N., Ulrichs, M., Bown, P. R., Kment, K., Mcroberts, C. A., Simms, M. & Tomasovych, A., 2013: The Global Stratotype Sections and Point (GSSP) for the base of the Jurassic System at Kuhjoch (Karwendel Mountains, Northern Calcareous Alps, Tyrol, Austria): *Episodes* 36 (2), 162-198.
- Hönig, M. R., John, C. M. & Manning, C., 2017: Development of an equatorial carbonate platform across the Triassic-Jurassic boundary and links to global palaeoenvironmental changes (Musandam Peninsula, UAE/Oman): *Gondwana Research* 45, 100-117. doi: 10.1016/j.gr.2016.11.007
- IEA, 2019: Report extract: Emissions. Downloaded 2021-05-19, from <https://www.iea.org/reports/global-energy-co2-status-report-2019/emissions>
- IPCC, 2018: Special Report: Global Warming of 1.5 °C. Downloaded 2021-03-10, from <https://www.ipcc.ch/sr15/chapter/spm/>
- Jochum, K. P., Scholz, D., Stoll, B., Weis, U., Wilson, S. A., Yang, Q., Schwalb, A., Börner, N., Jacob, D.E., & Andreae, M. O., 2012: Accurate trace element analysis of speleothems and biogenic calcium carbonates by LA-ICP-MS. *Chemical Geology* 318, 31-44.
- Jost, A. B., Bachan, A., van de Schootbrugge, B., Lau, K. V., Weaver, K. L., Maher, K. & Payne, J. L., 2017a: Uranium isotope evidence for an expansion of marine anoxia during the end-Triassic extinction: *Geochemistry, Geophysics, Geosystems* 18, 3093-3108. doi:10.1002/2017gc006941
- Kamber, B. S., & Webb, G. E., 2007: Transition metal abundances in microbial carbonate: a pilot study based on in situ LA-ICP-MS analysis. *Geobiology* 5(4), 375-389. doi:10.1111/j.1472-4669.2007.00129.x
- Kiessling, W., Aberhan, M., Brenneis, B. & Wagner, P. J., 2007: Extinction trajectories of benthic organisms across the Triassic–Jurassic boundary: *Palaeogeography, Palaeoclimatology, Palaeoecology* 244, 201-222. doi: 10.1016/j.palaeo.2006.06.029
- Klinkhammer, G. P. & Palmer, M. R., 1991: Uranium in the oceans: Where it goes and why: *Geochimica et Cosmochimica Acta* 55, 1799-1806. doi: 10.1016/0016-7037(91)90024-y
- Korte, C., Hesselbo, S. P., Jenkyns, H. C., Rickaby, R. E. M. & Spötl, C., 2009: Palaeoenvironmental significance of carbon- and oxygen-isotope stratigraphy of marine Triassic–Jurassic boundary sections in SW Britain: *Journal of the Geological Society* 166, 431-445.
- Li, F., Yan, J. X., Algeo, T., & Wu, X. Z., 2013: Paleoclimatic conditions following the end-Permian mass extinction recorded by giant ooids (Moyang, South China). *Global and Planetary Change* 105, 102-120. doi:10.1016/j.gloplacha.2011.09.009
- Li, F., Yan, J., Burne, R. V., Chen, Z.-Q., Algeo, T. J., Zhang, W., Tian, L., Gan, Y., Liu, K. & Xie, S., 2017: Paleo-seawater REE compositions and

- microbial signatures preserved in laminae of Lower Triassic ooids: *Palaeogeography, Palaeoclimatology, Palaeoecology* 486, 96-107. doi: 10.1016/j.palaeo.2017.04.005
- Lindström, S., 2016: Palynofloral patterns of terrestrial ecosystem change during the end-Triassic event – a review. *Geol. Mag.* 153 (2), 223 – 251.
- Lindström, S., 2020: Tracing volcanic emissions from the Central Atlantic Magmatic Province in the sedimentary record. *Earth-Science Reviews* 212, 103444
- Lucas, S. G. & Tanner, L. H., 2008: Reexamination of the end-Triassic mass extinction. In Elewa A. M. T. (ed.): Mass Extinction, 65-102. *Topics in Geobiology* 46.
- Lucas, S. G. & Tanner, L. H. 2018: The Missing Mass Extinction at the Triassic-Jurassic Boundary. In Tanner, L. H. (ed.): The Late Triassic World, 721-785. *Topics in Geobiology* 46.
- Marzoli, A., Callegaro, S., Dal Corso, J., Davies, J. H. F. L., Chiaradia, M., Youbi, N., Bertrand, H., Reisberg, L., Merle, R. & Jourdan, F. 2018: The Central Atlantic Magmatic Province (CAMP): A Review. In Tanner, L. H. (ed.): The Late Triassic World, 91-125. *Topics in Geobiology* 46.
- Maurer, F., Rettori, R. & Martini, R., 2008: Triassic stratigraphy, facies and evolution of the Arabian shelf in the northern United Arab Emirates: *International Journal of Earth Sciences* 97, 765-784. doi: 10.1007/s00531-007-0194-y
- McElwain, J. C., 1999: Fossil Plants and Global Warming at the Triassic-Jurassic Boundary: *Science* 285, 1386-1390. doi: 10.1126/science.285.5432.1386
- McHone, J., 2003: Volatile emissions from Central Atlantic Magmatic Province basalts: mass assumptions and environmental consequences.: *American Geophysical Union* 136, 241-254.
- McLennan, S. M., 1989: Chapter 7. Rare Earth Elements in Sedimentary Rocks: Influence of Provenance and Sedimentary Processes. In Lipin, B. R., & McKay, G. A., (eds.): Geochemistry and Mineralogy of Rare Earth Elements, 169-200. *Reviews in Mineralogy & Geochemistry* 21.
- McLennan, S. M., 2001: Relationships between the trace element composition of sedimentary rocks and upper continental crust: *Geochem. Geophys. Geosys* 2, 24 pp.
- McRoberts, C. A., Furrer, H. & Jones, D. S., 1997: Palaeoenvironmental interpretation of a Triassic-Jurassic boundary section from Western Australia based on palaeoecological and geochemical data: *Palaeogeography, Palaeoclimatology, Palaeoecology* 136, 79-95. doi: 10.1016/s0031-0182(97)00074-6
- Newsome, L., Morris, K. & Lloyd, J. R., 2014: The biogeochemistry and bioremediation of uranium and other priority radionuclides: *Chemical Geology* 363, 164-184. doi: 10.1016/j.chemgeo.2013.10.034
- Nomade, S., Knight, K. B., Beutel, E., Renne, P. R., Verati, C., Féraud, G., Marzoli, A., Youbi, N. & Bertrand, H., 2007: Chronology of the Central Atlantic Magmatic Province: Implications for the Central Atlantic rifting processes and the Triassic–Jurassic biotic crisis: *Palaeogeography, Palaeoclimatology, Palaeoecology* 244, 326-344. doi: 10.1016/j.palaeo.2006.06.034
- Ogg, J. G., Ogg, G. M., Gradstein, F. M., (eds) 2016: *A Concise Geologic Time Scale 2016*. Elsevier, Amsterdam. 240 pp.
- Olsen, P. E., 2002: Ascent of Dinosaurs Linked to an Iridium Anomaly at the Triassic-Jurassic Boundary: *Science* 296, 1305-1307. doi: 10.1126/science.1065522
- Pálfy, J., 2000: Timing the end-Triassic mass extinction: First on land, then in the sea?: *Geology* 28, 39-42. doi: 10.1130/0091-7613(2000)28
- Pálfy, J., Demény, A., Haas, J., Carter, E. S., Görög, Á., Halász, D., Oravecz-Scheffer, A., Hetényi, M., Márton, E., Orchard, M. J., Ozsvárt, P., Vető, I. & Zajzon, N., 2007: Triassic–Jurassic boundary events inferred from integrated stratigraphy of the Csövár section, Hungary: *Palaeogeography, Palaeoclimatology, Palaeoecology* 244, 11-33. doi: 10.1016/j.palaeo.2006.06.021
- Pálfy, J., Kovács, Z., Demény, A. & Vallner, Z., 2021: End-Triassic crisis and “unreefing” led to the demise of the Dachstein carbonate platform: A revised model and evidence from the Transdanubian Range, Hungary: *Global and Planetary Change* 199, 103428. doi: 10.1016/j.gloplacha.2021.103428
- Paton, C., Hellstrom, J., Paul, B., Woodhead, J., & Hergt, J., 2011: Iolite: Freeware for the visualization and processing of mass spectrometric data. *Journal of Analytical Atomic Spectrometry* 26(12), 2508-2518. doi:10.1039/c1ja10172b
- Percival, L. M. E., Ruhl, M., Hesselbo, S. P., Jenkyns, H. C., Mather, T. A. & Whiteside, J. H., 2017: Mercury evidence for pulsed volcanism during the end-Triassic mass extinction: *Proceedings of the National Academy of Sciences* 114, 7929-7934. doi: 10.1073/pnas.1705378114
- Piepgras, D. J., & Jacobsen, S. B., 1992: The behavior of rare-earth elements in seawater – precise determination of variations in the north pacific water column. *Geochimica et Cosmochimica Acta* 56(5), 1851-1862. doi:10.1016/0016-7037

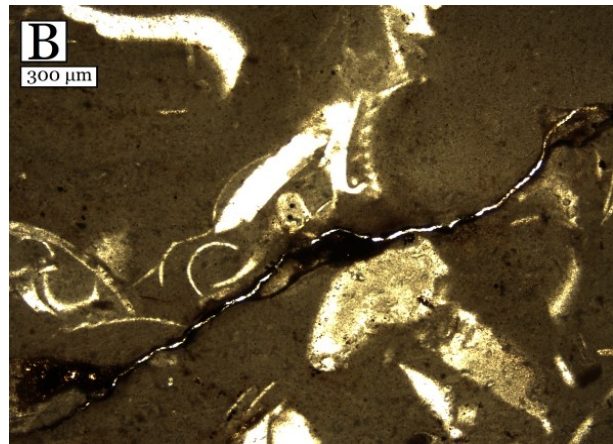
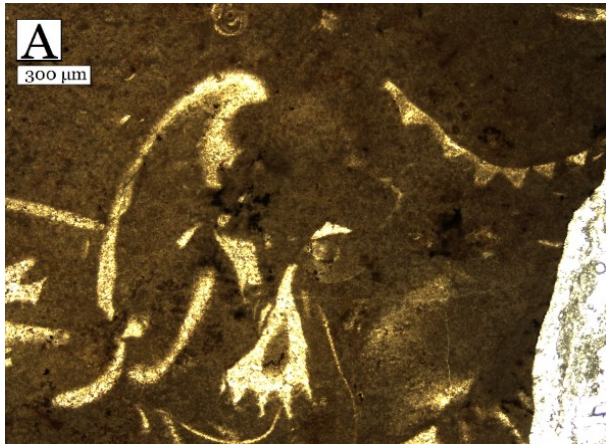
- (92)90315-a
- Plee, K., Ariztegui, D., Martini, R., & Davaud, E., 2008: Unravelling the microbial role in ooid formation—results of an in situ experiment in modern freshwater Lake Geneva in Switzerland. *Geobiology* 6(4), 341-350.
- Raup, D. M. & Sepkoski, J. J., 1982: Mass Extinctions in the Marine Fossil Record: *Science* 215, 1501-1503. doi: 10.1126/science.215.4539.1501
- Baud, A., Richoz, S., & Pruss, S., 2007: The lower Triassic anachronistic carbonate facies in space and time: *Global and Planetary Change* 55, 81-89.
- Richoz, S., van de Schootbrugge, B., Pross, J., Püttmann, W., Quan, T. M., Lindström, S., Heunisch, C., Fiebig, J., Maquil, R., Schouten, S., Hauzenberger, C. A. & Wignall, P. B., 2012: Hydrogen sulphide poisoning of shallow seas following the end-Triassic extinction: *Nature Geoscience* 5, 662-667. doi: 10.1038/ngeo1539
- Riding, R., 2006: Cyanobacterial calcification, carbon dioxide concentrating mechanisms, and Proterozoic-Cambrian changes in atmospheric composition. *Geobiology* 4(4), 299-316. doi:10.1111/j.1472-4669.2006.00087.x
- Riding, R. 2011: Microbialites, Stromatolites, and Thrombolites. In Reitner, J., & Thiel, V., (eds): *Encyclopedia of Geobiology*, 635-654. Springer, Netherlands.
- Roberts, N. M. W., Thomas, R. J. & Jacobs, J., 2016: Geochronological constraints on the metamorphic sole of the Semail ophiolite in the United Arab Emirates: *Geoscience Frontiers* 7, 609-619. doi: 10.1016/j.gsf.2015.12.003
- Ruhl, M., Deenen, M. H. L., Abels, H. A., Bonis, N. R., Krijgsman, W. & Kürschner, W. M., 2010: Astronomical constraints on the duration of the early Jurassic Hettangian stage and recovery rates following the end-Triassic mass extinction (St Audrie's Bay/East Quantoxhead, UK): *Earth and Planetary Science Letters* 295, 262-276. doi: 10.1016/j.epsl.2010.04.008
- Ruhl, M., Hesselbo, S. P., Al-Suwaidi, A., Jenkyns, H. C., Damborenea, S. E., Manceñido, M. O., Storm, M., Mather, T. A. & Riccardi, A. C., 2020: On the onset of Central Atlantic Magmatic Province (CAMP) volcanism and environmental and carbon-cycle change at the Triassic–Jurassic transition (Neuquén Basin, Argentina): *Earth-Science Reviews* 208, 103229. doi: 10.1016/j.earscirev.2020.103229
- Sandberg, P. A., 1983: An oscillating trend in Phanerozoic non-skeletal carbonate mineralogy. *Nature* 305 (5929), 19-22.
- Schaller, M. F., Wright, J. D. & Kent, D. V., 2011: Atmospheric pCO<sub>2</sub> Perturbations Associated with the Central Atlantic Magmatic Province: *Science* 331, 1404-1409. doi: 10.1126/science.1199011
- Schaller, M. F., Wright, J. D., Kent, D. V. & Olsen, P. E., 2012: Rapid emplacement of the Central Atlantic Magmatic Province as a net sink for CO<sub>2</sub>: *Earth and Planetary Science Letters* 323, 27-39. doi: 10.1016/j.epsl.2011.12.028
- Schaltegger, U., Guex, J., Bartolini, A., Schoene, B. & Ovtcharova, M., 2008: Precise U–Pb age constraints for end-Triassic mass extinction, its correlation to volcanism and Hettangian post-extinction recovery: *Earth and Planetary Science Letters* 267, 266-275. doi: 10.1016/j.epsl.2007.11.031
- Searle, M. P., 1988: Thrust tectonics of the Dibba zone and the structural evolution of the Arabian continental margin along the Musandam mountains (Oman and United Arab Emirates): *Journal of the Geological Society* 145, 43-53. doi: 10.1144/gsjgs.145.1.0043
- Sepkoski, J. J., Bambach, R. K. & Droser, M. L., 1991: Secular changes in Phanerozoic event bedding and the biological imprint. In Einsele, G., Ricken, W., & Seilacher, A., (eds.): *Cycles and events in stratigraphy*, 298-312. Springer, Berlin.
- Sereno, P. C., 1999: The Evolution of Dinosaurs: *Science* 284, 2137-2147. doi: 10.1126/science.284.5423.2137
- Shields, G., Stille, P., 2001. Diagenetic constraints on the use of cerium anomalies as palaeoseawater redox proxies: an isotopic and REE study of Cambrian phosphorites. *Chemical Geology*, 175(1–2), 29-48.
- Smith, K. S., Jakubzick, C., Whittam, T. S., & Ferry, J. G., 1999: Carbonic anhydrase is an ancient enzyme widespread in prokaryotes. *Proceedings of the National Academy of Sciences of the United States of America* 96(26), 15184-15189. doi:10.1073/pnas.96.26.15184
- Stanley, G., 1983: The History of Early Mesozoic Reef Communities: A Three-Step Process: *Society for Sedimentary Geology* 3, 170-183.
- Stanley, G. D., 2003: The evolution of modern corals and their early history: *Earth-Science Reviews* 60, 195-225. doi: 10.1016/s0012-8252(02)00104-6
- Stanley, G. D. & Beauvais, L., 1994: Corals from an Early Jurassic coral reef in British Columbia: refuge on an oceanic island reef: *Lethaia* 27, 35-47. doi: 10.1111/j.1502-3931.1994.tb01553.x
- Stanley, S. & Hardie, L., 1999: Hypercalcification: Paleontology Links Plate Tectonics and Geochemistry to Sedimentology: *GSA Today* 9, 1-6.
- Steinhorsdottir, M., Jeram, A. J. & McElwain, J. C., 2011: Extremely elevated CO<sub>2</sub> concentrations

- at the Triassic/Jurassic boundary: *Palaeogeography, Palaeoclimatology, Palaeoecology* 308, 418-432. doi: 10.1016/j.palaeo.2011.05.050
- Steinthorsdottir, M., Woodward, F. I., Surlyk, F. & Mcelwain, J. C., 2012: Deep-time evidence of a link between elevated CO<sub>2</sub> concentrations and perturbations in the hydrological cycle via drop in plant transpiration: *Geology* 40, 815-818. doi: 10.1130/g33334.1
- Storm, M. S., Hesselbo, S. P., Jenkyns, H. C., Ruhl, M., Ullman, C. V., Xu, W., Leng, M. J., Riding, J. B., & Gorbanenko, O., 2020: Orbital pacing and secular evolution of the Early Jurassic carbon cycle: *Proc. Natl. Acad. Sci.* 117 (8), 3974 – 3982.
- Stampfli, G. M. & Borel, G. D., 2002: A plate tectonic model for the Paleozoic and Mesozoic constrained by dynamic plate boundaries and restored synthetic oceanic isochrons: *Earth and Planetary Science Letters* 196, 17-33. doi: 10.1016/s0012-821x(01)00588-x
- Tanner, L. H., Kyte, F. T., Richoz, S. & Krystyn, L., 2016: Distribution of iridium and associated geochemistry across the Triassic–Jurassic boundary in sections at Kuhjoch and Kendlbach, Northern Calcareous Alps, Austria: *Palaeogeography, Palaeoclimatology, Palaeoecology* 449, 13-26. doi: 10.1016/j.palaeo.2016.01.011
- Takahashi, Y., Chatellier, X., Hattori, K. H., Kato, K., & Fortin, D., 2005: Adsorption of rare earth elements onto bacterial cell walls and its implication for REE sorption onto natural microbial mats. *Chemical Geology* 219(1-4), 53-67. doi:10.1016/j.chemgeo.2005.02.009
- Tegner, C., Marzoli, A., McDonald, I., Youbi, N. & Lindström, S., 2020: Platinum-group elements link the end-Triassic mass extinction and the Central Atlantic Magmatic Province: *Scientific Reports* 10 (3482). doi: 10.1038/s41598-020-60483-8
- Tribouillard, N., Algeo, T. J., Lyons, T. & Riboulleau, A., 2006: Trace metals as paleoredox and paleoproductivity proxies: An update: *Chemical Geology* 232, 12-32. doi: 10.1016/j.chemgeo.2006.02.012
- Tucker, M.E., Wilson, J.L., Crevello, P.D., Sarg, J.R., Read, J.F., (eds) 1990. *Carbonate platforms. Facies, sequences and evolution*. Spec. Publ. Int. Assoc. Sedimentologists, 9, Oxford, 328 pp.
- van de Schootbrugge, B., Bachan, A., Suan, G., Richoz, S. & Payne, J. L., 2013: Microbes, mud and methane: cause and consequence of recurrent Early Jurassic anoxia following the end-Triassic mass extinction: *Palaeontology* 56, 685-709. doi: 10.1111/pala.12034
- van de Schootbrugge, B., Quan, T. M., Lindström, S., Püttmann, W., Heunisch, C., Pross, J., Fiebig, J., Petschick, R., Röhlhling, H. G., Richoz, S., Rosenthal, Y. & Falkowski, P. G., 2009: Floral changes across the Triassic/Jurassic boundary linked to flood basalt volcanism: *Nature Geoscience* 2, 589-594. doi: 10.1038/ngeo577
- van de Schootbrugge, B. & Wignall, P. B., 2016: A tale of two extinctions: converging end-Permian and end-Triassic scenarios: *Geological Magazine* 153, 332-354. doi: 10.1017/s0016756815000643
- Weedon, G. P., Page, K. N. & Jenkyns, H. C., 2019: Cyclostratigraphy, stratigraphic gaps and the duration of the Hettangian Stage (Jurassic): insights from the Blue Lias Formation of southern Britain: *Geological Magazine* 156, 1469-1509. doi: 10.1017/s0016756818000808
- Wignall, P. B., & Twitchett, R. J., 1996: Oceanic Anoxia and the End Permian Mass Extinction: *Science* 272, 1155-1158. doi: 10.1126/science.272.5265.1155
- Wignall, P. B., 2001: Large igneous provinces and mass extinctions: *Earth-Science Reviews* 53, 1-33. doi: 10.1016/s0012-8252(00)00037-4
- Woods, A. D., Bottjer, D. J., Mutti, M. & Morrison, J., 1999: Lower Triassic large sea-floor carbonate cements: their origin and a mechanism for the prolonged biotic recovery from the end-Permian mass extinction: *Geology* 27, 645-648.
- Wootton, J. T., Pfister, C. A. & Forester, J. D., 2008: Dynamic patterns and ecological impacts of declining ocean pH in a high-resolution multi-year dataset: *Proceedings of the National Academy of Sciences* 105, 18848-18853. doi: 10.1073/pnas.0810079105
- Ziegler, M.A., 2001: Late Permian to Holocene paleofacies evolution of the Arabian Plate and its hydrocarbon occurrences. *GeoArabia* 6 (3), 445–504.

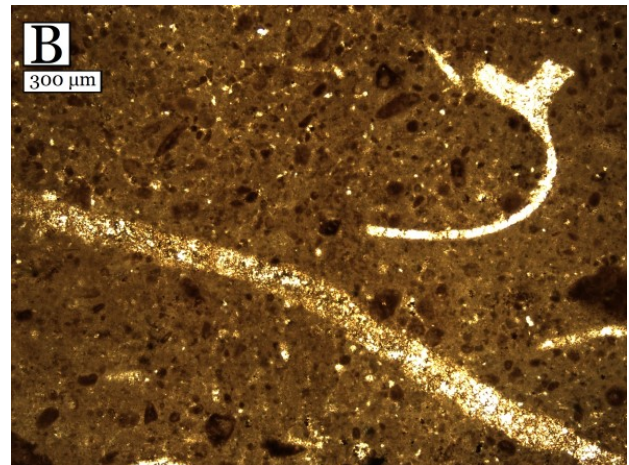
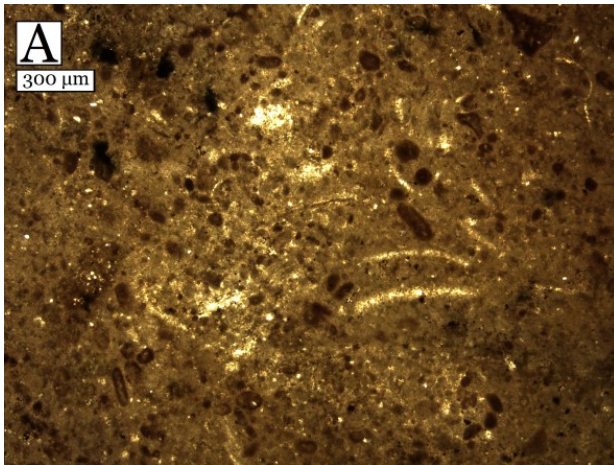


## Appendix 1—Thin section images

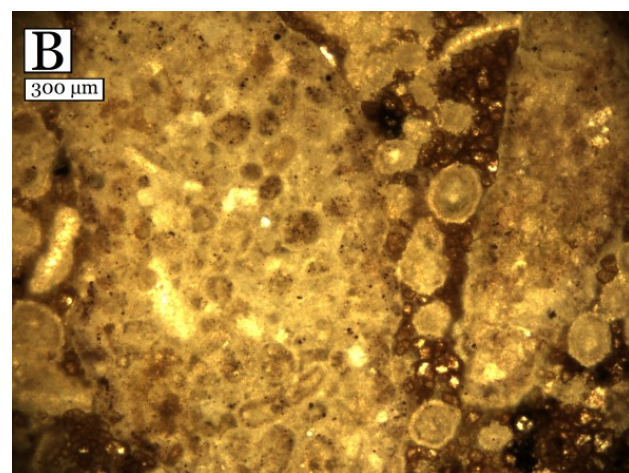
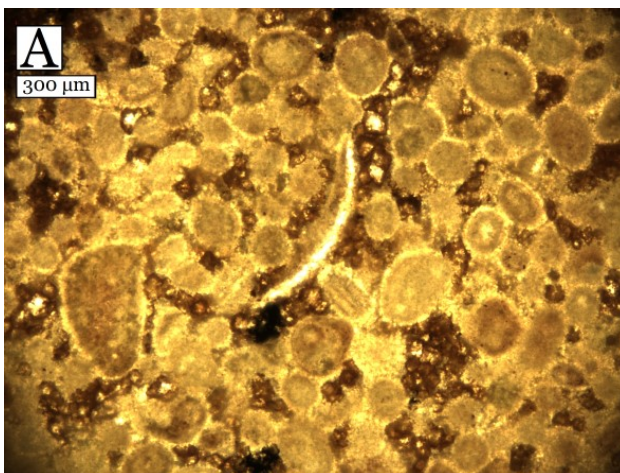
Two images (A&B) for each sample.



*WG1: A & B in PPL*

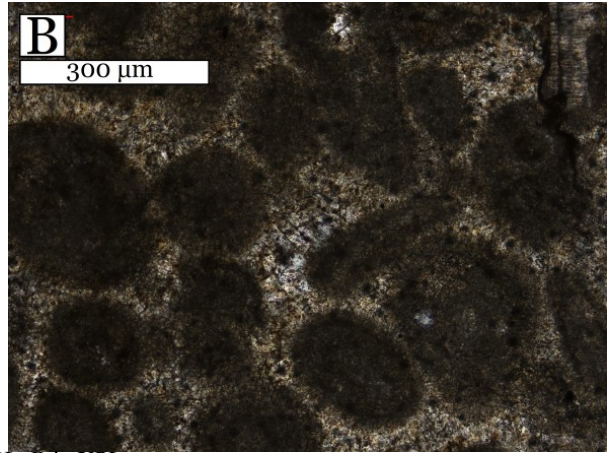
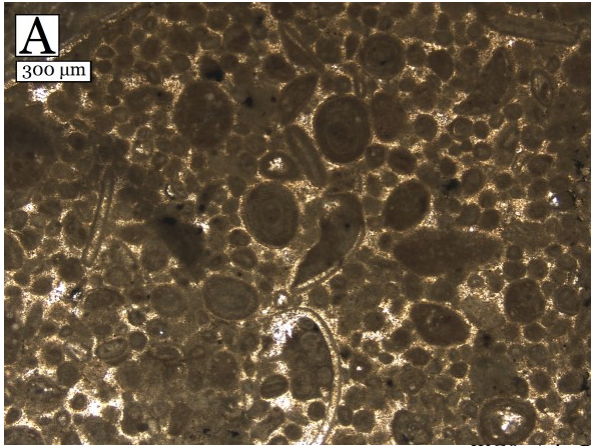


*WG6: A & B in PPL*

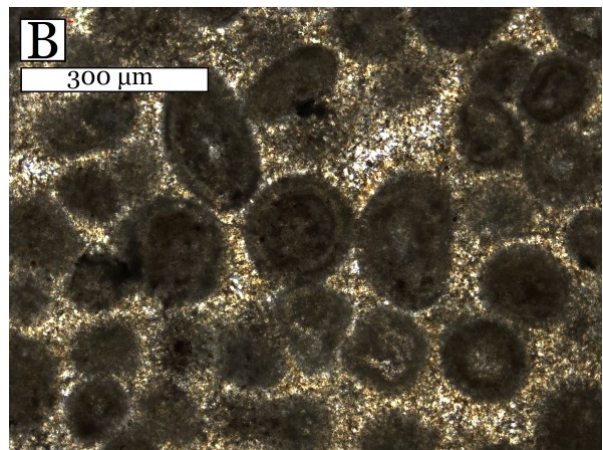
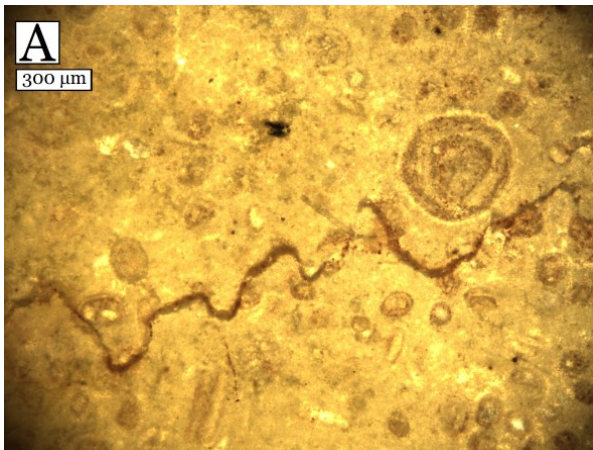


*WG7: A & B in PPL*

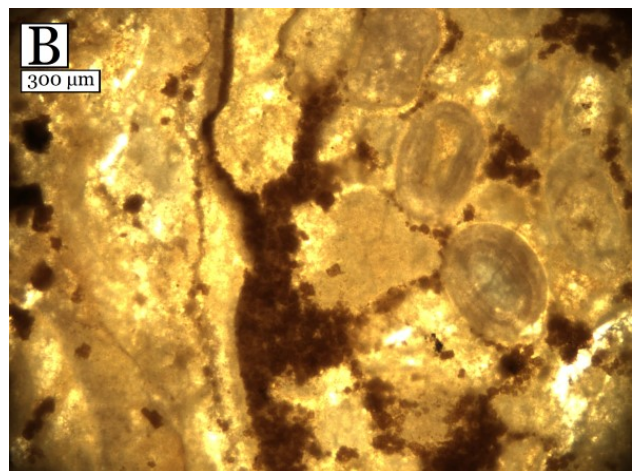
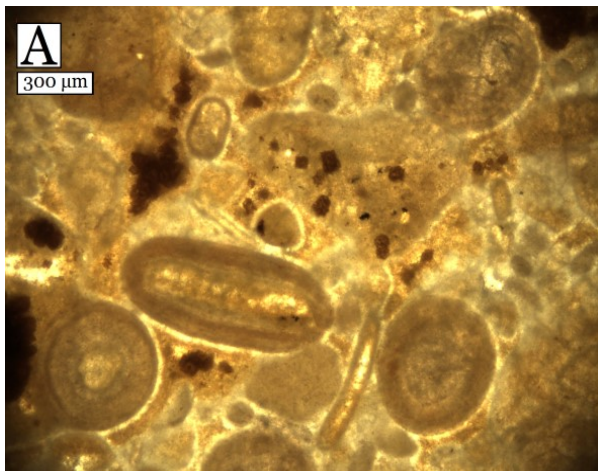




*WG8*: A in PPL, B in XPL

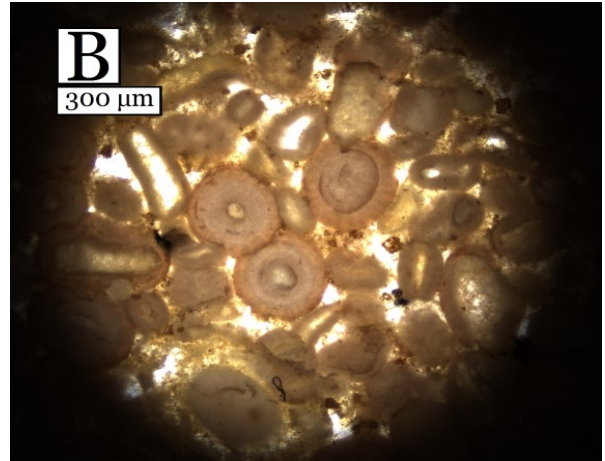
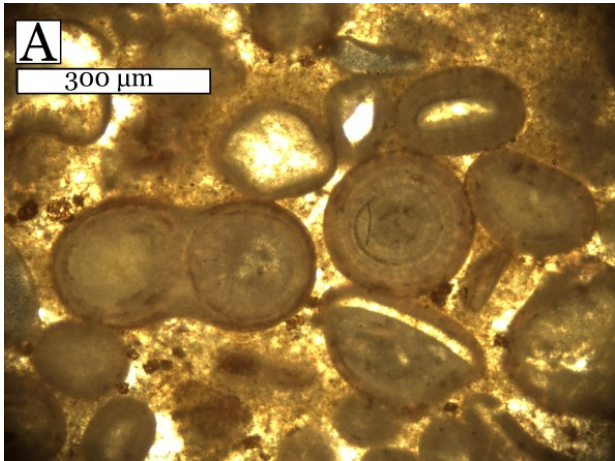


*WG9*: A in PPL, B in XPL

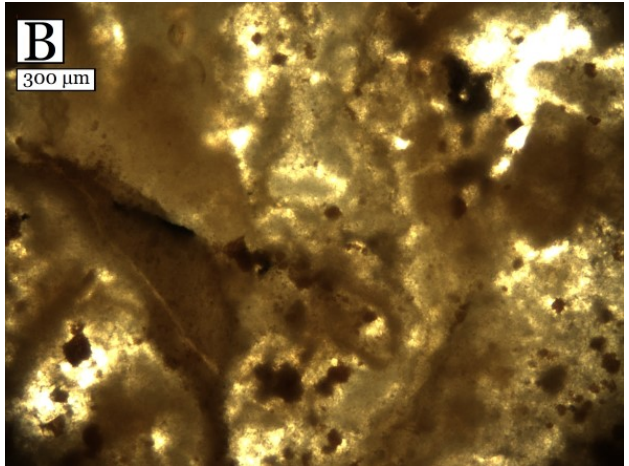
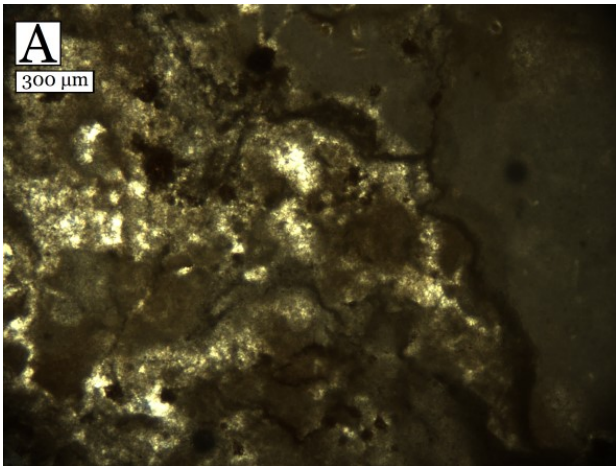


*WG11*: A & B in PPL

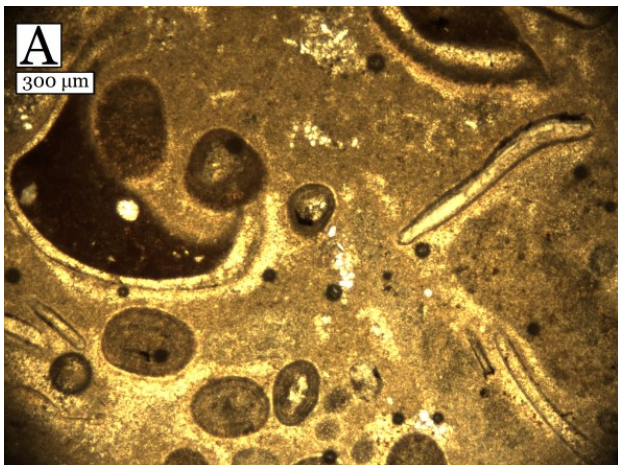




*WG12A*: A & B in PPL

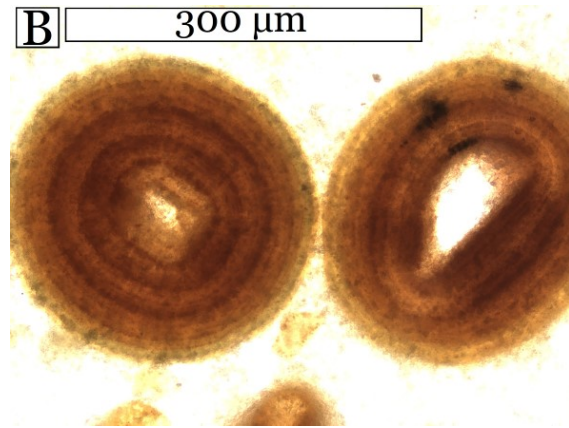
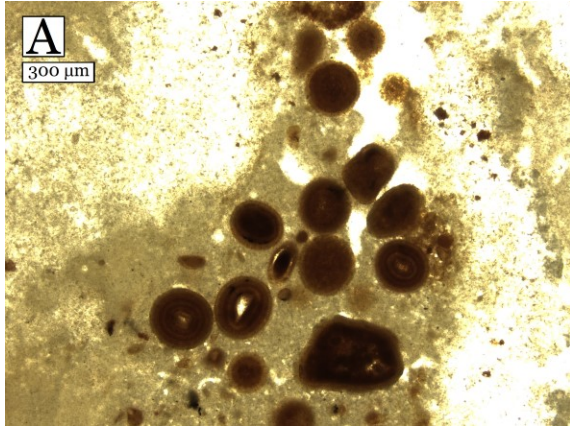


*WG12B*: A in XPL, B in PPL

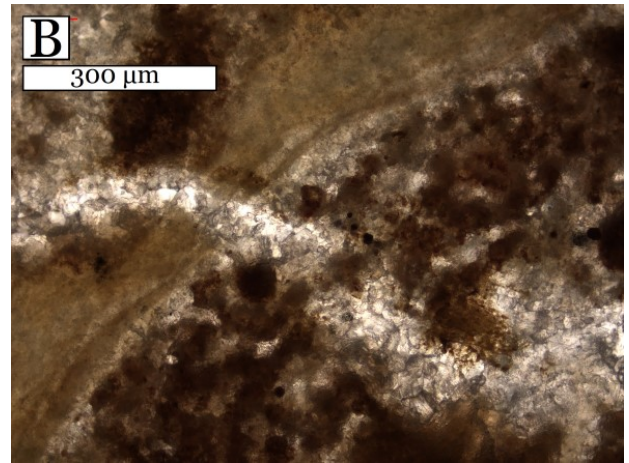


*WG13*: A & B in PPL

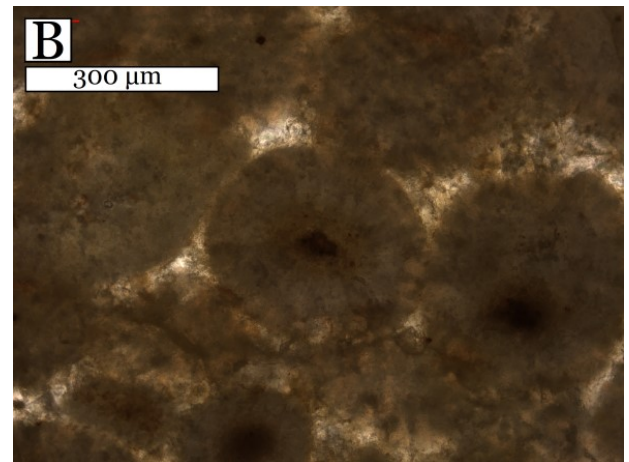
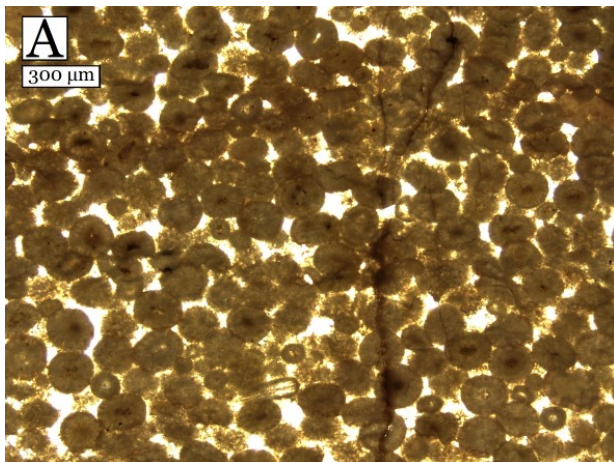




WG14: A & B in PPL

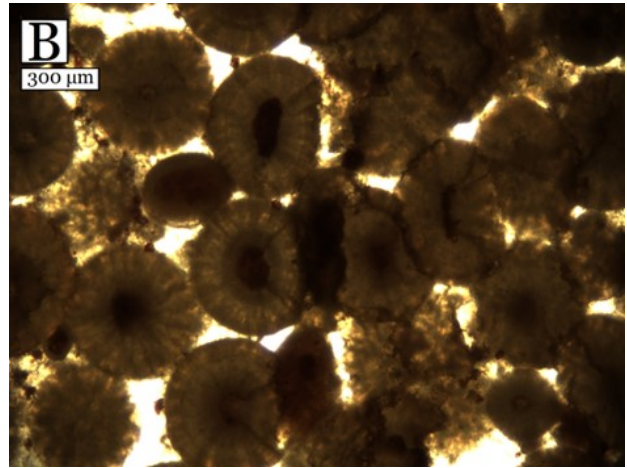
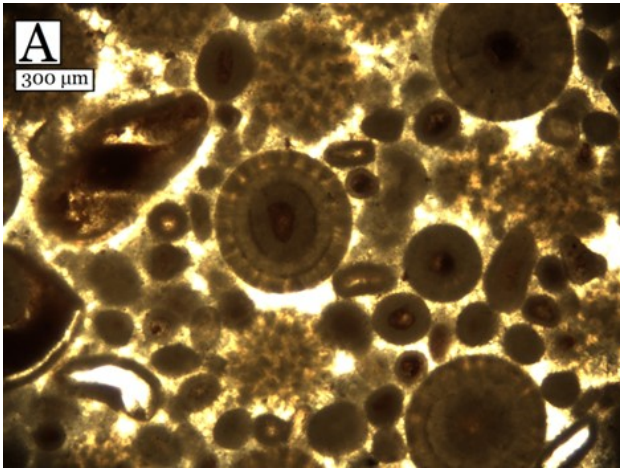


WG15: A & B in PPL

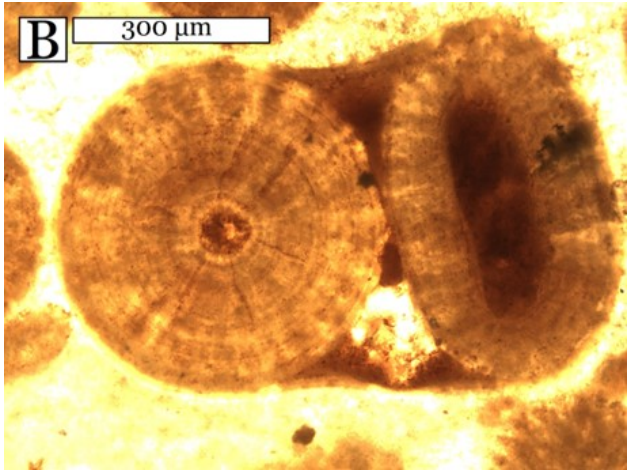
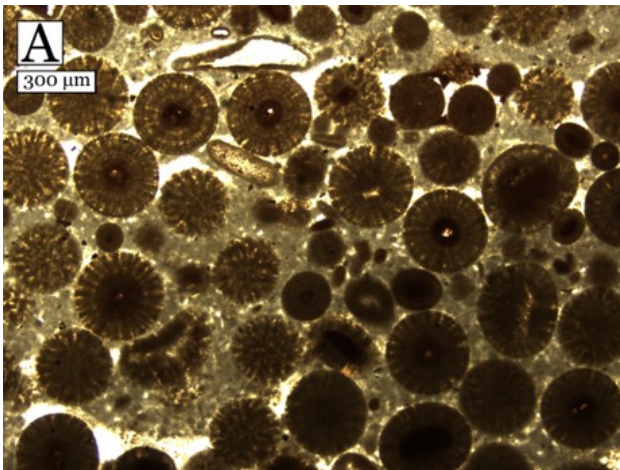


WG17: A & B in PPL

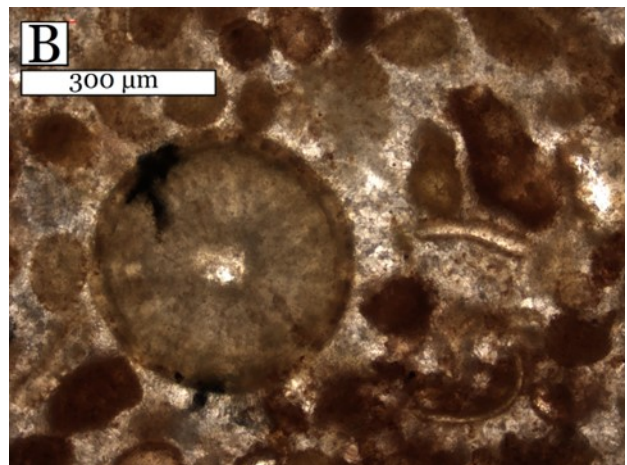
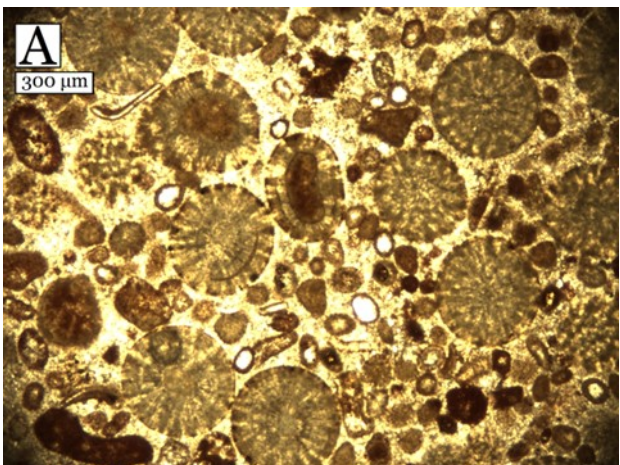




*WG18: A & B in PPL*

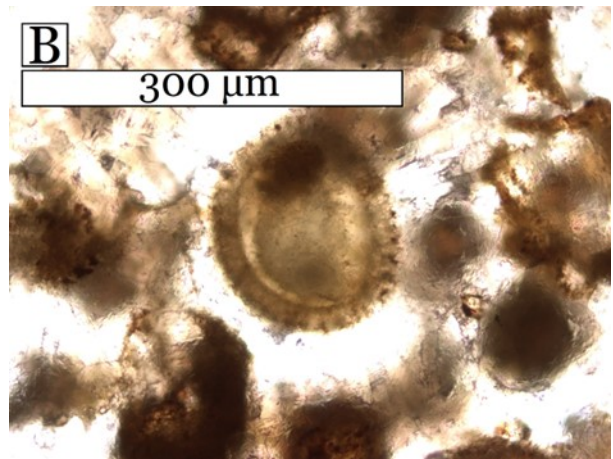
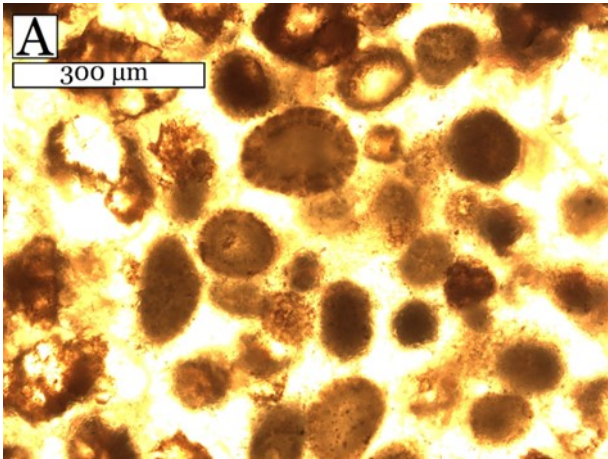


*WG19: A & B in PPL*

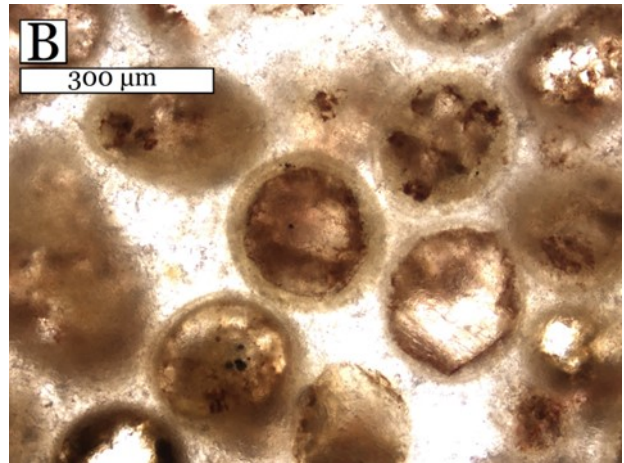
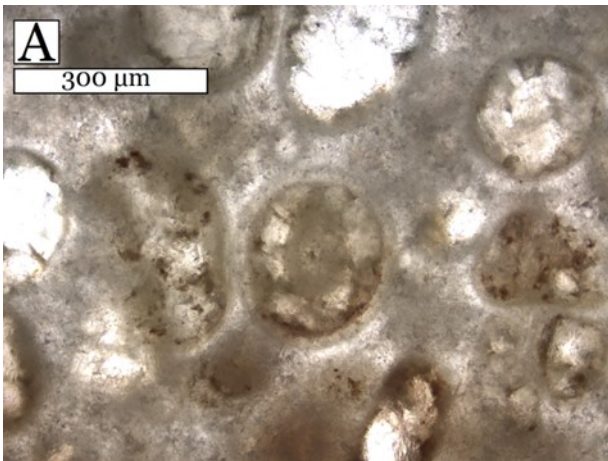


*WG20: A & B in PPL*

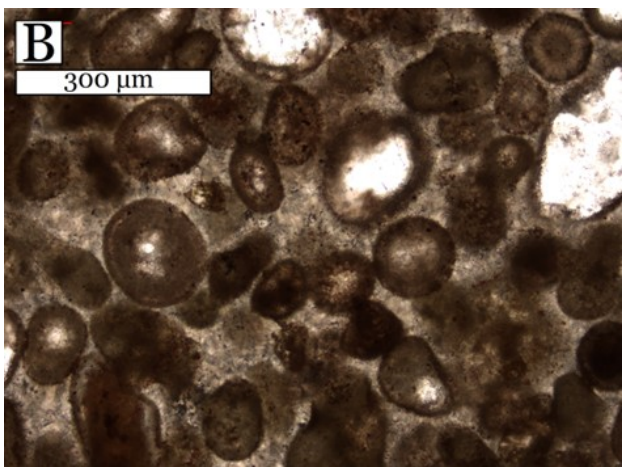
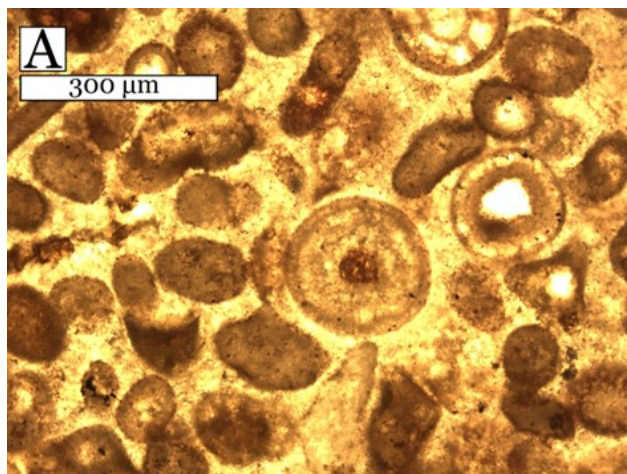




WG23: A & B in PPL

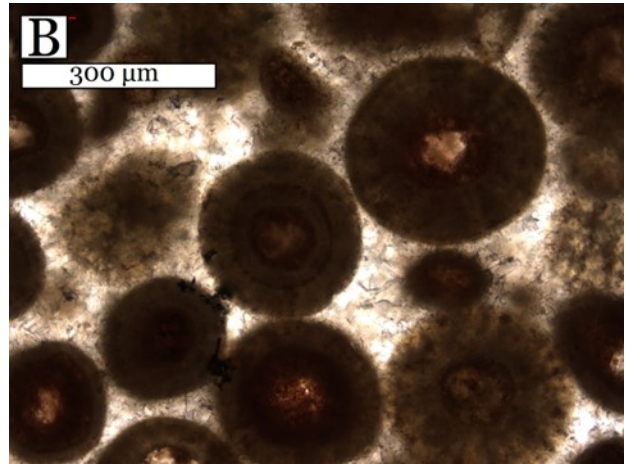
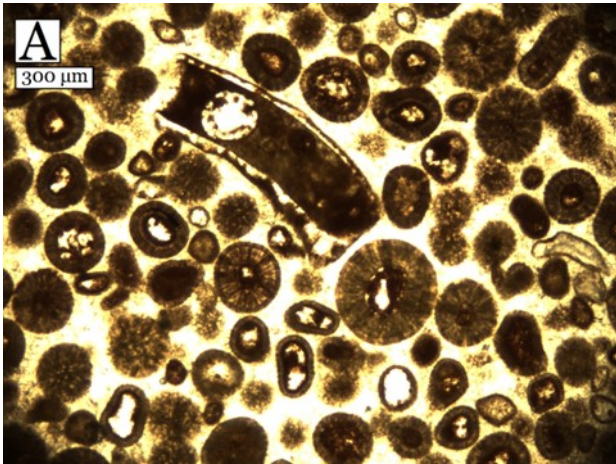


WG24: A & B in PPL

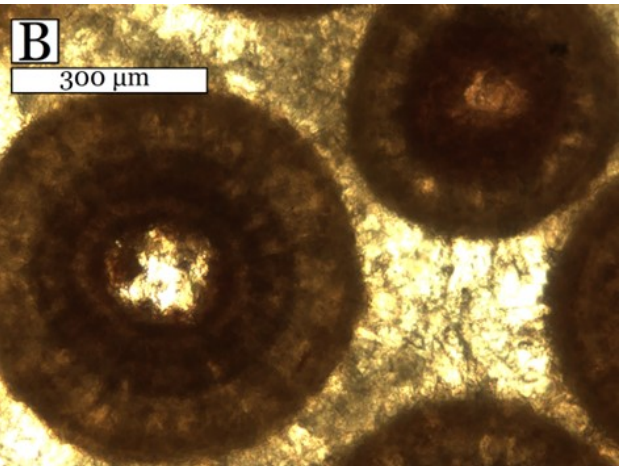
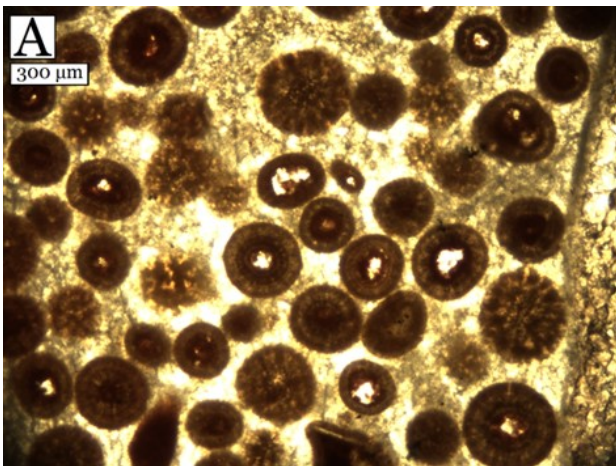


WG25: A in PPL, B in XPL

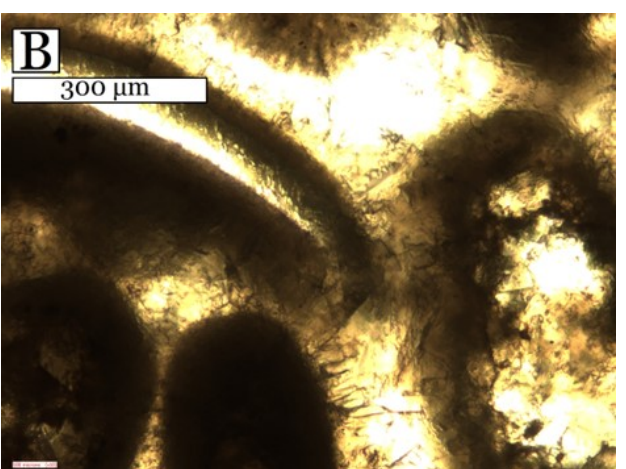
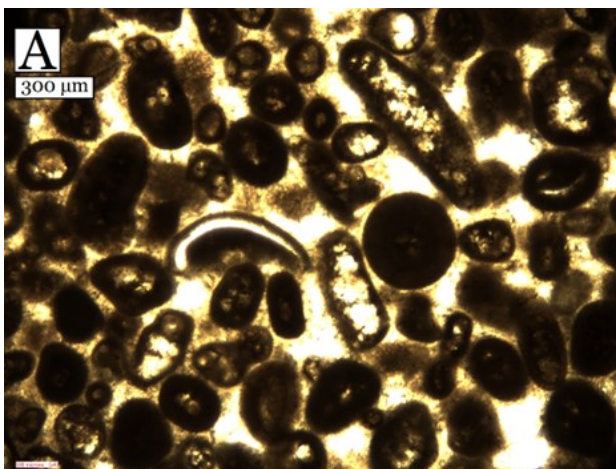




WG26: A & B in PPL

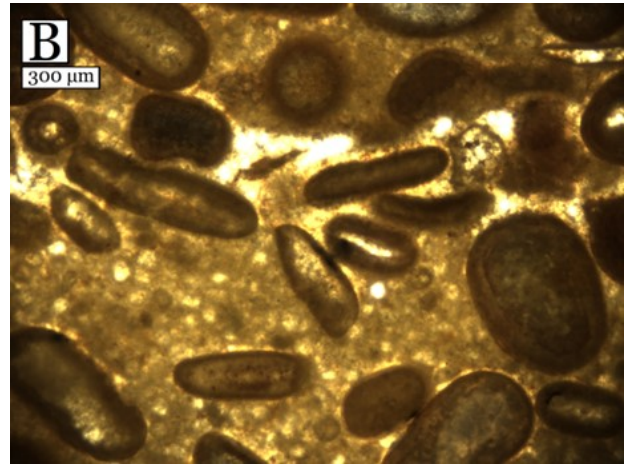
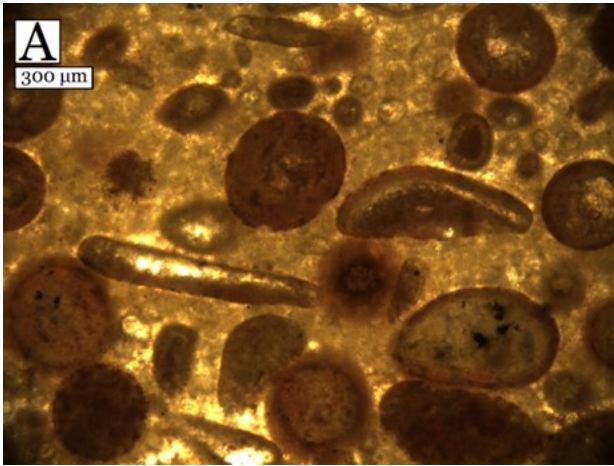


WG27: A & B in PPL

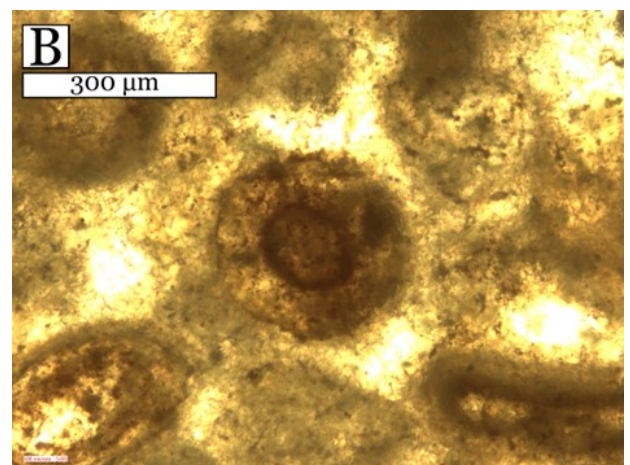
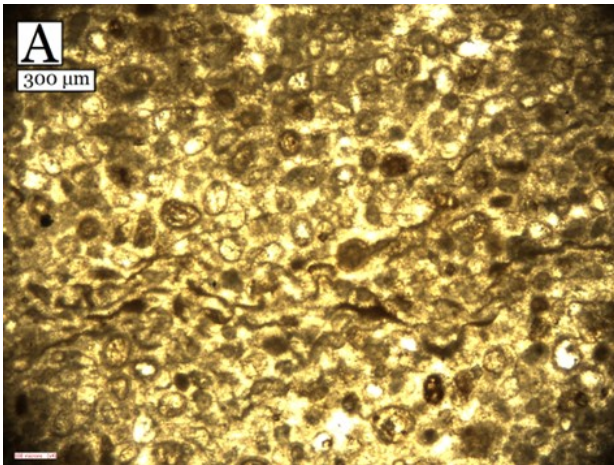


WG28: A & B in PPL

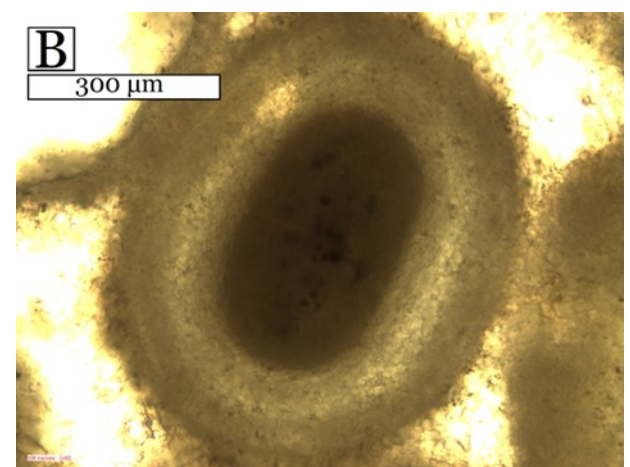
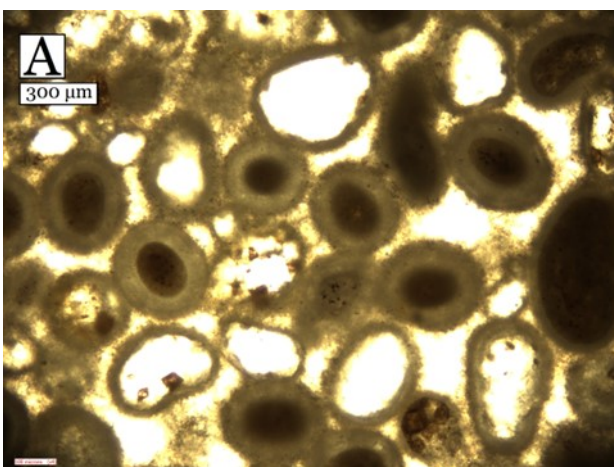




*WG29*: A & B in PPL

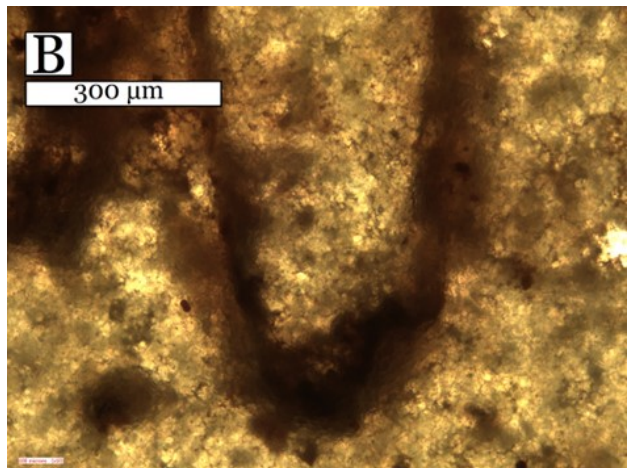
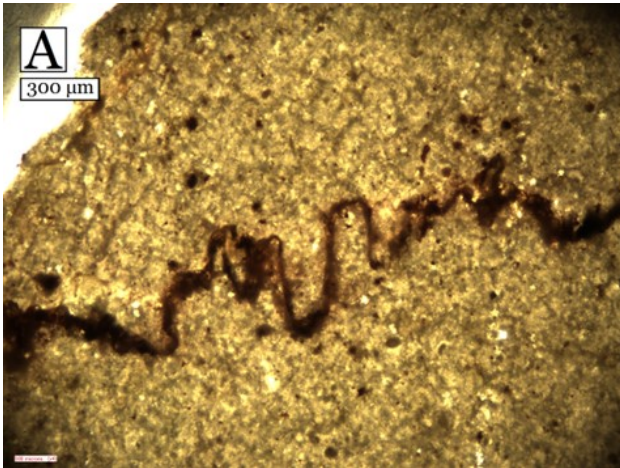


*WG31*: A & B in PPL

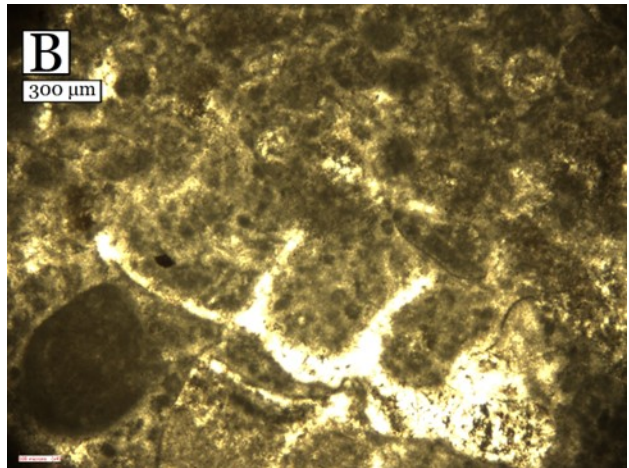
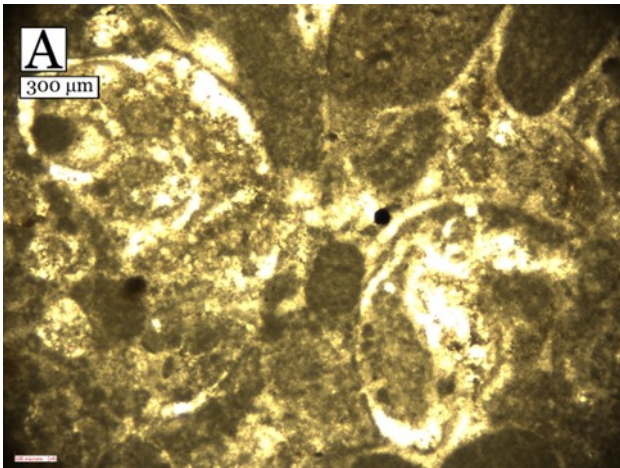


*WG33*: A & B in PPL

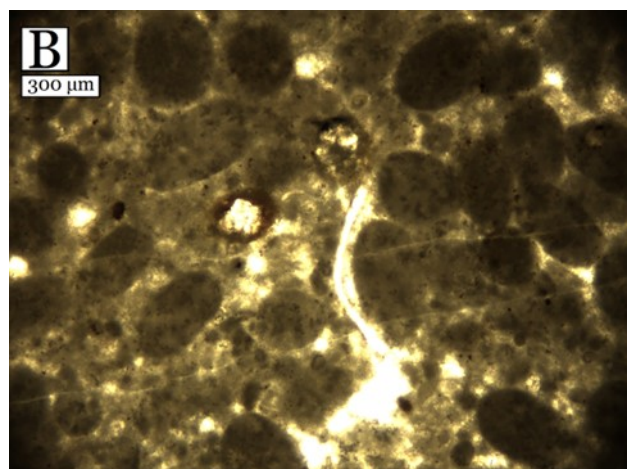
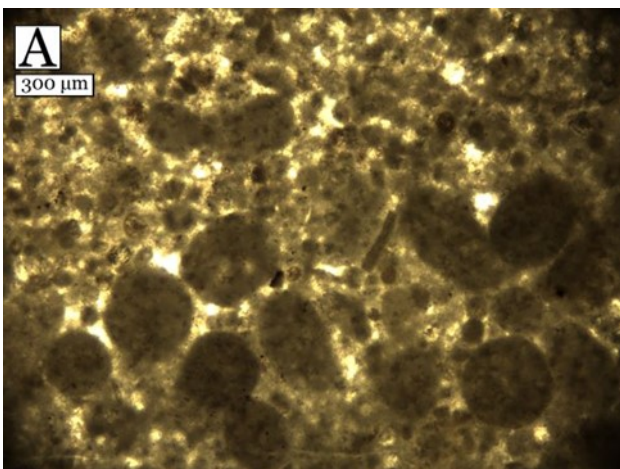




*WG34: A & B in PPL*

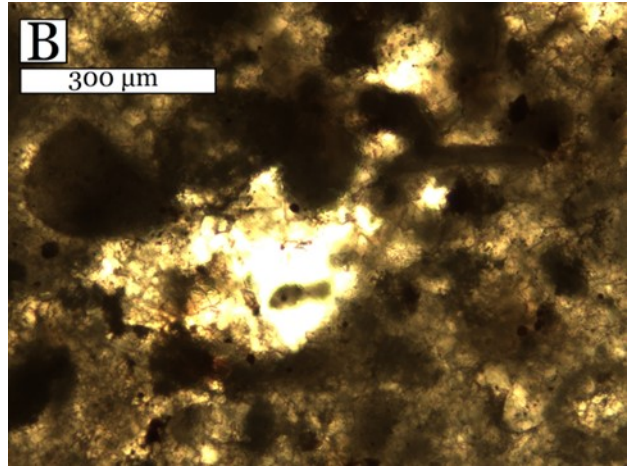
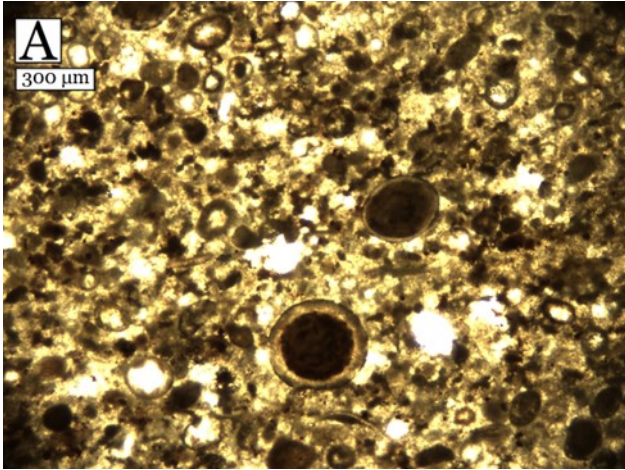


*WG35: A & B in PPL*

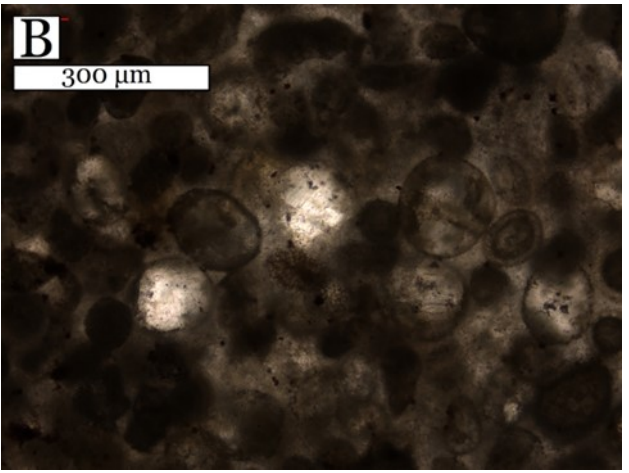
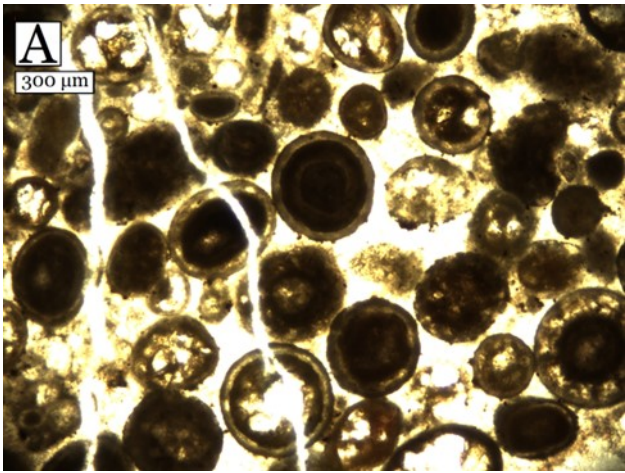


*WG37: A & B in PPL*





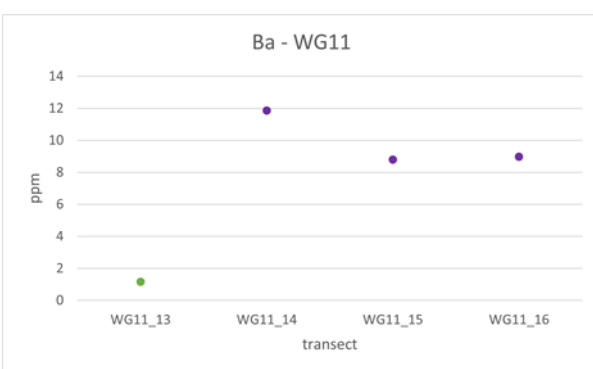
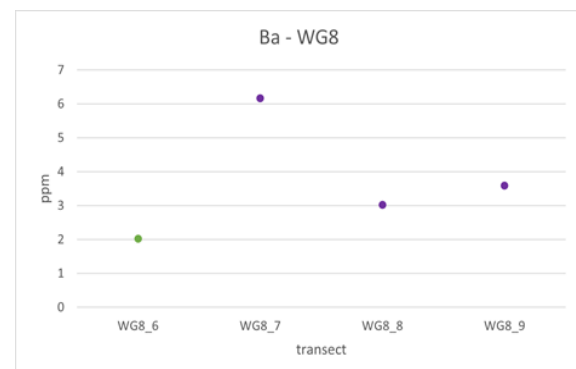
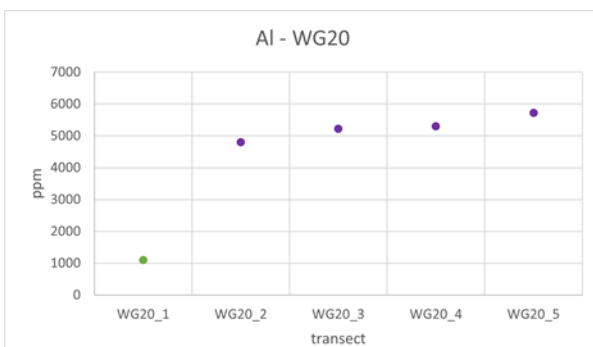
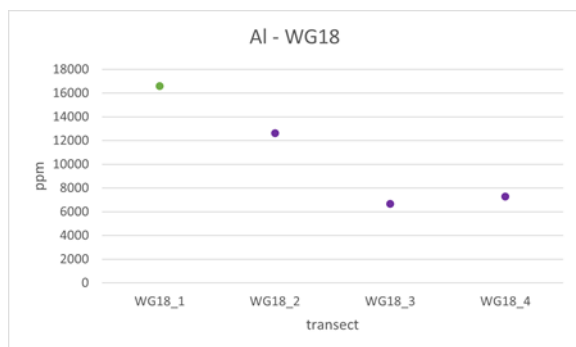
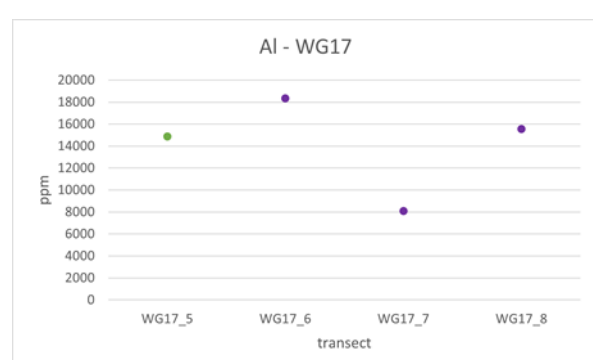
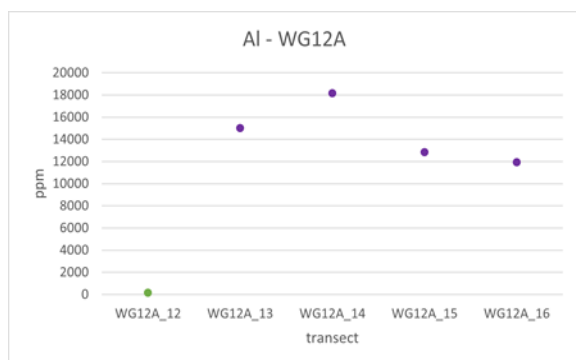
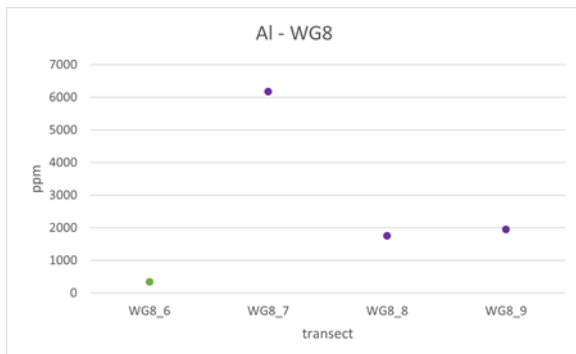
*WG40: A & B in PPL*

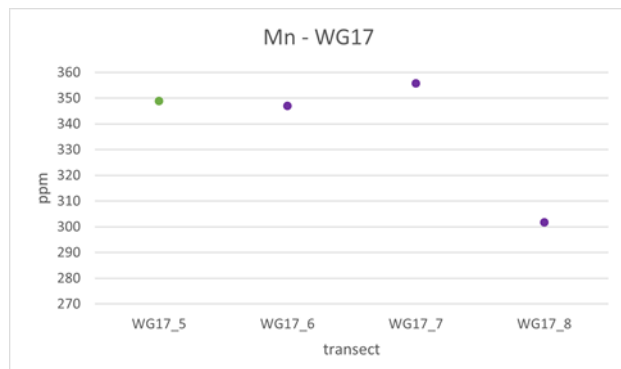
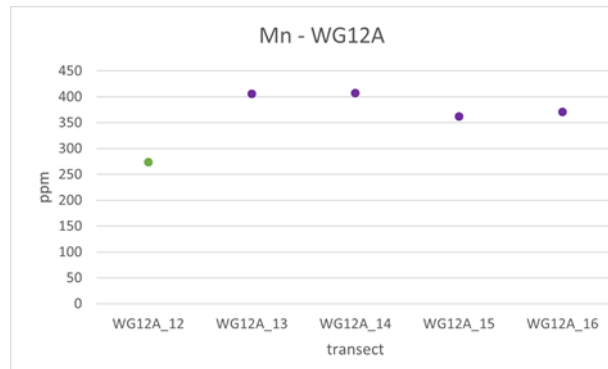
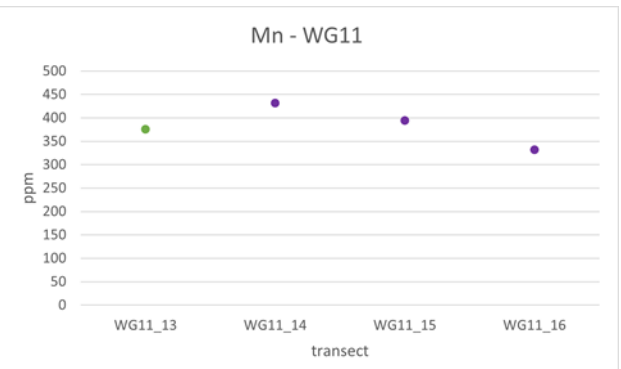
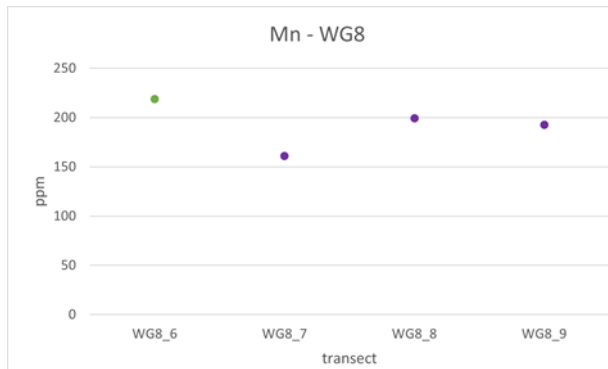
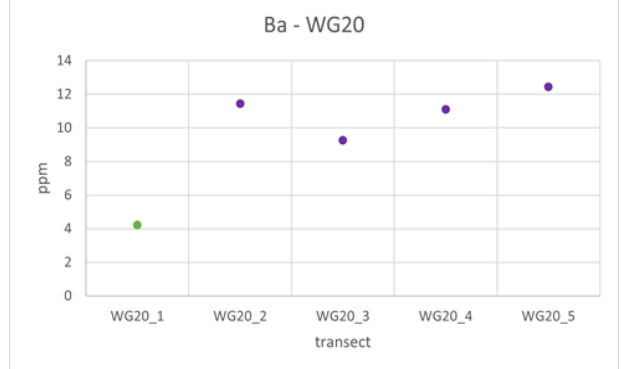
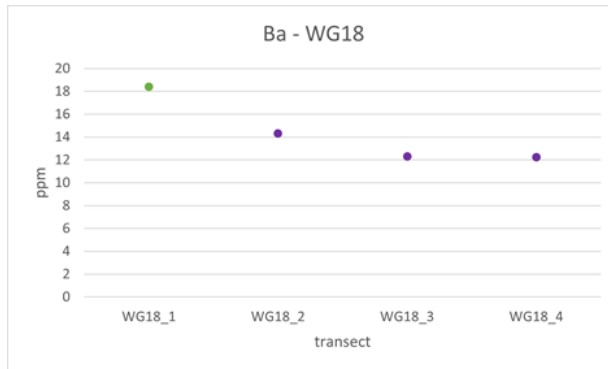
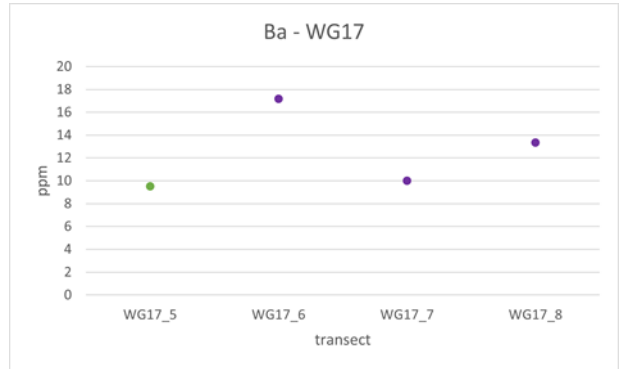
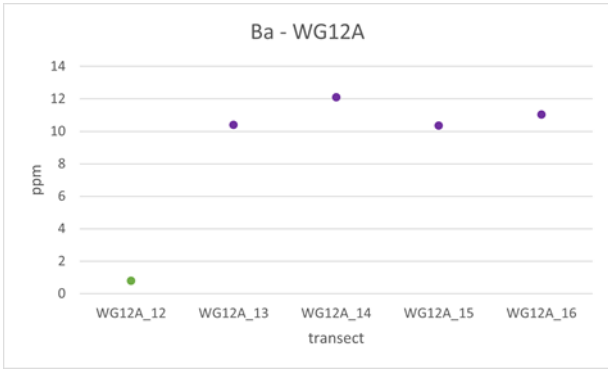


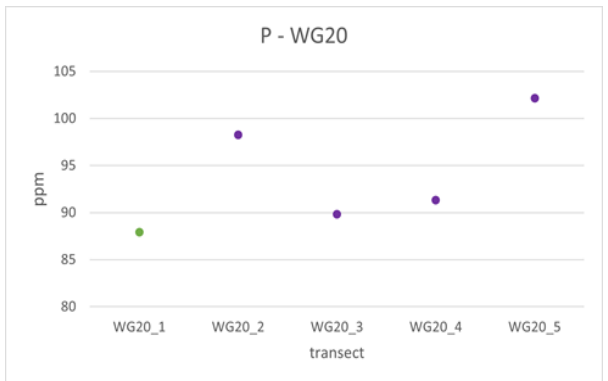
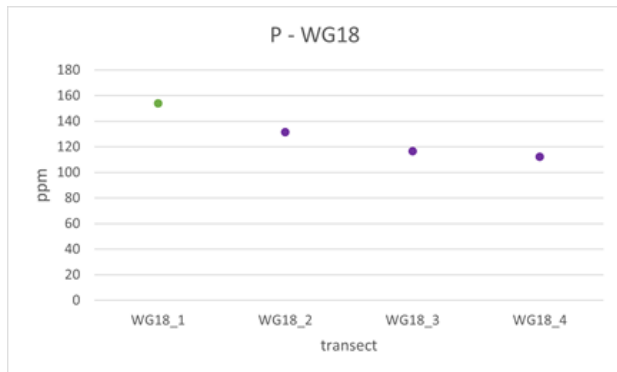
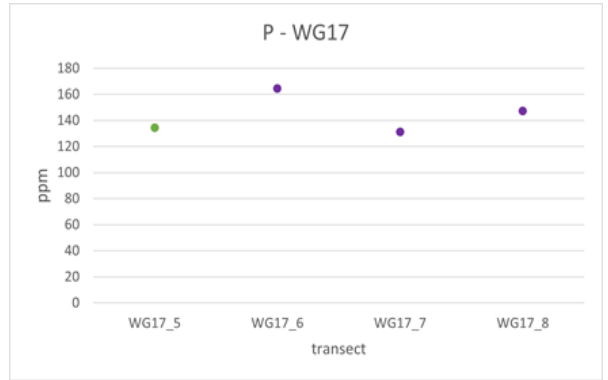
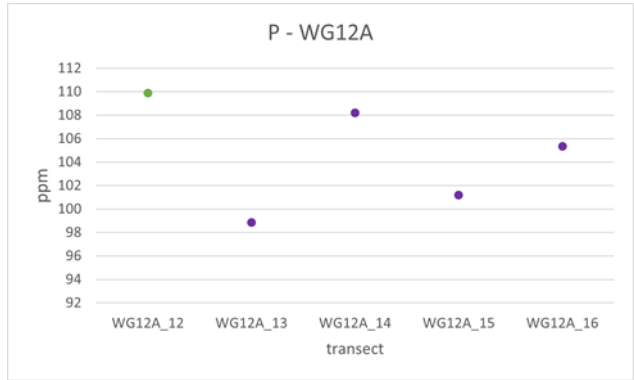
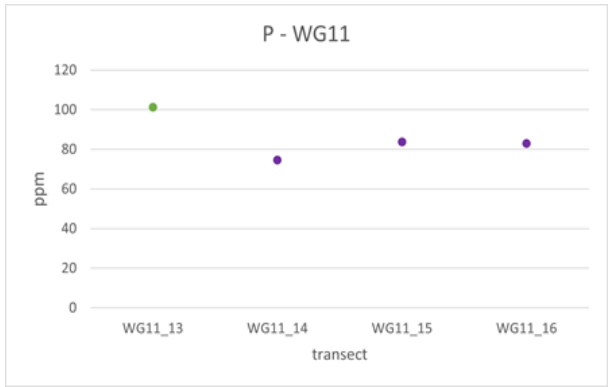
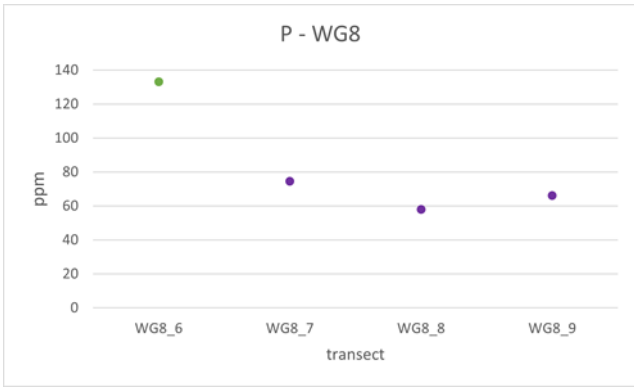
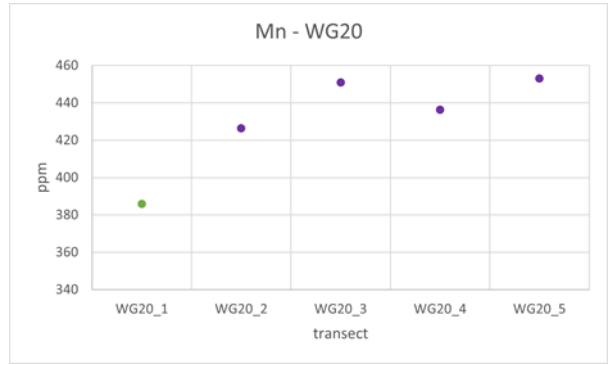
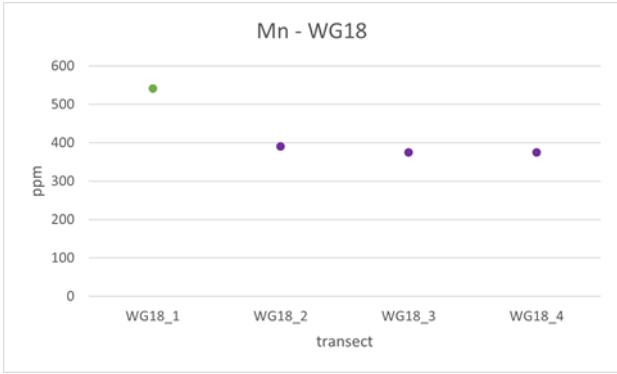
*WG44: A & B in PPL*

## Appendix 2—LA-ICP-MS transects

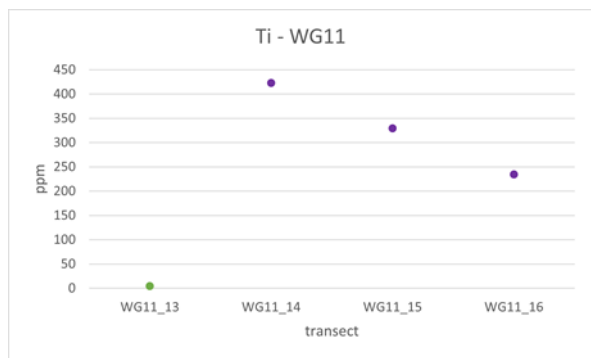
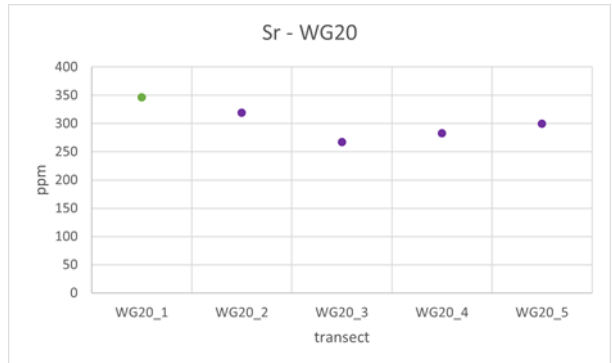
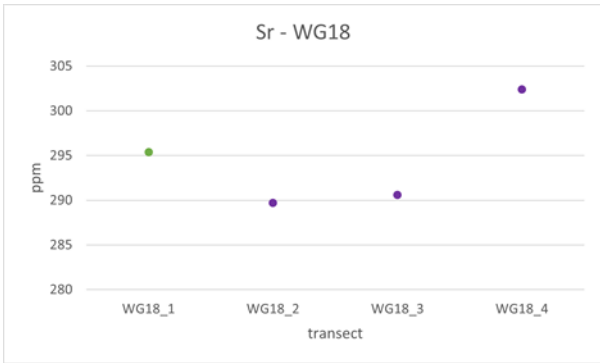
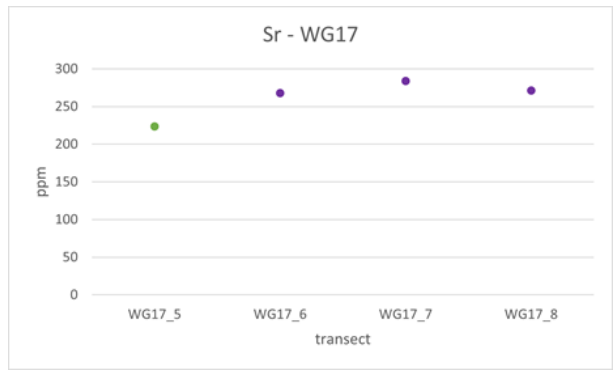
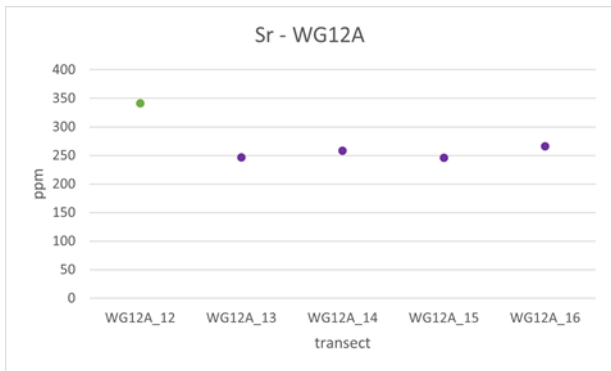
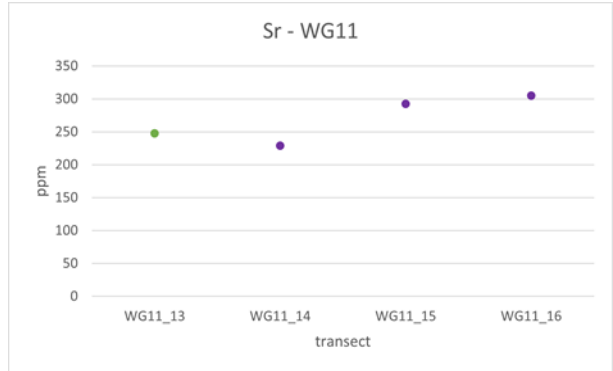
Transects – Green dots represents nuclei, purple represents ooid cortex. As we go to the right in the diagrams, we go further outwards from the nuclei.

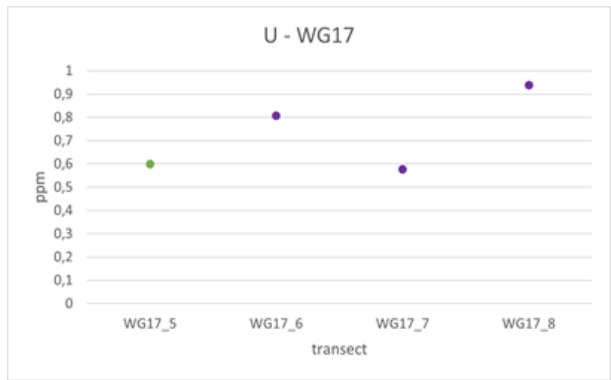
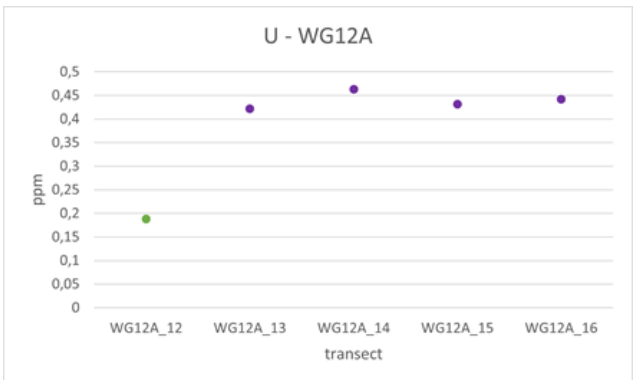
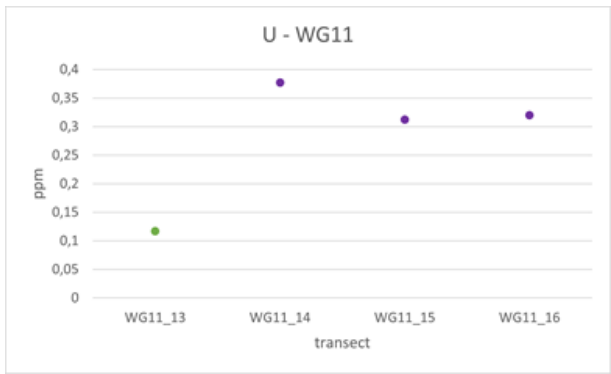
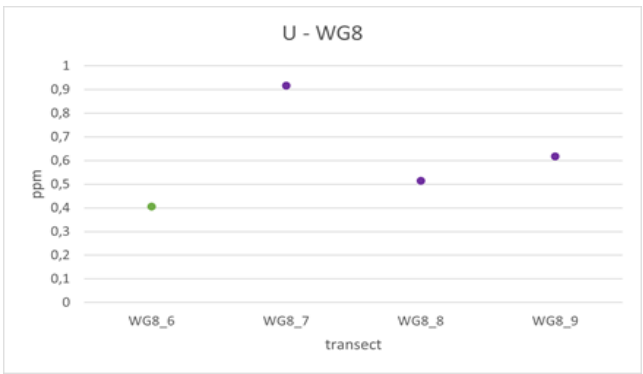
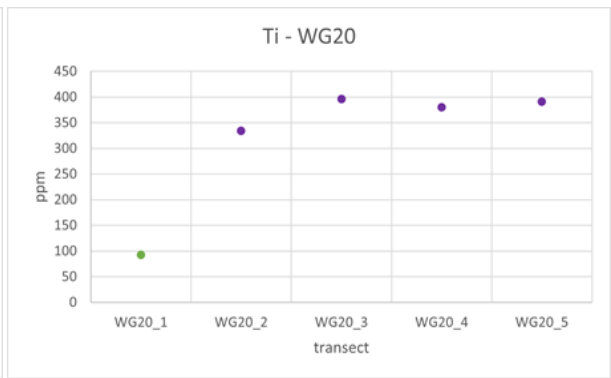
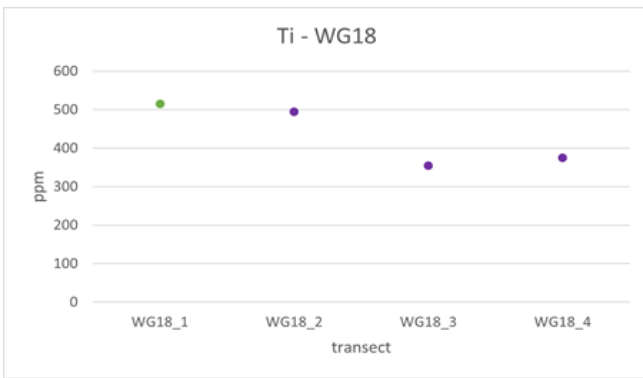
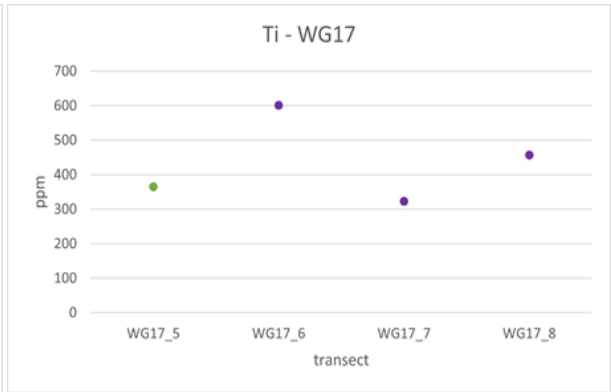
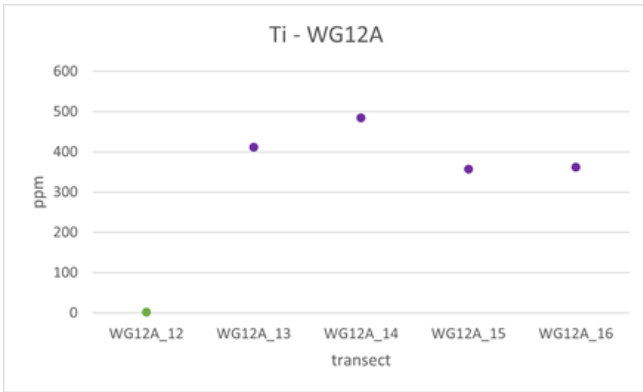


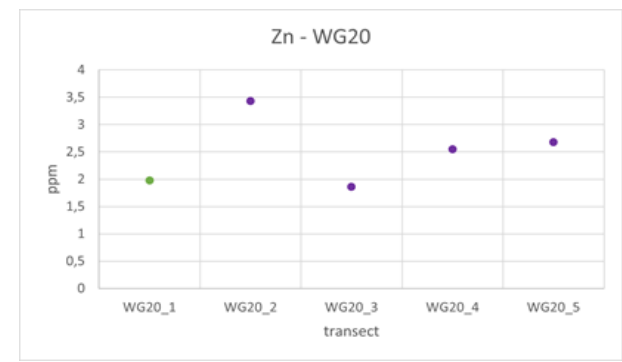
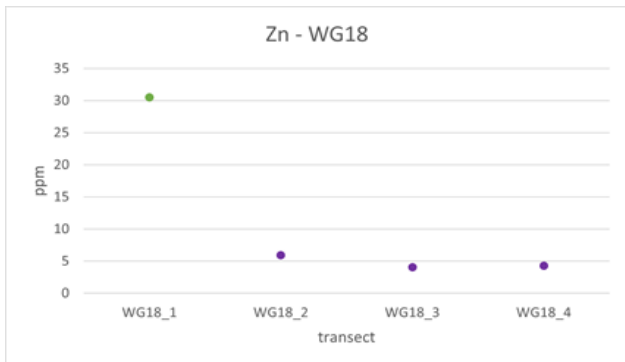
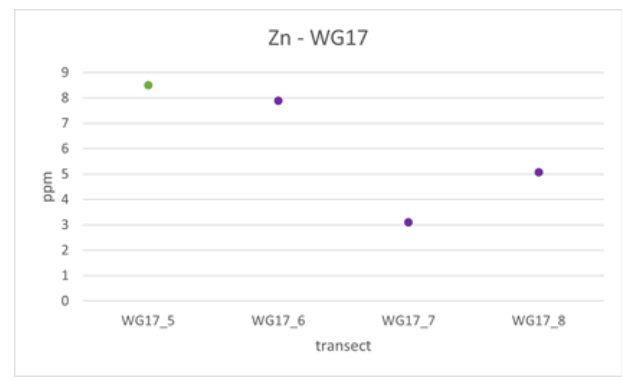
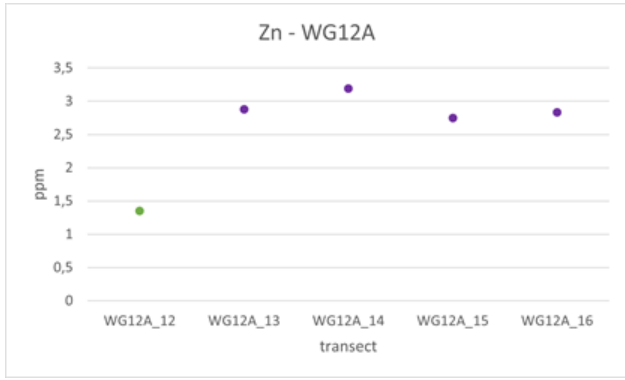
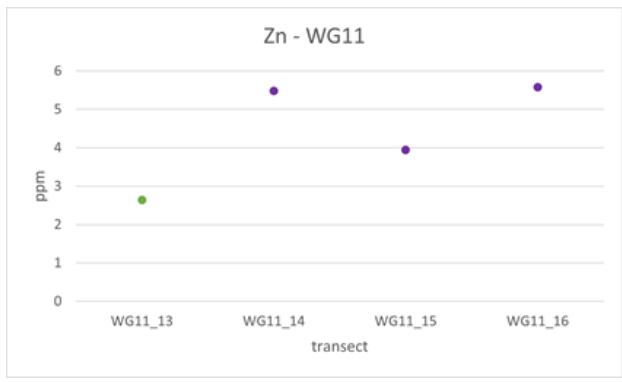
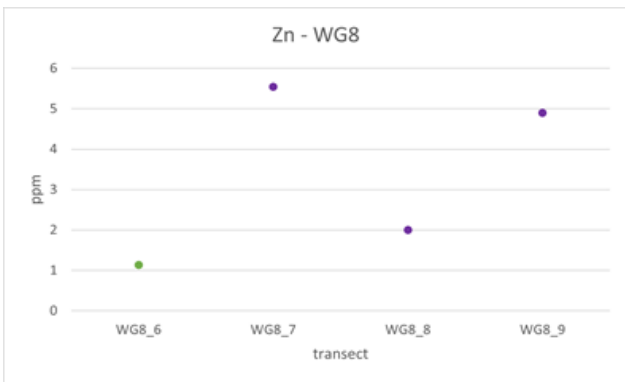
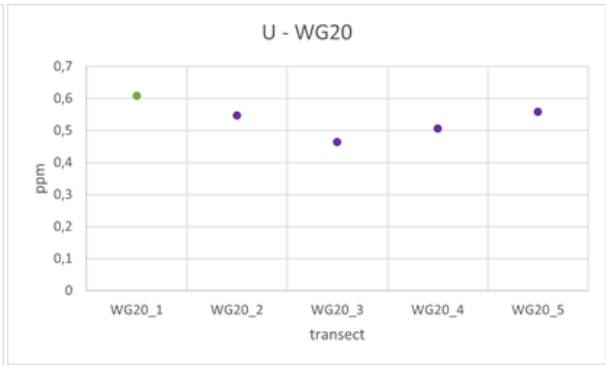
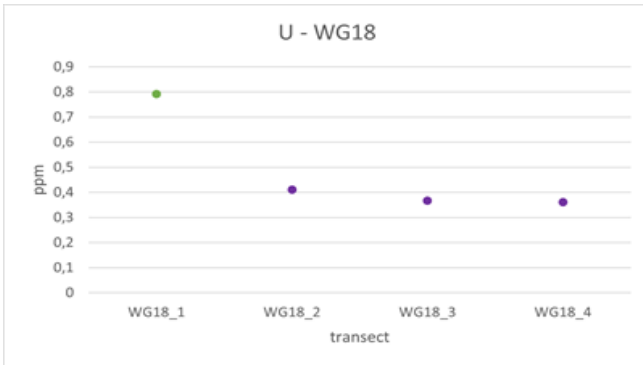






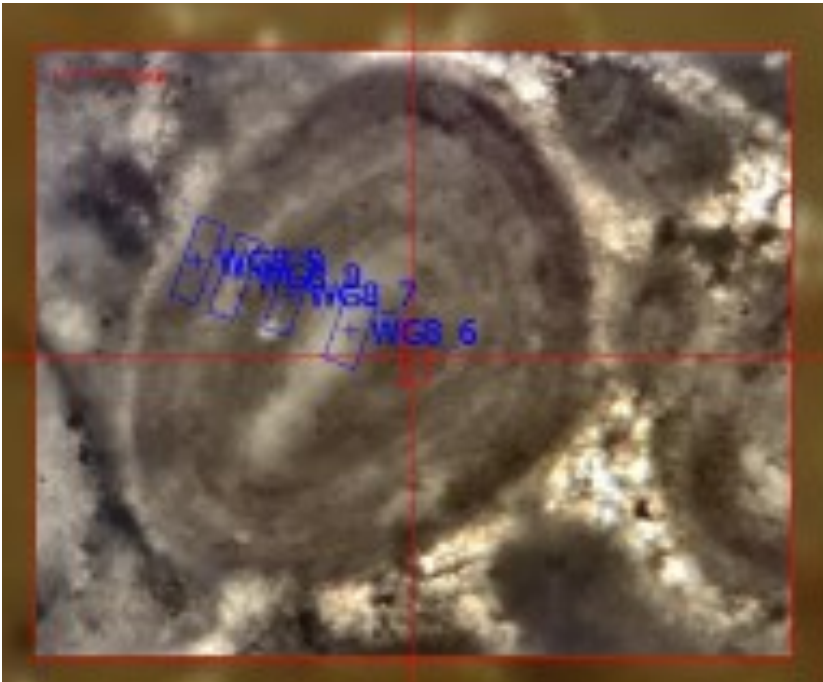
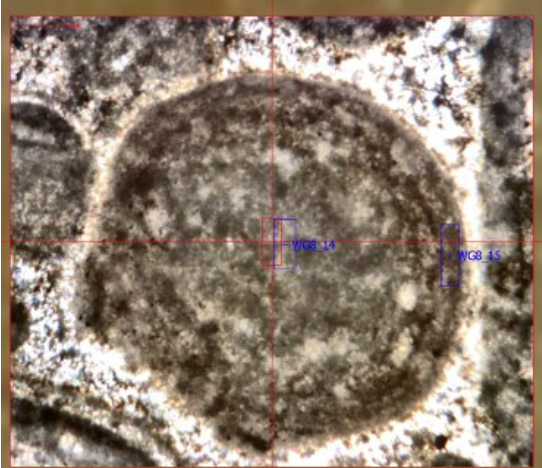


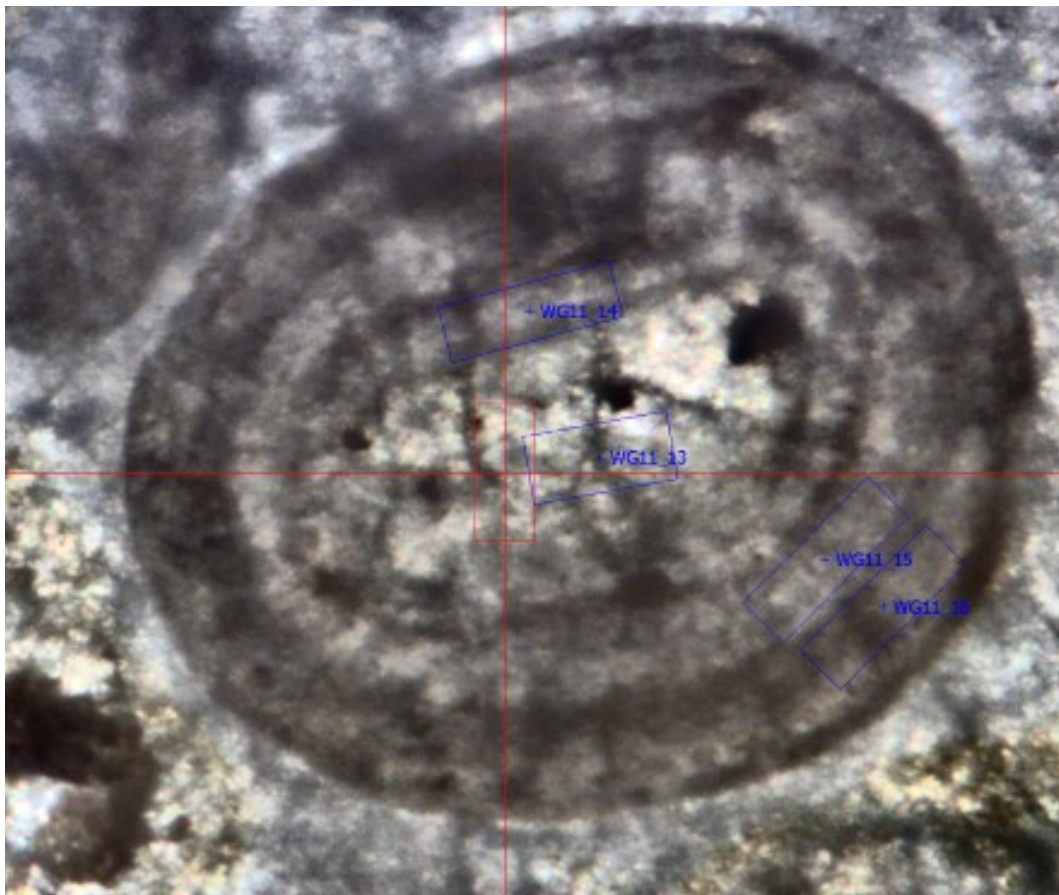
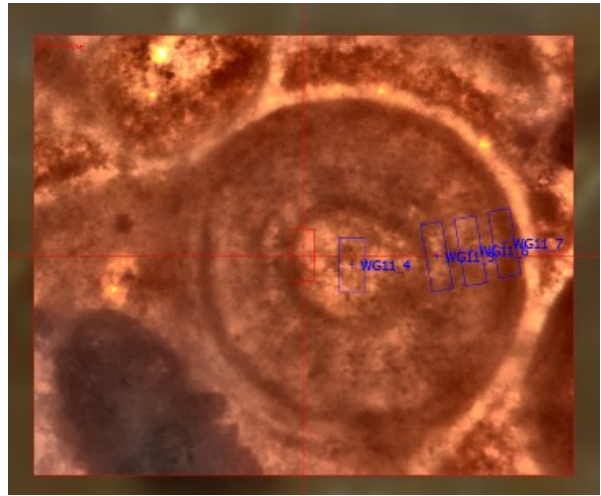
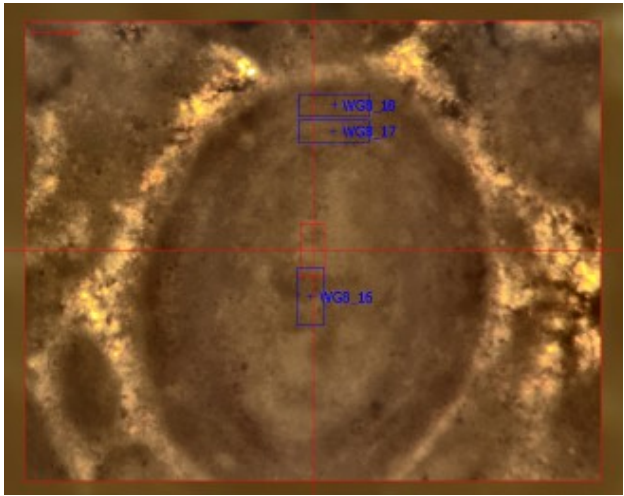




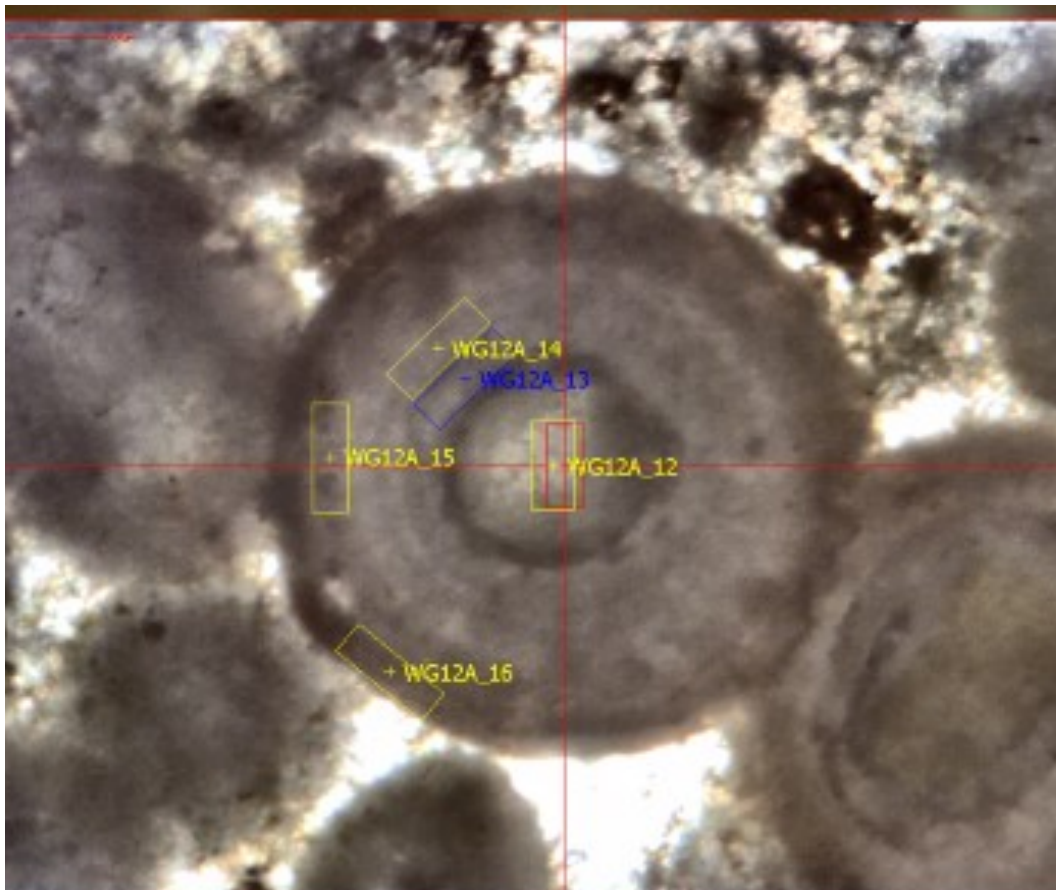
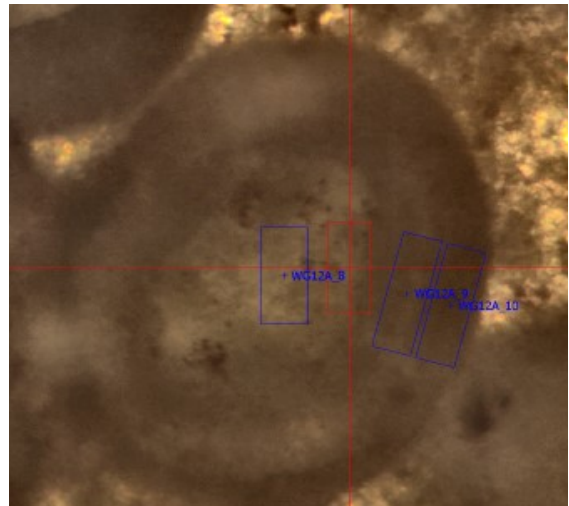
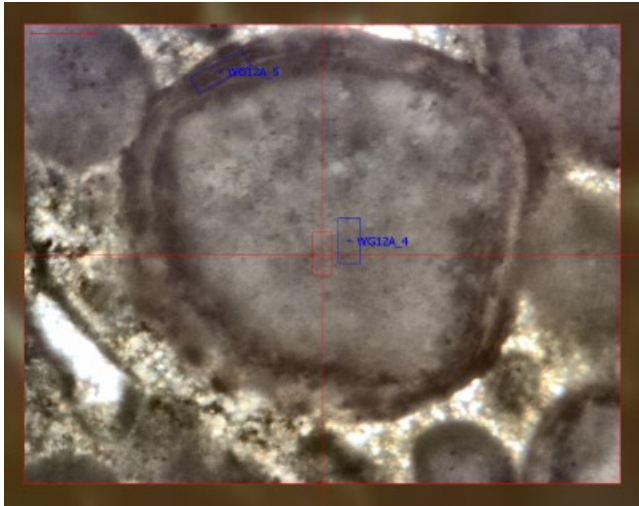
### Appendix 3— LA-ICP-MS Spot reference images for ooids

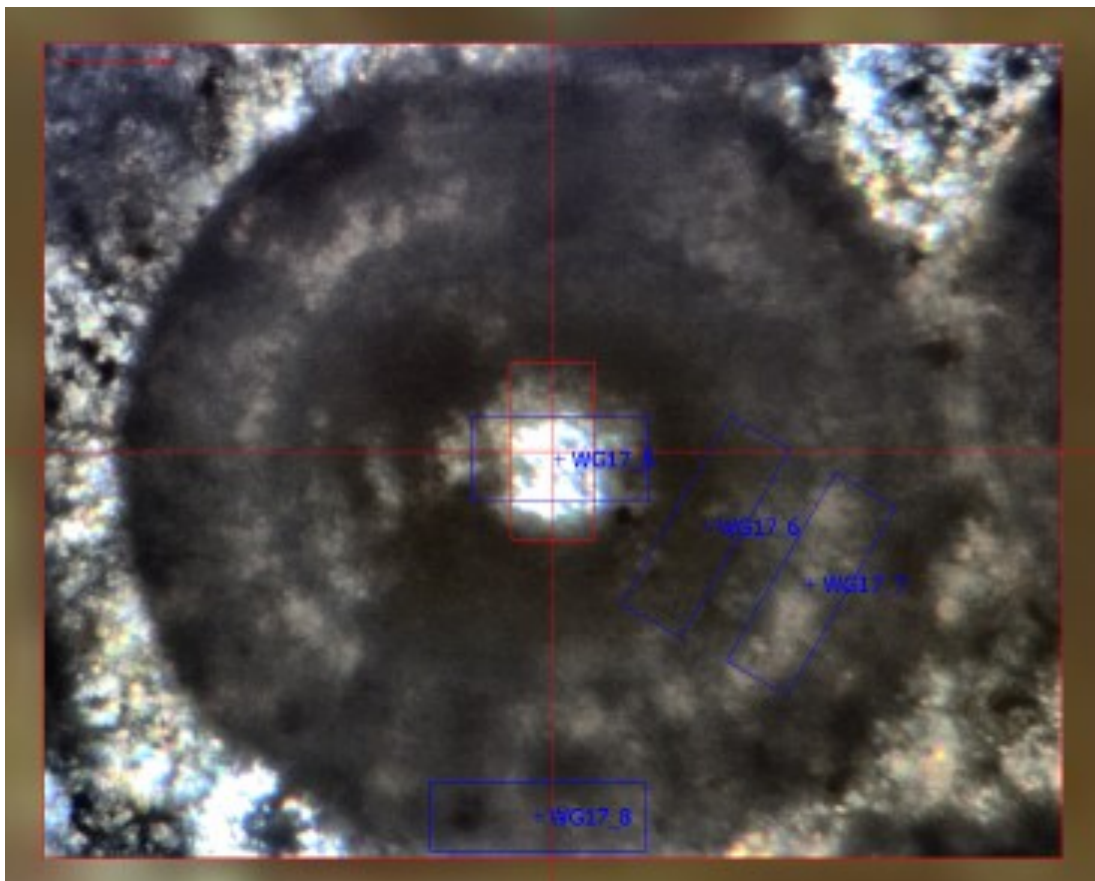
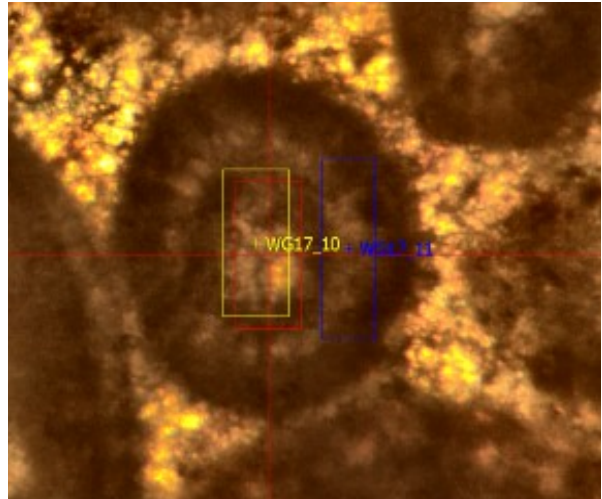
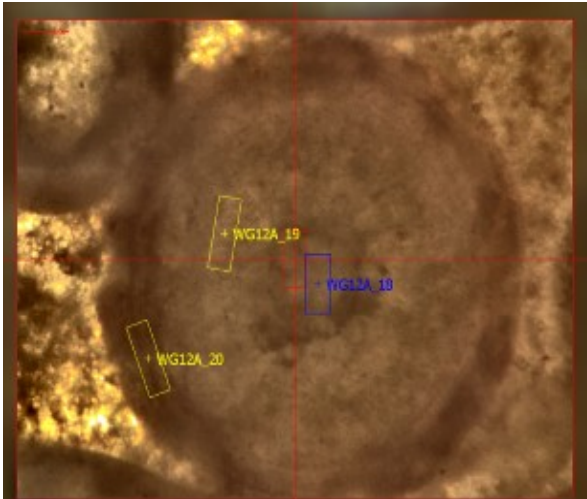
Images of the ooids which were used for examples of transect graphs in chapter 5.8 and Appendix 2 have been particularly enlarged here at the bottom of each page.

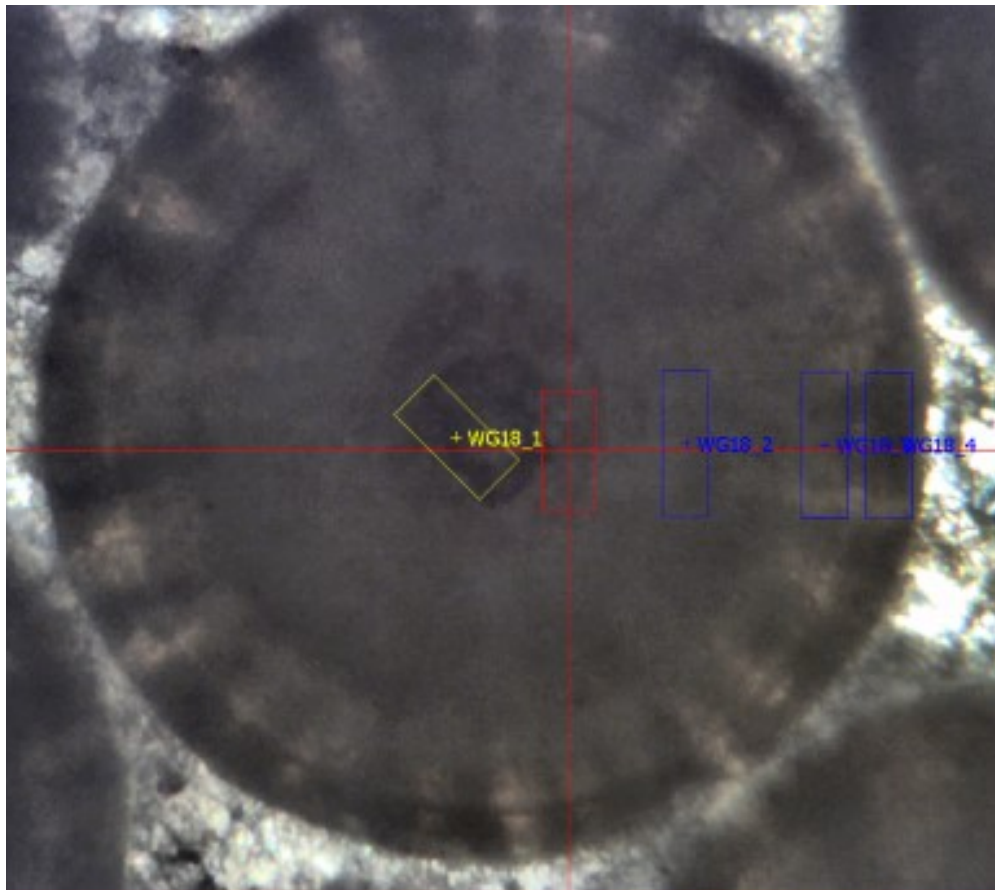
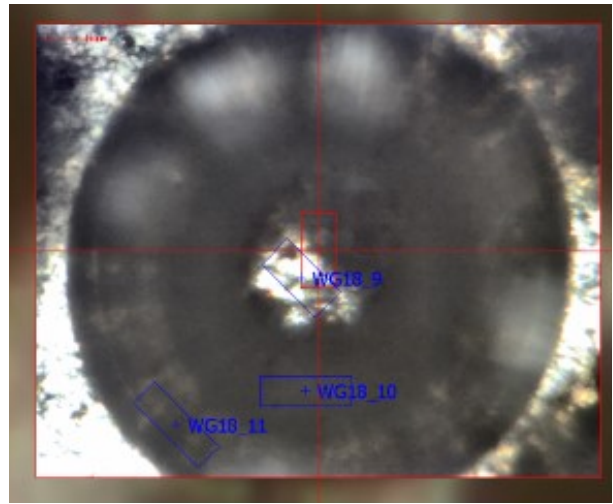
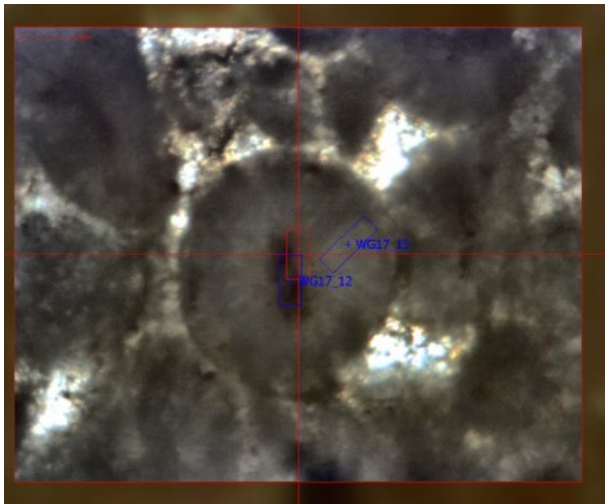




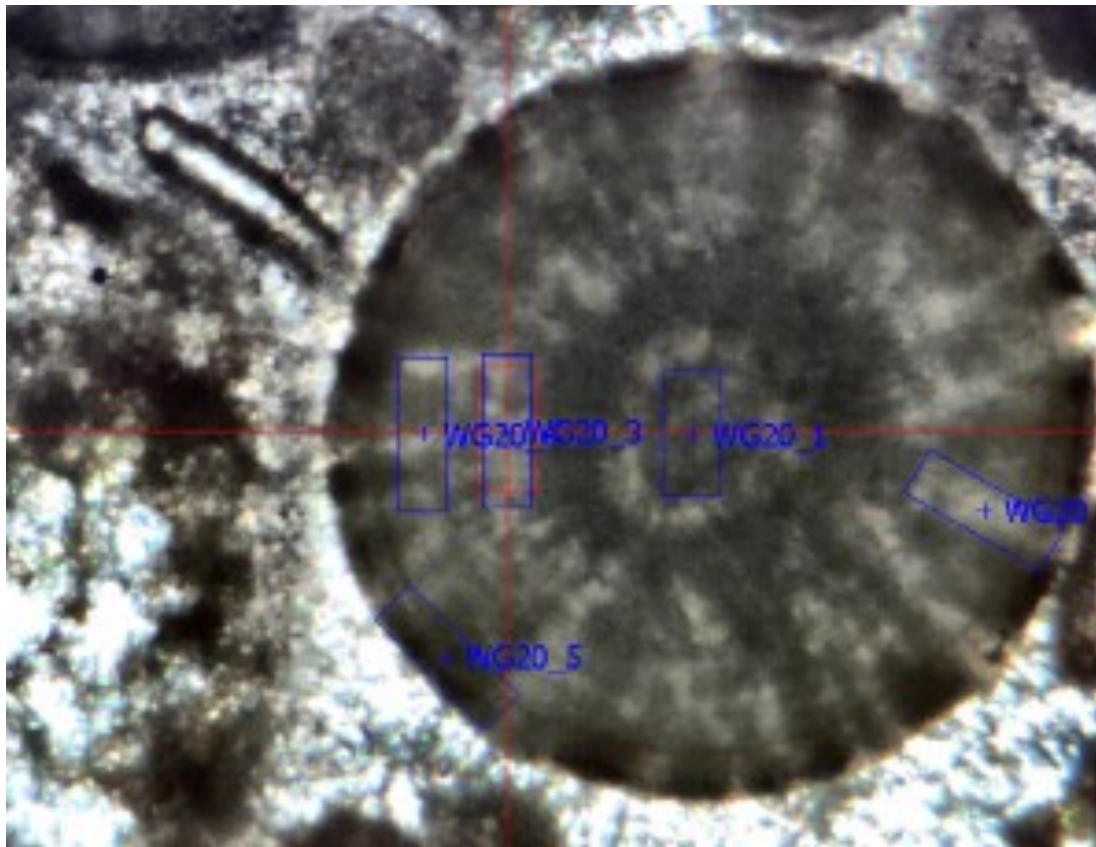
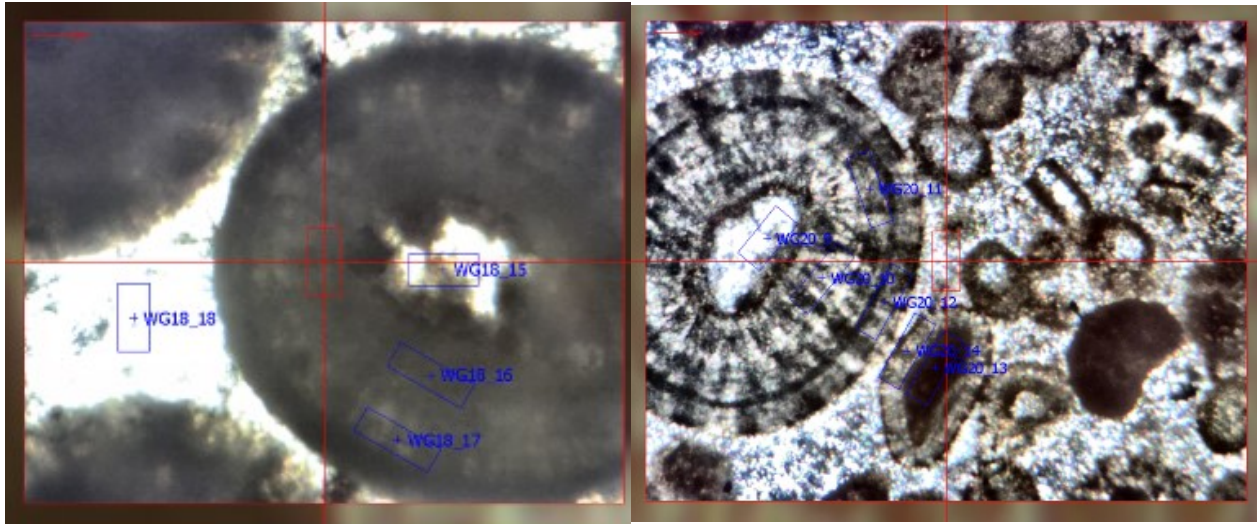












**Tidigare skrifter i serien  
”Examensarbeten i Geologi vid Lunds  
universitet”:**

563. Bjeremo, Tim, 2019: Eoliska avlagringar och vindriktningar under holocen i och kring Store Mosse, södra Sverige. (15 hp)
564. Langkjaer, Henrik, 2019: Analys av Östergötlands kommande grundvattenresurser ur ett klimtperspektiv - med fokus på förstärkt grundvattenbildning. (15 hp)
565. Johansson, Marcus, 2019: Hur öppet var landskapet i södra Sverige under Atlantisk tid? (15 hp)
566. Molin, Emmy, 2019: Litologi, sedimentologi och kolisotopstratigrafi över krita-paleogen-gränsintervallet i borrhningen Limhamn-2018. (15 hp)
567. Schroeder, Mimmi, 2019: The history of European hemp cultivation. (15 hp)
568. Damber, Maja, 2019: Granens invandring i sydvästa Sverige, belyst genom pollenanalys från Skottensjön. (15 hp)
569. Lundgren Sassner, Lykke, 2019: Strandmorfologi, stranderosion och stranddeposition, med en fallstudie på Tylösand sandstrand, Halland. (15 hp)
570. Greiff, Johannes, 2019: Mesozoiska konglomerat och Skånes tektoniska utveckling. (15 hp)
571. Persson, Eric, 2019: An Enigmatic Cerapodian Dinosaur from the Cretaceous of southern Sweden. (15 hp)
572. Aldenius, Erik, 2019: Subsurface characterization of the Lund Sandstone – 3D model of the sandstone reservoir and evaluation of the geoenery storage potential, SW Skåne, South Sweden. (45 hp)
573. Juliusson, Oscar, 2019: Impacts of subglacial processes on underlying bedrock. (15 hp)
574. Sartell, Anna, 2019: Metamorphic paragenesis and P-T conditions in garnet amphibolite from the Median Segment of the Idefjorden Terrane, Lilla Edet. (15 hp)
575. Végvári, Fanni, 2019: Vulkanisk inverkan på klimatet och atmosfärcirkulationen: En litteraturstudie som jämför vulkanism på låg respektive hög latitud. (15 hp)
576. Gustafsson, Jon, 2019: Petrology of platinum-group element mineralization in the Koillismaa intrusion, Finland. (45 hp)
577. Wahlquist, Per, 2019: Undersökning av mindre förkastningar för vattentag i sedimentärt berg kring Kingelstad och Tjutebro. (15 hp)
578. Gaitan Valencia, Camilo Esteban, 2019: Unravelling the timing and distribution of Paleoproterozoic dyke swarms in the eastern Kaapvaal Craton, South Africa. (45 hp)
579. Eggert, David, 2019: Using Very-Low-Frequency Electromagnetics (VLF-EM) for geophysical exploration at the Albertine Graben, Uganda - A new CAD approach for 3D data blending. (45 hp)
580. Plan, Anders, 2020: Resolving temporal links between the Högberget granite and the Wigström tungsten skarn deposit in Bergslagen (Sweden) using trace elements and U-Pb LA-ICPMS on complex zircons. (45 hp)
581. Pilser, Hannes, 2020: A geophysical survey in the Chocaya Basin in the central Valley of Cochabamba, Bolivia, using ERT and TEM. (45 hp)
582. Leopardi, Dino, 2020: Temporal and genetic constraints of the Cu-Co Vena-Dampetorp deposit, Bergslagen, Sweden. (45 hp)
583. Lagerstam Lorient, Clarence, 2020: Neck mobility versus mode of locomotion – in what way did neck length affect swimming performance among Mesozoic plesiosaurs (Reptilia, Sauropterygia)? (45 hp)
584. Davies, James, 2020: Geochronology of gneisses adjacent to the Mylonite Zone in southwestern Sweden: evidence of a tectonic window? (45 hp)
585. Foyn, Alex, 2020: Foreland evolution of Blåisen, Norway, over the course of an ablation season. (45 hp)
586. van Wees, Roos, 2020: Combining luminescence dating and sedimentary analysis to derive the landscape dynamics of the Velická Valley in the High Tatra Mountains, Slovakia. (45 hp)
587. Rettig, Lukas, 2020: Implications of a rapidly thinning ice-margin for annual moraine formation at Gornergletscher, Switzerland. (45 hp)
588. Bejarano Arias, Ingrid, 2020: Determination of depositional environment and luminescence dating of Pleistocene deposits in the Biely Váh valley, southern foothills of the Tatra Mountains, Slovakia. (45 hp)
589. Olla, Daniel, 2020: Petrografisk beskrivning av Prekambriska ortogneiser i den undre delen av Särsvskollan, mellersta delen av Skollenheten, Kaledonska orogener. (15 hp)
590. Friberg, Nils, 2020: Är den sydatlantiska magnetiska anomalin ett återkommande fenomen? (15 hp)
591. Brakebusch, Linus, 2020: Klimat och väder i Nordatlanten-regionen under det senaste årtusendet. (15 hp)
592. Boestam, Max, 2020: Stränder med erosion och ackumulation längs kuststräckan Trelleborg - Abbekås under perioden 2007-2018. (15 hp)



593. Agudelo Motta, Laura Catalina, 2020: Methods for rockfall risk assessment and estimation of runout zones: A case study in Gothenburg, SW Sweden. (45 hp)
594. Johansson, Jonna, 2020: Potentiella nedslagskratrar i Sverige med fokus på Östersjön och östkusten. (15 hp)
595. Haag, Vendela, 2020: Studying magmatic systems through chemical analyses on clinopyroxene - a look into the history of the Teno ankaramites, Tenerife. (45 hp)
596. Kryffin, Isidora, 2020: Kan benceller bevaras över miljontals år? (15 hp)
597. Halvarsson, Ellinor, 2020: Sökande efter nedslagskratrar i Sverige, med fokus på avtryck i berggrunden. (15 hp)
598. Jirdén, Elin, 2020: Kustprocesser i Arktis – med en fallstudie på Prins Karls Forland, Svalbard. (15 hp)
599. Chonewicz, Julia, 2020: The Eemian Baltic Sea hydrography and paleoenvironment based on foraminiferal geochemistry. (45 hp)
600. Paradeisis-Stathis, Savvas, 2020: Holocene lake-level changes in the Siljan Lake District – Towards validation of von Post's drainage scenario. (45 hp)
601. Johansson, Adam, 2020: Groundwater flow modelling to address hydrogeological response of a contaminated site to remediation measures at Hjortsberga, southern Sweden. (15 hp)
602. Barrett, Aodhan, 2020: Major and trace element geochemical analysis of norites in the Hakefjorden Complex to constrain magma source and magma plumbing systems. (45 hp)
603. Lundqvist, Jennie, 2020: "Man fyller det med information helt enkelt": en fenomenografisk studie om studenters upplevelse av geologisk tid. (45 hp)
604. Zachén, Gabriel, 2020: Classification of four mesosiderites and implications for their formation. (45 hp)
605. Viðarsdóttir, Halla Margrét, 2020: Assessing the biodiversity crisis within the Triassic-Jurassic boundary interval using redox sensitive trace metals and stable carbon isotope geochemistry. (45 hp)
606. Tan, Brian, 2020: Nordvästra Skånes prekambrika geologiska utveckling. (15 hp)
607. Taxopoulou, Maria Eleni, 2020: Metamorphic micro-textures and mineral assemblages in orthogneisses in NW Skåne – how do they correlate with technical properties? (45 hp)
608. Damber, Maja, 2020: A palaeoecological study of the establishment of beech forest in Söderåsen National Park, southern Sweden. (45 hp)
609. Karastergios, Stylianos, 2020: Characterization of mineral parageneses and metamorphic textures in eclogite- to high-pressure granulite-facies marble at Allmenningen, Roan, western Norway. (45 hp)
610. Lindberg Skutsjö, Love, 2021: Geologiska och hydrogeologiska tolkningar av SkyTEM-data från Vombsänkan, Sjöbo kommun, Skåne. (15 hp)
611. Hertzman, Hanna, 2021: Odensjön - A new varved lake sediment record from southern Sweden. (45 hp)
612. Molin, Emmy, 2021: Rare terrestrial vertebrate remains from the Pliensbachian (Lower Jurassic) Hasle Formation on the Island of Bornholm, Denmark. (45 hp)
613. Höjbert, Karl, 2021: Dendrokronologi - en nyckelmetod för att förstå klimat- och miljöförändringar i Jämtland under holoцен. (15 hp)
614. Lundgren Sassner, Lykke, 2021: A Method for Evaluating and Mapping Terrestrial Deposition and Preservation Potential- for Palaeostorm Surge Traces. Remote Mapping of the Coast of Scania, Blekinge and Halland, in Southern Sweden, with a Field Study at Dalköpinge Ängar, Trelleborg. (45 hp)
615. Granbom, Johanna, 2021: En detaljerad undersökning av den mellanordoviciska "furudalkalkstenen" i Dalarna. (15 hp)
616. Greiff, Johannes, 2021: Oolites from the Arabian platform: Archives for the aftermath of the end-Triassic mass extinction. (45 hp)



# LUNDS UNIVERSITET

Geologiska institutionen  
Lunds universitet  
Sölvegatan 12, 223 62 Lund